Computer Aided Diagnosis of Complications of Total Hip Replacement X-Ray Images

by

Najiba AL-Zadjali

A Doctoral Thesis

Submitted in partial fulfilment
of the requirements for the award of
Doctor of Philosophy
of
Loughborough University

16th of October 2017

Abstract

Hip replacement surgery has experienced a dramatic evolution in recent years supported by the latest developments in many areas of technology and surgical procedures. Unfortunately complications that follow hip replacement surgery remains the most challenging dilemma faced both by the patients and medical experts.

The thesis presents a novel approach to segment the prosthesis of a THR surgical process by using an Active Contour Method (ACM) that is initiated via an automatically detected seed point within the enarthrosis region of the prosthesis. The circular area is detected via the use of a Fast, Randomized Circle Detection Algorithm. Experimental results are provided to compare the performance of the proposed ACM based approach to popular thresholding based approaches. Further an approach to automatically detect the Obturator Foramen using an ACM approach is also presented.

Based on analysis of how medical experts carry out the detection of loosening and subsidence of a prosthesis and the presence of infections around the prosthesis area, this thesis presents novel computational analysis concepts to identify the key feature points of the prosthesis that are required to detect all of the above three types of complications. Initially key points along the prosthesis boundary are determined by measuring the curvature on the surface of the prosthesis. By traversing the edge pixels, starting from one end of the boundary of a detected prosthesis, the curvature values are determined and effectively used to determine key points of the prosthesis surface and their relative positioning. After the key-points are detected, pixel value gradients across the boundary of the prosthesis are determined along the boundary of the prosthesis to determine the presence of subsidence, loosening and infections.

Experimental results and analysis are presented to show that the presence of subsidence is determined by the identification of dark pixels around the convex bend closest to the stem area of the prosthesis and away from it. The presence of loosening is determined by the additional presence of dark regions just outside the two straight line edges of the stem area of the prosthesis. The presence of infections is represented by the determination of dark areas around the tip of the stem of the prosthesis. All three complications are thus determined by a single process where the detailed analysis defer. The experimental results presented show the effectiveness of all proposed approaches which are also compared and validated against the ground truth recorded manually with expert user input.

Najiba Al-Zadjali
16th October 2017

Acknowledgements

This thesis is culmination of my PhD journey which was full of encouragement, confidence, hardworking and frustration. When I found myself experiencing the feeling of accomplishment, I realized though only my name appears on the cover of this thesis. Many people supported me through this journey. First and foremost, I would like to thank God for giving me the opportunity to peruse this research study and surrounding me with his blessing.

A very special gratitude goes to my supervisor Professor Eran Edirisingh for enlightening me the first glance of this research. His precious support, patience and insightful comments widen the research from various perspectives.

I would like to thank all my friends and colleagues of computer science research laboratory for their spiritual support and spending such wonderful time with them. A special thanks goes to Giounona Tzanidou for her support at the beginning of my PhD journey and also Hanaa Mahmood.

I owe a deep sense of gratitude to Ministry of Manpower for funding my PhD scholarship. The research presented in this thesis would not have been possible without collaboration with the Musculoskeletal Surgical Team of the Leicester Glenfield Hospital headed by Prof Joseph Dias. Prof Dias's expert comments, suggestions, evaluations and patience is very much appreciated with gratitude.

Last but not least, my sincere thanks also goes to my lovely children Omair, Zainab and Muhja for giving me strength and their enthusiasm and in excelling in their school studies. Thank you for making proud. My extreme thanks to my family for their support and valuable prayers.

Najiba Al-Zadjali, October 2017

Table of Contents

List of Figures

List of Acronyms

THR	Total Hip Replacement
THA	Total Hip Arthroplasty
CT	Computed Tomography
MRI	Magnetic Resonance Imaging
2D	Two Dimensional
3D	Three Dimensional
ROI	Region of Interest
POI	Point of Interest
MSE	Mean Square Error
SE	Structuring Element
GVF	Gradient Vector Flow
ACM	Active Contour Method
ASM	Active Shape Model

Chapter 1.

Introduction

Developments of medical diagnostics tools that are based on image analysis, computer vision and image processing algorithms have shown great promise and holds ample scope for collaborative research between experts from various fields. Lesion diagnoses such bone fractures, wound ulcers, tumours and infectious or inflammatory disease are examples of the outcomes that can be expected of such collaborative research efforts. Designing such computer-aided detection systems is a complex procedure that requires an understanding of the biology of the lesion.

Total Hip Replacement (THR) is an orthopaedic surgical procedure conducted to remove damaged hip joints and replace them with artificial joints, medically known as a 'prosthesis'. The prosthesis used in THR consists of a ball component made of metal or ceramic and a socket, which has an insert or liner made of plastic, ceramic or metal[1]. The prosthesis is carefully fitted in the thighbone and acetabulum, allowing the joint to move smoothly in multiple directions, functioning as a normal hip joint.

Unfortunately, replacing the hip joint with steel implant can cause serious complications, such as loosening, subsidence, infection, wear, dislocation and misalignment; common modalities such as ultrasound, CT and MRI generate images with high resolutions produce large number of image slices. This would create a difficultly in visualising complex structure without cutting away large portions of perhaps crucial information to medical diagnosis. Creating a computer-aided system that processes information of this diversity is complicated; though, the

motivation is that to have such a system for certain situations can provide valuable diagnostic support to those involved in medical diagnosis. Computers excel at keeping track of large amounts of data and at performing time-consuming and tedious tasks, effectively and quickly: a combination of a human interpreter and a computerised system can therefore improve diagnostic accuracy (Mitchell et al. [2]). It is apparent that radiologists' performance in diagnosing medical dilemmas is improved significantly by the use of computer-aided systems. In the current practice of assessing THR complications, radiologists assess the prosthesis by looking for signs in the form of imperfections and comparing a number of standard x-ray images of the patient's hip taken over a long period of time.

This research focuses on the use of image processing algorithms to automatically detect THR complications, which can significantly aid clinical experts and radiologists and minimise the possibility of human error, as well as significantly reducing the time needed for such diagnostics. In this thesis, a novel image analysis-based technique is proposed that automatically detects most devastating clinical complications within Total Hip Replacement (THR) surgery, namely, loosening, subsidence and infection. Loosening refers to a condition in which the prosthesis becomes loose within the surgically created hollow area of the thigh bone due to the absence of cement layer around the prosthesis or the thinning of the bone around the un-cemented prosthesis. Subsidence refers to a condition in which the prosthesis unexpectedly subsides further into the bone. Infection is a condition wherein a clinical infection ripens on the boundary of the prosthesis or a sudden inflammatory syndrome without any initial signs. All these complications develop typically in the region that immediately surrounds the surface of the implanted prosthesis. Therefore, detecting these complications should commence by detection and the extraction of the boundary of the implanted steel 'prosthesis', followed by a surface contour analysis to determine the key points on the surface of the prosthesis that can be used as points of reference with respect to which the complications are referred to.

This is a crucial initial step in detecting THR complications automatically. By and large, detecting THR complications encompasses several distinct steps that mainly depend on finding region of interest on the prosthesis boundary and determining the pixel value variation across the prosthesis boundary.

1.1. Research Motivation

With the rapid increase of THR surgeries in orthopaedics that has resulted from the aging population of the world at present, medical experts are in need for automated or semi-automated processing tools that can provide accurate and robust image analysis to segment, track, recognize and detect various abnormalities related to THR surgery. Such diagnostic tools in the medical fields have proven increased diagnostics accuracy and speed of providing effective medical care improving the service provided to the patients and saving health service organisations substantial amount of funds. According to the British Orthopaedic Assocaiation [3] in England and Wales over 80,000 people had such operations in 2011 and the number continues to rise. In the past, patients between 60 and 75 years of age were considered to be the best candidates for THR. However, at present the average range has been extended to include more elderly patients as well as younger patients.

Like in any other surgical procedure, complications may develop that will require post-surgery follow ups and careful monitoring to avoid revision surgery. Although the current modalities provide significant information about THR complications for medical interpretation; processing this information involves complicated techniques such familiarity of particular examination procedures and

the use of technical equipment, along with patient history based on which a common sense is formed to aid the diagnosis of THR complication.

Computer aided diagnosis have became a major part of the routine clinical work for medical experts. They use the output of the computerized analysis tools/systems as a second opinion to make their final decision. The motivation is to investigate and devote computer vision and image processing techniques to create a computer assisted diagnostic tool that can interpret THR complications. To date, x-ray images are still used as the most effective diagnostic modality for detecting THR failures. Interpretation of THR images relies on the accuracy of manual observations carried out by the medical experts to detect and identify THR failures, which can be too slow, inaccurate in some cases and put both clinicians and patients under mental and physical stress. Having a computer assisted tool that reads and marks the suspicious regions of THR x-ray image would assist the clinicians to focus on those regions and have an informed insight of the surgical condition of the patients. Moreover, it aids in identifying early evidence of any THR catastrophic failure, which can reduce the need for a revision surgery and can thus improve healthcare provision by reducing the patient's bias as well as the clinician's effort required. Identifying and detecting THR complications automatically is thus the key motivation to pursue the work conducted within the research context of this thesis.

1.2. Research Gaps

Although modem imaging devices provide an exceptional view of the human anatomy, the use of computers to quantify and analyze the embedded structures in the image with accuracy and efficiency is limited due to the sheer size of the images and the technologies used for processing the images. The existing literature review conducted within the research context revealed that up-to-date the diagnostic tool

for measuring total hip replacement complications is the manual interpretation of from the available imaging modalities. Hence, there is a lack of computer assisted techniques that could automatically detect and assess these complications. The need of computer aided tool to mark suspicious region or reveal specific abnormalities within THR may used to alert medical expert to these regions during image interpretation, improve clinical decisions and aid patients considered for revision surgery. The research presented within this thesis address the existing gap of an image analysis-based technique for the automatic detection of three of the most common complications within Total Hip Replacement (THR) surgery, namely Loosening, Subsidence and Infection.

1.3. Aim and Objectives

The aim of this research is to investigate and develop a robust computer assisted tool for automatically detecting the presence of surgical complications in THR images. The specific complications investigated include the detection of loosening, subsidence and infections. Following are the objectives of the proposed research that are aimed at delivering the above:

- To develop a robust and efficient algorithm to extract prosthesis and obturator foramen automatically from THR x-ray images.
- To develp a method to traverse the prosthesis boundary of a THR image, determining key-points on the boundary that are used as points of reference to automatcially detect loosening in THR x-ray images.
- To develp an algorithm to automatically detect subsidence in THR x-ray images via computing the pixel value gradients of across the surface of the prosthesis around respective regions identified by the key-points.

- To develop an algorithm to automatically detect the presence of infections in THR x-ray images via computing the pixel value gradients of across the surface of the prosthesis around respective regions identified by the key-points.

1.4. Contribution of Research

The original contributions of the research conducted within the research context of this thesis has contributed state of art number of noval ideas that provides practical solutions for the most devasting THR complications. These contributions are presented in detail in chapters 2 to 6.

1. The literature review presented in Chapter 2, covers existing work on manual, semi-automatic and automatic computer based approaches to the detection of THR complications. Alternative existing methods used to detect some of THR complication are also presented. It is noted that such a review of literature in the area of computer based detection of THR complications have not been presented in previous literature. Thus the literature review is a contribution to the current and future research community involved in this area of research.

2. Two novel contribution were presented in Chapter 3 that focus on methods that can be used to automatically segment two important objects of a THR image, the prosthesis and the obturator foramen. For the novel algorithms presented in Chapters 4-6 requires the accurate detection of the boundary of the prosthesis and surgical complications that are to be detected are visible just outside the boundary of the prosthesis. An Active Contour Model (ACM) based approach is used to extract the prosthesis. In order to make the ACM approach fully automatic, a method to automatically select the seed point is proposed using circle detection algorithm wherein the centre of the circular area of the prosthesis is found. The literature review conducted within this thesis revealed that previous approaches proposed for the

detection of misalignment suffered from the need to manually annotate the boundary of the obturator foramen, proposes the effective use of an ACM based approach to automatically select it. The work presented in this chapter is novel and contributes to the current state-of-art in research in THR based imaging.

3. A novel contribution is presented in chapter 4, that automatically detects the presence of loosening in THR x-ray images. The algorithm initially determines important key-points on the contour of the prosthesis that are relevant to the identification of loosening. Subsequently in relation these key-points and points surrounding them, it carries out a calculation of pixel value gradients across the prosthesis boundary to determine the presence of loosening. The algorithm has been designed based on knowledge captured from expert radiographers and medical specialists and have been tested and evaluated on a sample set of images annotated by such specialists.

4. A novel contribution is presented in Chapter 5, that automatically detects the presence of subsidence in THR x-ray images. The algorithm initially determines important key-points on the contour of the prosthesis that are relevant to the identification of subsidence. Subsequently in relation these key-points and points surrounding them, it carries out a calculation of pixel value gradients across the prosthesis boundary to determine the presence of subsidence. This algorithm has been also designed based on knowledge captured from expert radiographers and medical specialists and have been tested and evaluated on a sample set of images annotated by such specialists.

5. A novel contribution is presented for the automatic detection of the presence of infections in THR x-ray images in Chapter 6. The algorithm has been designed based on knowledge gathered from medical experts having experience in THR image diagnostics. It is based on the calculation of pixel value gradient changes across cross sections around the end of the stem area of the prosthesis where infections are most likely to happen. The proposed algorithm is tested on a number of images which has been annotated by medical specialists to have and not to have infections.

1.5. Thesis Structure

For clarity of presentation and ease of reference; in figure 1.2 below we present a procedural flow diagram that relates to the thesis structure. Additional experimental results presented in appendix as approparite.

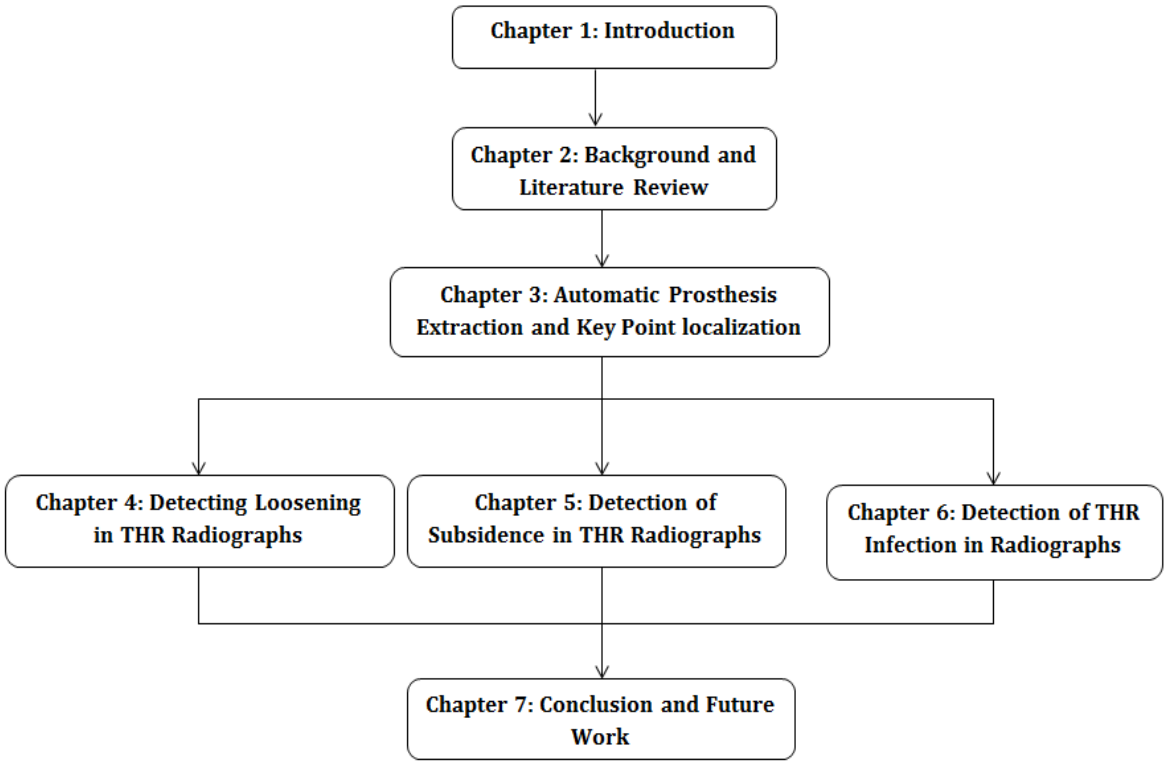

Figure 1. 1: The structure of the thesis

A brief summary of the work presented in each chapter can be presented as follows:

1. **Background and Literature Review**: Chapter 2 begins with a brief presentation of concepts and terminologies used within Total Hip Replacement surgical procedures and an introduction to the various surgical complications that can occur in THR. This is

followed by a comprehensive literature review that covers existing work on manual, semi-automatic and computer based automatic approaches to the detection of THR complications. The chapter ends with a presentation of a number of theoretical and mathematical concepts on which the contributory work of the thesis is based on.

2. **Automatic Prosthesis Extraction and Key Point localization:** Chapter 3 focuses on methods that can be used to automatically segment two important objects of a THR image, the prosthesis and the obturator foramen. Initially the chapter presents a Thresholding based approach to the segmentation of the prosthesis. However this leads to a semi-automatic process that is not practically useful. Therefore an Active Contour Model (ACM) based approach is presented as the recommended approach to the extraction of the prosthesis automatically. The chapter finally proposes the effective use of an ACM based approach to automatically segment obturator foramen.

3. **Detection of Prosthetic Loosening in THR Images:** Chapter 4 proposes a novel algorithm that automatically detects the presence of loosening in THR x-ray images. The algorithm initially determines important key-points on the contour of the prosthesis that are relevant to the identification of loosening. Pixel value gradients of those key points and the surrounded keypoints is calculated to determine the presence of loosening.

4. **Detection and Localization of Interest Point to Diagnoses Subsidence in THR Radiographs:** Chapter 5 proposes a novel algorithm that automatically detects the presence of subsidence in THR x-ray images. The algorithm initially determines important key-point on the contour of the prosthesis that are relevant to the identification of subsidence. Subsequently in relation this key-point, the relevant region is segmented and calculation of pixel value gradients is calculated across the segmented region of prosthesis boundary to determine the presence of subsidence.

5. **Detection of THR Infection in Radiographs:** Chapter 6 proposes a novel algorithm for the automatic detection of the presence of infections. The algorithm is based on the calculation of pixel value gradient changes across cross sections around the end of the stem area of the prosthesis where infections are most likely to happen.

6. **Conclusion and Future Work:** Chapter 7 finally concludes the thesis providing an insight into the possible future improvements and extensions of the novel algorithms presented in Chapters 3-6.

Chapter 2.

Background and Literature Review

2.1. Introduction

This chapter presents the process of Total Hip Replacement (THR) and describes THR complications and their clinical measurements and analysis that are performed by noting their positions and features. Many clinical and radiological methods used for the above process vary in degrees of accuracy of measurement of total hip replacement complications which are often limited to the clinical interpretation. Therefore, the presented literature review in this chapter is divided into three subsections in an attempt to thoroughly cover all related work within this domain. This clinical information is important in our attempt to propose computer vision based automated algorithms for the identification of THR complications.

In addition to describing the clinical process around identification of THR complications, this chapter covers the theoretical background behind the very few attempts made to automatically process THR images proposed in literature and associated computing research.

For clarity of presentation, this chapter is divided into several sections. Section 2.2; describes the clinical background of THR and its possible complications. Section 2.3; provides a detail literature review of computing based research proposed in the past for automated analysis of THR images. Section 2.4, presents the preliminary theories of image processing that are instrumental in the design of

the novel algorithms for the detection of THR complications proposed in this thesis. Finally section 2.5 briefly summarises and concludes the chapter.

2.2. Clinical Background of THR and its Complications

To fulfill the purpose of this study, we briefly present the medical terminologies related to THR and its complications that provide an understanding of their medical diagnosis. All THR medical diagnosis performed by medical experts support concepts that can be designed, implemented and integrated into their intelligent, automated computer based diagnosis as presented in chapters 4 to 6.

2.2. 1 Total Hip Replacement

Total Hip Replacement (also known as total hip arthroplasty) can be counted among the most spectacularly successful innovations of modern medicine. THR is a surgical procedure where the hip joint is replaced with an artificial joint called a ***prosthesis*** as illustrated in figure 2.1. This consists of a ball component, made of metal or ceramic, and a socket, which has an insert or liner made of plastic, ceramic or metal [1]. The prosthesis is carefully fitted into the thighbone and acetabulum, allowing the joint to move smoothly in multiple directions, functioning as a normal hip, so the patient can get back to their usual life. However, this induces prominent changes internal to the human body.

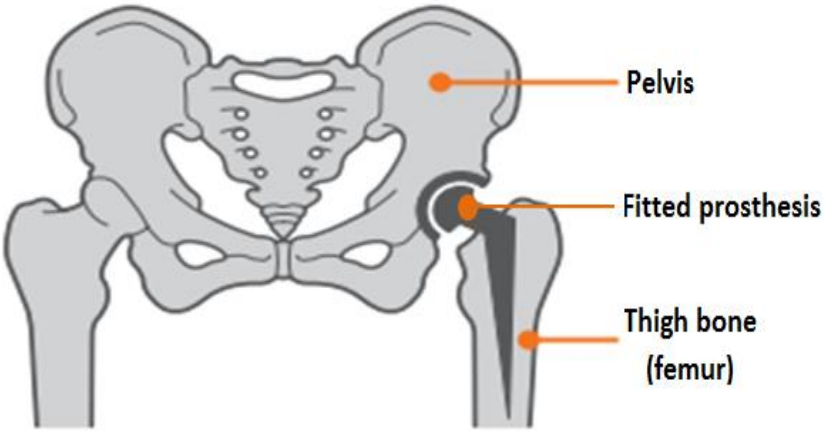

Figure 2. 1: An artificial hip joint

Implants, like any surgery do not come without risk or complications. A growing number of implant recipients have experienced implant failure and other severe complications associated with their hip replacements. The majority of the post-operative complications of THR are mechanical failures such as subsidence, dislocation, misalignment, loosening and deep infection as well as fractures. The specific causes of these complications include cup malrotation, trochanteric migration, and decreased femoral offset [81]. These complications often require revision. Hip revision surgery involves the removal of the former implant, the cement (if applicable), the surrounding tissues and any bone fractures. With over 7,000 revision THRs per annum within the United Kingdom [4], this is an economic drain and more significantly distressing for the patients. Additionally, revisions show a higher rate of infection and poorer performance [5] as compared to the original surgical processes carried out. However more recently the approaches to THR has changed substantially with the invention and use of newer fixation techniques and devices that have been introduced for both cemented and un-cemented implants, significantly reducing the need of revisions in THR surgery.

Despite this the need for revisions still remains high has motivated the review of literature in this thesis.

2.2. 2 Total Hip Replacement Complications

THR surgery does not come without risk. In long term, THR surgery may induce complications. In this section we describe the most common THR complications and their potential clinical aspects of interpreting, identification and analysis.

2.2.2.1 Loosening

Loosening is clinically known as aseptic loosening. Loosening refers to harmful mechanical and biological events caused by osteolysis. It destroys the functionality of the implanted prosthesis and is associated with chronic pain and loss of motion. Osteolysis affects bone volume; the bone is continuously lost and replenished. As a matter of fact, the ration of bone resorption to bone formation controls the volume of bone at all times: at a younger age, the level of formation exceeds resorption, while in older people, the opposite is true. The condition of osteolysis causes bone resorption to exceed bone formation, causing a loss of bone volume, which leads to faster loosening around the prosthetic interface. There is no general definition of loosening in THR; however, in clinical practice, loosening is assessed indirectly by measuring radiolucent dark lines around the prosthesis and assessing the positional variances of the prosthesis relative to the bone. The radiolucent lines indicate the absence of a cement layer around the prosthesis as in

Figure. 2.2. As described earlier, the prosthesis is tightly fitted into the bone, but if the implant loosens, a widen region appears as a radiolucent zone between the prosthesis and bone. This can be seen in figure 2.2 (b), the x-ray image has radiolucent lines across the boundary of the prosthetic. Gruen [6] described seven sections around the femoral component figure 2.2(a) as "zones" in a system used for the evaluation of THR loosening. Cemented implant components generally show a tiny (1-2mm) radiolucent zone at the cement interface. Nevertheless, if these radiolucent lines progress over time to exceed 2mm at the cement-bone interface, then it becomes a lucent prosthetic, as shown in figure 2.2(b). However, clinical decisions on whether there is loosening or not vary from surgeon to surgeon with regards to radiolucent lines.

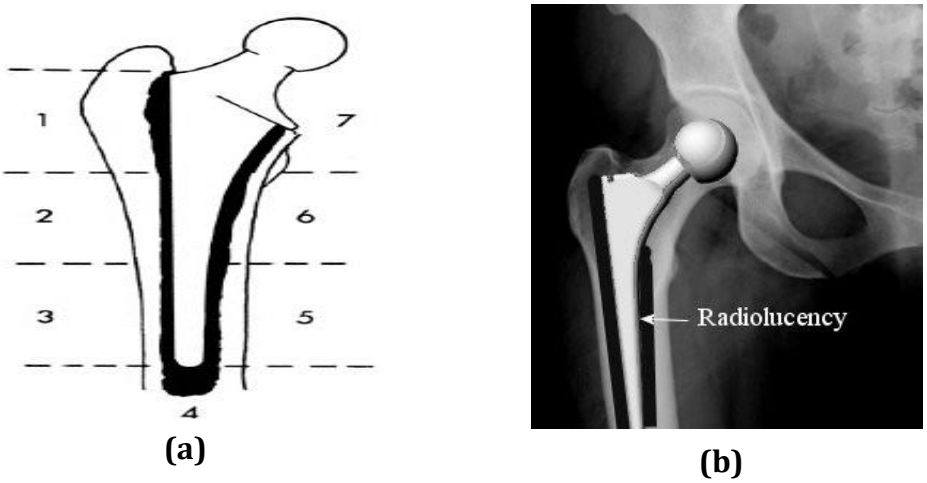

(a) **(b)**

Figure 2. 2: (a) Seven Gruen zones around the femoral component and (b) Radiolucency of the femoral stem

2.2.2.2 Subsidence

Subsidence in THR is a gap between the convex of the prosthetic border and the cement. The prosthesis is placed into the hip either by pressing fit into the bone or cementing it into position, so it fits tightly and is perfectly aligned with the bone; this region can be described as “fixation of the THR” where the prosthesis is fitted into the bone or with cement. If there is any imperfection in the anatomical structure of prosthetic and bone, which may appear as a cavity within the prosthetic and bone, then this is logically described as subsidence of the prosthesis within the cement figure 2.3. This transverse gap between implant and bone can measure more than one or two millimeters.

This is a phenomenon that applies to all femoral stems, regardless of the surface finish, type of prosthetic and presence of cement. Thus, subsidence refers to the condition in which the prosthesis unexpectedly subsides vertically further into the bone.

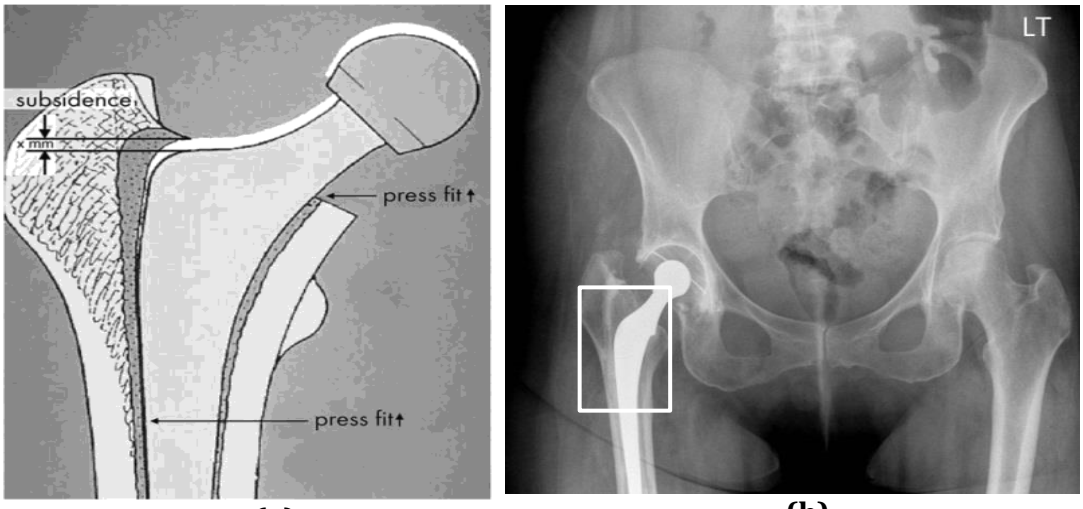

(a) **(b)**

Figure 2. 3: (a) Subsidence of a tapered femoral stem (within the cement) press-fit[74]; (B) An x-ray image of THR complication (Subsidence and also loosening)

One of main differences between subsidence and loosening is that with subsidence, the gap can is measured between the cement and the convex of the prosthesis, as shown in figure 2.3, while loosening is measured as radiolucent lines (or gap) around the broader part of the prosthesis, as shown in figure 2.2.

2.2.2.3 Infection

An infection after total hip replacement is another of the most devastating THR complications. Infection is a bacterial invasion of the hip joint [7]. It is also known as septic loosening. It is rare in orthopaedic surgeries; nevertheless, it is challenging to eradicate. The reason for this is that there is neither a standardised diagnosis nor treatment for it, despite the considerable progress that has been made in the medical field. Zimmerli [8] describes three categories of infection associated with prosthetic joints. According to Widmer [9], the first type involves early manifestation: the signs and symptoms appear during the first three months after surgery; some authors limit these surgical site infections to the first two to four weeks, as this is anticipated in surgery due to the potential for intraoperative contamination or healing disturbance during the perioperative period. The second type is a more delayed infection considered low-grade. The signs of this type of infection can appear between three months and two years after surgery, and usually also indicate an early sign of loosening. Lastly, late manifestation is defined by the appearance of the signs and symptoms of infection more than two years after the surgery. These infections appear either with a sudden systemic inflammatory response syndrome [10] or without any initial signs. If, despite treatment for infection using antibiotics and other medications, the infection cannot be exterminated, the implant prosthetic has to be amputated and in the most extreme cases, the leg may also be surgically removed. It is a serious potential problem that occurs in the area of the wound that indiscriminately spreads, but doctors look for

the clinical signs around the implant in patients' radiographs, as well as using laboratory investigation of infection parameters to identify whether there is an infection or not.

Accordingly, one can technically diagnose infection from radiographs by looking for these clinical signs, as x-ray images have various intensity levels of grey, as a human eye can differentiate various organs and tissues. In normal x-rays of THR, the prosthetic appears as the brightest object that, perfectly aligns with the cement and the bone, as illustrated in figure 2.4(a).

(a) **(b)**

Figure 2. 4: X-ray image of (a) uninfected THR and (b) infected THR

In abnormal x-rays, although the prosthetic appears as the brightest region, there is gap between the prosthetic and the cement. The element of perfection in the alignment of implant and cement is missing, as can be observed in figure 2.4(b). The highlighted region indicates dark pixels at the bottom of the implant and this might be diagnosed as an infection taking into account the shape of the dark pixel region.

2.2.2.4 Dislocation and Misalignment

Dislocation of a total hip replacement is the second most common cause of revision after aseptic loosening [11]. Hip dislocation occurs when the prosthetic head (femoral component) is dislocated from the cup (acetabulum component) as in figure 2.5(a). This complication is a serious cause of morbidity in patients and a substantial burden on healthcare costs. The risk of dislocation is common in the first few months after surgery. It decreases once the first year is passed, when the tissue strength has recovered. However, beyond the first postoperative year, the cumulative risk of later dislocation continues to rise slowly over time, at a rate of 1% every five years [12]. Dislocation leads to various posterior directions that clinically cause shortening of the leg, flexion and rotation of the internal implant components. This weakness may be accompanied by fractures of the acetabulum, soft tissue injuries or misalignment, which is barely visible in x-ray images. Improper alignment of the implant after hip replacement surgery can cause loosening of the hip, pain and hip wear. It may also cause post-operative hip dislocation of acetabular cup as illustrated in figure 2.5(b). Due to the lack of a definition of what constitutes a correct target of misalignment, we refer to misalignment as an inaccurate or misaligned position of obturator foramen. Obturator foramens refer to a large opening of the innominate in pelvic bone as shown in figure 2.5(b).

(a) **(b)**

Figure 2. 5: X-ray image of (a) dislocation THR and (b) misalignment THR

Although the vast majority of THR surgeries are successful; many patients experience minor side effects or serious and painful side effects especially in long run. It is necessary to monitor the level of the side effect to prevent further medical following falls.

2.3. Literature Review

Much of the literature related to the identification of total hip replacement complications is based on administered procedures that require manual assessment of radiographs, ranging from labour-intensive measurements of radiographs to semi-automated computer applications that employ image processing techniques. Due to the research context and the vast amount of literature that details manual or clinical radiographic interpretation of THR, we categorize the literature into three different subsections. Methods that automatically or semi-automatically assess THR

complications, which utilise image processing techniques are presented in subsection 2.3.1. Manual interpretation of THR complications is presented in subsection 2.3.2. Finally, prospective methods that deal with THR complications using alternative tools other than computer based applications is presented in subsection 2.3.3. However, for the purpose of this research; the first category of literature has been reviewed more widely.

2.3.1 Automatic/Semi-automatic Assessment of THR Complications

An initial unpublished study measures dislocation in total hip replacement used hough transform and filter back projection algorithm proposed by *Otoum et al.[13]* to identify whether the prosthetic head(femoral head) is perfectly co-centered within the cup (Acetabulum) or not. It quantifies key points of the prosthetic head and measures the distance between the centre points of the prosthetic head and the cup. It searches for two circles with two different radius values to locate the centre of circles as described above. This study also measures misalignment in THR by defining differences in length between two perpendiculars points on the tearbone by drawing straight a line from the centre of prosthetic head to a straight line that connects the two key predefined points on the teardrop bone. *Otoum et al. [13]* stated that measurements of both dislocations and misalignments are taken to compare with acceptable tolerances provided by the medical specialist's in-order to define if the values are larger than the tolerances provided then cases are marked as positive. However, the experimental results presented are not correlated to measurement of the efficiency of this method.

Another publication by *Komeno et al. [14]* examines proper position of the cup and the stem of a THR system, after total hip arthroplasty. This method measures the cup and stem anteversion using computed tomography (CT). Cup anteversion is measured as an angle between the line connecting the anterior edge with the posterior edge of the cup and the vertical line against the line connecting the posterior portions of the pelvis in the slice passing through the centre of the cup. On the other hand, the stem ante-version is measured as an angle between the line connecting the posterior part of the femoral condyles and the axis of the stem superimposed sequentially. The sum of cup and stem ante-version in posterior dislocated hips is significantly lesser than that of the non-dislocated hips and the sum in anterior dislocated hips is significantly greater than that of the non-dislocated hips. According to the results of this study, the implant should be placed approximately at a 50° angle of the sum of cup and stem anteversion. To prevent posterior dislocation, only the anteversion angle of the cup should be increased rather than that of the contralateral acetabulum. However, this method has not taken into account the impingement of the femoral head and osseous pelvis.

As per the automatic/semi-automatic segmentation of the THR components from radiographs Oprea *et al.* [15] investigated the use of several classical adaptive region segmentation techniques, using either the initial pixel luminance space (adaptive histogram thresholding), or an extended feature space (Fuzzy C-Means) to automatically segment the x-ray images into clinically relevant parts: prosthesis, bone (femur), soft tissue etc. The segmentation quality was evaluated by using the standard detection error and ROC (Receiver Operating Characteristics) curves. This method reveals that FCM segmentation provides superior performance for the segmentation of all image components that can be used as image analysis methods for a computer-assisted diagnosis system.

Later on, Florea et al. [16] created another method to extract objects from x-ray images for automatic analysis. They presented a model of a femoral bone with a

set of three non-concentrically cylindrical shapes (the bone, the medullar and prosthesis). The initial step of the method is based on histogram segmentation of image components, and then a Canny edge operator was used to determine the edges followed by 3D modelling of the femoral bone. The prosthesis is measured to be fit inside the medullar bone. Then prosthetic-bone fit percentages were measured that were simultaneously carried-out on the prosthetic and medullar channel borders. This study indicated that the measurements are valid on the prosthesis fit inside the femoral bone and it determines the exact position of the composing parts (segment the x-ray images). However the measurements were limited to recognizing certain hip areas in the x-ray images. In [17] Smith *et al.* proposed a new segmentation technique that was described using a hierarchical method of three key structures from pelvic x-ray images: the ilium, and the left and right acetabulums. First, Directed Hough Transforms were used to detect the femur shafts and to correctly determine the patient's horizontal position within the image. Then the Hough transform was combined with Active Shape Model (ASM) to detect the femur and in turn, the acetabulum. The position of the femurs is used to initialize ASM for pelvic ring detection, and the location of the pelvic ring. Subsequently direct Hough transform was used for the detection of the iliac crests. This method detects fracture of structures from initial patient x-ray s that may assist physicians in the diagnosis and advice for proper treatment.

Barker *et al.* [18] measured subsidence of the femoral components that relies on the implantation of two ball markers around the femoral stem. Stem dimensions were used to correct magnification and out-of-plane rotations resulting from radiographic positioning. To measure subsidence, the position of the hip implant surrounding the bone and the cement were determined via circular Hough transform based techniques. In conjunction with a Sobel edge operator the center (radius) of the femoral head components and location of the spherical markers were located manully. This technique has as advantage of minimizing the variation in landmark positions by incorporating image processing algorithms and measuring

the axial migration of the specific design of implant used in total hip replacement. However, to assess the subsidence; relevant implant dimensions are required.

Downing et al. [19] developed a method that automatically classify different sections of the THR model from standard clinical radiographs using three separate techniques. Reference axes are defined and a template is matched to magnify and correct femur extraction. Measurements compared within and between patients giving quantified measurements of bone thickness, cement radio-lucency and prosthesis positioning. They define lucency using image intensity profile and to aussre the accuracy of the method they will apply the method to a larger set of images. However, using the image intensity profile may lead to inaccurate results because the intensity of the image is highly affected by the light illumation of the device which the x-ray is taken. As it clearly indicated that more testing required to prove the effectiveness of the proposed method.

Hardinge *et al. [20]* developed a computer-based image analysis system for total hip replacement. This system enhances poor quality radiographs and takes multiple measurements from coronal plane radiographs. Measurement of stem subsidence, cup migration, cup wear, and stem loosening were obtained as well as reproducibility and accuracy were ± 0.01 mm and ± 0.5 mm computed respectively. The present application is in retrospective research, but prospective monitoring of radiographs is planned.

A recent study conducted by Sahin et al. [21] proposed a new segmentation method to determine boundary of obturator foramen. Marker-Based Watershed segmentation method and Zernike moment feature descriptor were used to detect obturator foramen. The region of interest was first manually extracted and then a Marker-Based Watershed segmentation method is applied to the region of interest. Subsequently the Zernike moment feature descriptor is applied to segmented region of interest. Zernike moment feature descriptor is used to provide the

required matching between the binary template image and the segmented binary image for final extraction of Obturator Foramens. Pelvic bone rotation rate is automatically measured for each hip radiograph to prevent having to choose processing images for further angle measurements, which are based on pelvic bone structure.

A number of related publications of wear estimation in THR have been proposed in [22, 23, 24]. Kerrigan et al. [22] used active ellipses to measure the wear in THR. Radiographs are manually annotated and the boundary of the femoral head and acetabular rim are learned. Two ellipses are drawn on the radiograph, the first deformed around femoral head whereas the second is placed using the previously learned average shape of the acetabular rim. The distance between centres of two ellipses calculated and converted to mm is a measure of wear. This method quantifies displacement of centre of the femoral head is proportional to the centre of the acetabular rim.

Later on Kerrigan et al. [23] proposed a method that automatically localises displacement of femoral head and acetabular rim. A wire marker is attached to the acetabular component of the prosthetic where a projection of an ellipse is modelled. The centre of ellipse is used as a reference point to estimate wear. 3D poses of acetabular cups estimated from projected ellipse parameters that were also used to estimate the expected error values. The wear measurements to correct these errors were investigated using standard clinical anteroposterior radiographs and an automated ellipse fitting method. Yet, Kerrigan et al. [24] assess the active ellipse method for latter wear cases and the distances measured revealed as very eccentric and inadequate. The fit functions were compared, including a geometric error of fit function, on both synthetic data and by using active ellipses on a set of test radiographs that has eccentric rims. Least squares were estimated using a geometric error function that provided most accurate presence of Gaussian noise. This method has a drawback that it is computationally

expensive and in applications where speed is important the foci bisector distance is recommended as an error of fit function.

2.3.2 Manual Interpretation of THR Complications

Kaneuji et al. [25] clinically deliberated the relationship between stem subsidence and the improvement in the initial radiolucency at the bone cement interface in polished- and rough-surface stems in radiographs. The outcome of this study state that stem subsidence was seen in 34 of 42 hips (81.0%), and improvement in the initial radiolucency was seen in 15 hips (35.7%) in collarless polished tapered stems at 1 year after operation. The key indication of this study is radiolucent lines around the stem in THA is generally considered a sign of implant failure; this destruction is presumed as stem subsidence or a contrary sign of loosening if the cement moves in the femoral canal. Similar radiological signs of subsidence were validate by Loudon et al. [26] the clinical outcome were compared with femoral subsidence and radiographic changes in 102 patients at 9 to 13 years after low friction arthroplasty. Loudon et al. [26] also measured radiological subsidence of a femoral prosthesis in relation to the femur after total hip arthroplasty using the ruling method on radiographs. This method measure the distance from the tip of the femoral prosthesis to a fixed point in the bone by placing the radiograph on a horizontal viewing box and two mid-points are measured on the distal (straight) part of the stem then marked on the film. A line is drawn to indicate the central axis of the stem between these marked points. However, Loudon et al. [26] addressed that it is difficult to quantify subsidence of the prosthesis as an a gap between the convex lateral surface of the upper part of the stem of the prosthesis and the adjacent cement due to the appearance of the prosthesis on radiographs. Smith et al. [27] assessed the clinical and radiological signs of prosthetic loosening using the electronic picture archiving and communications system (PACS) to reduce the risk of pre-prosthetic fractures and

significant loss of bone. They used the three common radiological assessments of total hip arthroplasty (THA); Barrack, Gruen and Hodgkinson. The findings indicated that the Hodgkinson system is the most reliable in evaluating femoral and acetabular loosening. Massoud et al. [28] conduct a study on aseptic loosening of the femoral component in 76 patients with primary total hip replacement using the Capital prosthesis. The evaluated radiological criteria of femoral component radiological loosening are divided into two categories. Definite loosening is migration of the component as demonstrated by a change in alignment in figure 2.6 or more than 2 mm of subsidence in figure 2.7. The potential loosening was defined as the appearance of a radiolucent line of up to 2 mm at the cement-prosthesis interface that had not been present on the postoperative radiograph in figure 2.6 & figure 2.7.

Figure 2.6:Definite loosening with change in alignment at 30 months [28].

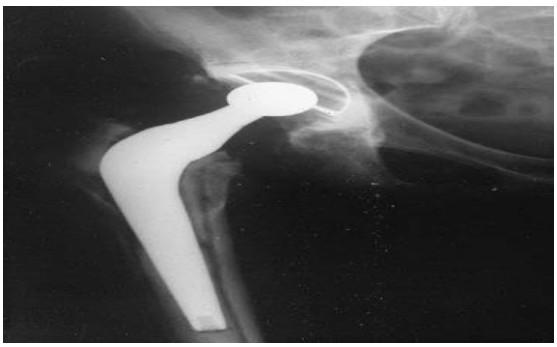

Figure 2.7:Definite loosening with cement fracture and subsidence at 22 months [28].

Another publication of Kinov et al. [29] argued the controversy in diagnosing value of bone scintigraphy and laboratory tests in patients suspected to have loosening of the hip arthroplasty. Seventeen patients hip radiograph were examined with conventional radiography and three-phase bone scintigraphy. Microbiological examination results of joint aspiration and surgical specimens (9 patients), plus, C-reactive protein level (CRP) and erythrocyte sedimentation rate (ESR) test, as well as clinical follow-ups were evaluated on the radiographs. Five hips had septic loosening (infection) and three hips had aseptic loosening. In the remaining twelve cases, neither loosening nor infection was confirmed. For diagnosing infection radiography and bone scintigraphy, respectively, sensitivity values were 62.5% and 87.5%; specificity - 80% and 91.6%; and accuracy 85% and 90%. For ESR and CRP, respectively, sensitivity values were 60% and 100%; specificity - 100% and 70%; and accuracy - 86.7% and 75%. In a study population of patients suspected of having infected total hip replacements, three phase bone scintigraphy performed better than conventional radiography, ESR and CRP tests. Mulcahy et al.[30] carried out a systematic review on radiograph assessment of hip arthroplasty. He included different types of techniques, terminologies for prosthesis design, surgical techniques, initial and follow-up radiographic assessment etc. He proposed the measurement of leg discrepancy by drawing a line connecting the tips of both teardrops and drawing a vertical bisector from each teardrop. Superior aspect of the tip of lesser trochanter was marked followed be drawing a line joining both ischia tuberosity. The Teardrop lies in the inferomedial portion of the acetabulum, just above the obturator foramen. Vanrusselt et al.[31] also provided an pictorial review with systematic guidelines for the radiographic evaluation of a prosthesis hip.

2.3.3 Alternative Methods used in Assessment of THR Complications

Ruther et al. [32] investigated the use a passive sensor array that was based on the interaction between magnetic oscillators inside the implant and an excitation of coil outside the patient. The main concept is to excite several magnetic oscillators inside the THR to impinge and to produce a sound in the audible range. The excited oscillators create audio signals that vary according to the amount of loosening. After several experimental tests, the sensor array was optimized to guarantee reproducible and selective excitation of the sound emission. To increase optimization of measuring system; a numerical simulation of boundary was designed using a cylindrical and C-shaped coil. The numerical simulation showed the behavior of coils during application and how the magnetic field characteristics are developed. According to these investigations, the passive sensor system reveals the potential of detection of implant loosening in THR.

A different concept was adopted by Valstar et al.[33] that used roentgen stereophotogrammetic analysis (RSA) to obtain accurate 3D measurements of radiographs for measuring migration of the prosthesis. This technique involves insertion of tantalum markers where two x-ray sources placed at approximately 1.6m above the film at a 20^{o} angle to the vertical [33]. The accuracy of RSA ranged between 0.05 and 0.5 mm for translations and between 0.15^{o} and 1.15^{o} for rotations. The RSA method was tested on a small group of patients due to the changes in implant design and by measuring micromotion of a prosthetic in a short-term (i.e. 2 years) clinical RSA study, a prediction can be made on the chance of long-term (i.e. 10 years) loosening of the prosthesis. This method has been used to screen new developments in prosthetic design as well as to prevent patients from being exposed to potentially inferior designs. Gergiou et al. [34] examined the

potential role of vibration testing as a non-invasive method of diagnosing loosening of total hip replacements in the clinical setting. A vibranting device is placed on the patient's knee and ultrasound device is attached to the patient's hip. The sound frequency generated by vibrating femur and hip is measured where, constant increase and decrease in frequencies show that the implant is still attached to the bone and if the frequencies are irregular then it indicates that the implant has loosened. A comparison study is carried out between the vibration testing and radiographs in patients with loosening of total hip replacement. Although the results were satisfactory, this technique has limitations: it is unsuitable for patients who cannot lie on their side or who experience pain induced by vibrator. In addition, the vibration testing was performed in the early stages of development of instability of total hip replacements. The study used a different approach to identify the loosening; radiographs remain the most popular and practical tools used in assessing THR complications in medical field.

Kristanto et al.[35] adopted a Gradient Vector Flow snake (GVF) method to perform a semiautomatic planning for hip joint replacement surgery using a special medical image viewing software, ViewPro™. The preoperative planning is calibrating the hip x-ray image to adjust the magnification factor by applying GVF snake algorithm to detect the reference object. Manual user interference has been reduced significantly, therefore, the process become more user-friendly. A study has been performed to compare the newly developed semiautomatic algorithm to the old manual calibration algorithm. The results show a close relation between the two algorithms with less than 1% of average relative difference. It concluded that the developed semi-automated algorithm can be used as an alternative for performing the manual calibration.

A divergent study describe an algorithm of infection detection in x-ray images of lung carried out by Habib et al.[36]. The proposed algorithm adjusts image intensity and converts it to grey scale as a pre-processing step. Then a

gaussian filter is used to remove any false structure in the x-rays. To extract the lung from the x-ray image, image thresholding is carried out followed by dilation and erosion morphological operations. A flood fill algorithm is applied to localize the infected area in x-ray images. This study used basic image processing techniques to define the infected region in lung in radiographs automatically. It aims to improve radiation treatment and increase survival rate via accurate diagnosing of the disease.

2.4. Fundamental of Image processing Techniques Related to Research Problem

This section introduces the fundamental theories of image processing that are core to building novel systems/applications for computer-assisted diagnostics of THR images as presented in this thesis from chapter 3-6.

2.4.1 Image Segmentation and Enhancement

Image segmentation has a broad range of applications in image processing, computer vision, object recognition and tracking. In all of these applications, the grey level information of an x-ray image can be ignored due to the bi-level information that creates a cluster of gray level pixels which may make it hard to classify an object because of intensity inhomogeneity. Segmentation is the step of dividing digital images into multiple segments or categories that correspond to

different objects or parts of objects so it is easier to use and more meaningful for any further analysis.

2.4.2 Wiener Filter

A significant number of image enhancement techniques are available in image processing; however, the Wiener is "2-D adaptive noise removal filter" is the most appropriate algorithm for enhancing the anatomical visualization of bone in x-ray images. It reduces the noise of images based on statistical estimation from the local neighborhood of each pixel [39]. It also known as the low pass filters of greyscale images, which are degraded by the constant power of additive noise. For example, to calculate the Wiener filter we assume that the filtering image is corrupted by signal-independent, zero-mean adaptive white Gaussian noise, as follow:

$$Y(i) = x(i) + n(i,j)$$

where, *Y(i, j)* is the noisy image, *X(i)* is the ground truth image and *n(j,j)* is additive Gaussian noise. In order is to remove noise *n(i,j)* and get a linear estimate $\hat{X}(i)$ of *X(i)* that minimises the mean squared error (MSE), the following equation is utilised:

$$MSE(\hat{X}) = \frac{1}{N}\sum_{i=1}^{N,M}\left(\hat{X}(i) - X(i)\right)^2 \qquad (2.1)$$

where *N,M* are pixels in an image of *X(i)*.

When *X(i)* and *n(i, j)* are stationary Gaussian processes, the Wiener filter is the optimal filter [40], especially when *x(I, j)* is likewise a white Gaussian process. The Wiener filter is estimated using (2.3):

$$X(i,j) = \frac{\sigma_x^2(i,j)}{\sqrt[2]{\sigma_x^2(i,j)+\sigma_x^2(i,j)}}[Y(i,j) - \mu_x(i,j)] \quad (2.2)$$

where σ2, μ are variances and means respectively, and if the noise variance is not given, the Wiener uses the average of all the local estimated variances. The adaptive noise removal filter provides the best restored signal with respect to square error averaged over the original signal and the noise among linear operators [40], where, if the variance is high, the filter performs little smoothing and if the variance is small, the filter performs more smoothing. This filter is adopted because it cleans out the noise that has corrupted the original signal. Design of the Wiener filter takes a statistical approach whose output will be as close to the original signal as possible.

2.4.3 Morphological Operations

Morphological operations are powerful non-linear image analysis tools used in image processing. They are based on pre-defined spatial structures, known as structuring elements (SE), used to input an image, creating an output image of the same size. The value of each pixel in the output image is based on comparison to its corresponding neighbor pixels in the input image [41]. The fundamental morphological operations are erosion and dilation. Morphological open images combine both morphological operations respectively. They eliminate all the pixels of the input image that are too small to contain the structuring element. This can be described as if the opening of the image f by SE ***b*** was set as the erosion by b followed by a dilation of the result with **b**:

$$f \; o \; b = (f \; \Theta \; b) \oplus b \quad (2.3)$$

Likewise, the closing of ***f*** by b is:

$$f \; \bullet \; b = (f \; \oplus b) \; \Theta \; b \quad (2.4)$$

The use of opening and closing images has a humble geometrical interpretation that may support the visualization of hidden geometry in an image. By adjusting the default parameters and reading the image as 3D, the representation of a pixel can have a different colour and this would not alter the actual intensity value. Assuming that the image *f(x, y)* is displayed as a 3D surface, intensity values are seen as heights over the xy-plane. The opening of ***f*** by b can be seen as "pushing" ***b*** up from below against the base of ***f***. At each location of b, the opening reaches its highest value by any part of b as it drives against the base of f. The whole opening process then covers all such values obtained by having b visit every *(x, y)* coordinate of ***f***. In brief, a morphological operation is based on set theoretical concepts of shape. It looks at an object in an image as a structuring element (SE) in order to get information about it. This structure is useful in the representation and description of a region's shape. Adapting open morphology decreases the size of small, bright details without changing the dark regions in an image. Morphological operations originally dealt with binary images only and were later extended to grey image processing [39].

2.4.4 Thresholding

The objective of image thresholding is to divide the image into regions, as it is known that in image processing applications the grey level value of the foreground or an object is different from the grey level value of the background. It is an effective way to make discrete the foreground and background. In medical imaging applications, it is more essential to clarify the distribution of tissues or organs within an image than the distribution of objects in a natural scene image. Given a single threshold *(T)* for a grey image, the binary image is created by designating pixels with less value than the given threshold as 0 and the rest of the pixels as 1. For example, if F is an image of size M x N in which *i* is the grey level,

ranged as [0,J-1] , J indicates maximum array level in the image. The brightest pixel is denoted with coordinates *(x,y)* by *F(x,y)* where *(x,y)* are points at grey level *F(x,y)*. The threshold value *(T)* is also ranged as [0, J-1] and the thresholding technique to determine an optimum value of *(T)* is based on predefined measurements, as in (2.5):

$$G(x,y) = \begin{cases} 1, f(x,y) > T \\ 0, f(x,y) \leq T \end{cases} \quad (2.5)$$

where 1 is object, 0 is background and *G(x, y)* is the binary image.

The value of each pixel in the binary image is either 0 or 1, where 0 represents black and 1 represents white. In this work, we are interested in bright objects that are represented as white on a dark background.

2.4.5 Sobel Edge Detection

Edge detection is the process of locating the edge of an image using a gradient operator to detect sharp intensity variations in the image. Sobel[42] is a common edge detection algorithm that typically corresponds to edges in the image where the gray value changes significantly from one pixel to the next. It represents regions in the image with strong intensity contrast by finding the approximate absolute gradient magnitude at each point of a greyscale image. It uses derivative approximation to find edges and returns those edges with high gradients. In other word, it performs 2D spatial gradient measurement on images, using two 3x3 masks which are convolved with the original image to calculate approximations of the derivatives for horizontal and vertical changes.

If A is the source image, G_x and G_y are two images which at each point contain the horizontal and vertical derivative approximations. The computations are as follow:

$$G_x = \begin{bmatrix} +1 & 0 & -1 \\ +2 & 0 & -2 \\ +1 & 0 & -1 \end{bmatrix} * A \;\; and \;\; G_y = \begin{bmatrix} +1 & +2 & +1 \\ 0 & 0 & 0 \\ -1 & -2 & -1 \end{bmatrix} * A$$

where $*$ represents a two-dimensional convolution operation.

The key point is to bring out the horizontal and vertical edges individually and then to put them together to detect the edge. The two filters G_x and G_y highlight areas of especially high frequency, which tend to define the edge of an object in an image. This is done by decomposing Sobel kernels as an averaging product, along with kernel differentiation; both filters compute the gradient with smoothing. For example, G_x can be written as:

$$\begin{bmatrix} +1 & 0 & -1 \\ +2 & 0 & -2 \\ +1 & 0 & -1 \end{bmatrix} = \begin{bmatrix} 1 \\ 2 \\ 1 \end{bmatrix} [+1 \quad 0 \quad -1]$$

The x-coordinate is described as increasing in the "right" direction, and the y-coordinate is described as increasing in the "down" direction. The appro results of the gradient can be combined to give gradient magnitude at each point in the image using:

$$G = \sqrt{Gx^2 + Gy^2} \tag{2.6}$$

Using this information, we can calculate the gradient's direction as:

$$\theta = tan^{-1}(Gy/Gx) \tag{2.7}$$

where, for example, Θ is 0 for a vertical edge, which means it is darker on the right side. Sobel edge detection creates an image that emphasizes the edges and transitions that contain significant information about various organs and tissues in x-rays. It also reduces the amount of processed data and filters out information that may be considered less relevant, while preserving the important structural properties of the image. The detected edge of the prosthetic can be traced further.

2.4.6 Edge Link Algorithm

The edge link algorithm has previously been used in the area of lane detection [43]. It works well on edges obtained from the Sobel operator. It collates edge pixels in an image into an organized list. A flowchart of the algorithm is shown in figure 2.8(a).

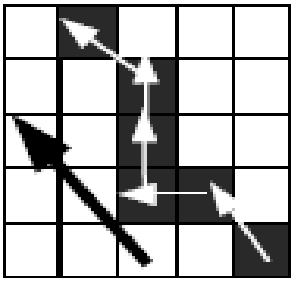

(a)

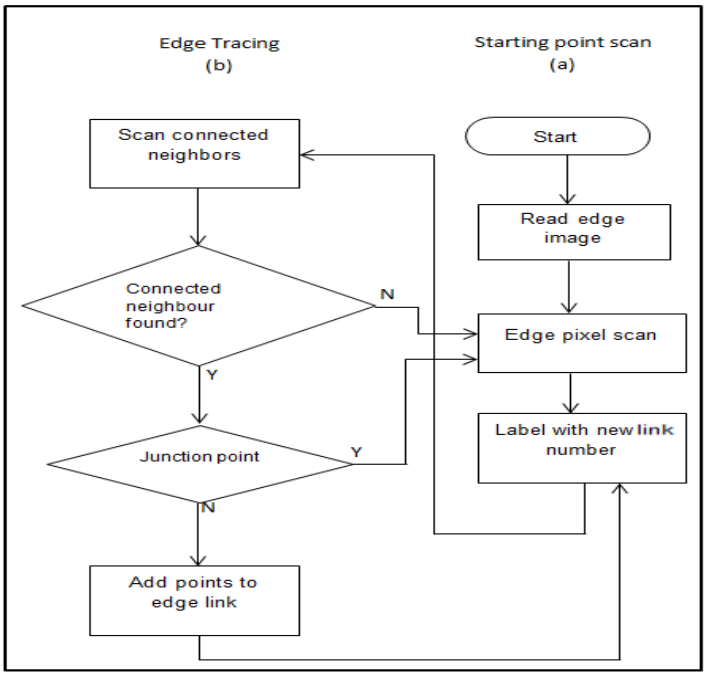

(b)

Figure 2.8: (a) Edge Link Orientation and (b) Diagram shows flow chart of edge link algorithm

First, scanning is performed from the bottom of image to locate the starting point. Once the starting point is found, the edge tracing process starts to track all the edge pixels. The next added edge pixel added to the link is the one with the eight neighboring pixels connected to the previous edge pixel. From the starting point, edge pixels are tracked in one orientation, as illustrated in figure 2.8(b), and then stored in an edge link array by edge link number. This process continues until no more connected edge pixels are found; for more details, see [43].

2.4.7 Snake Algorithm

Snake or active contours are used to define or segment particular object boundaries in an image. Snake was first introduced by Kass et al. [44] as an elastic contour extraction technique for boundary detection. The snake curve moves under influence of internal forces coming from within the curve itself and external forces computed from the image data [45]. The internal and external forces are defined so that the snake conform to an object boundary or any other desired features within an image. It called snake because of the way the contour moves while searching for an edge in image. Snakes are widely used in many applications, including edge detection [44], shape modeling [46], [47] and segmentation [48], [49], [50] and motion tracking [51]. There are two key difficulties in the implementation of parametric active contour algorithms. First, the initial contour must be close to the true boundary or else it will likely get the wrong result. Second, active contours have difficulty progressing into boundary concavities [52] and [3]. The snake active counter algorithm was further improved by Xu and Prince [54] and [55]; they developed a new external force, called gradient vector flow (GVF), which largely solves both problems. GVF is computed as a diffusion of the gradient vectors of a gray-level or binary edge map derived from the image. The result of GVF field has a large capture range, which means that the active contour can be set far away from the desired boundary. The GVF field also forces active contours into boundary concavities, where traditional snakes have poor convergence. Initially, a snake is a curve defined inside an image that moves under influence of both internal forces within the snake itself as well as external forces derived from the image data. Those forces are defined in such way where it conform an object boundary. The traditional snake is defined as *v(s) =[x(s), y(s)]*, where s ε [0, 1]. The snake moves through the spatial domain of an image to minimize the energy function:

$$E = \int_0^1 (E_{int}(v(s)) + E_{ext}(v(s))) \quad (2.8)$$

The internal energy can be written as:

$$E_{int} = \alpha(s)\left[v^{i}(s)\right]^2 + \beta(s)\left[v^{ii}(s)\right]^2 \quad (2.9)$$

Where, α and β are weighting parameters that control the snake's elasticity [44].
The traditional snake algorithm in gray-scale images uses gradient image gradient function to express the external energy as:

$$E_{ext} = -|\nabla I(x,y)|^2 \quad (2.10)$$

Where, *I(x,y)* is the image function and ∇ is its gradient.
A snake that minimizes *E* in (2.8) must satisfy the Euler equation:

$$\alpha v^{ii}(s) + \beta v^{iiii}(s) - \nabla E_{ext} = 0 \quad (2.11)$$

To solve (2.11), the snake is made dynamic by treating **v** as a function of time as well as of *s*—i.e., *v(s,t)*. The partial derivative of ***v*** with respect to ***t*** is set equal to the left-hand side of (2.12) as follows:

$$v_t(s,t) = \alpha v^{ii}(s,t) + \beta v^{iiii}(s,t) - \nabla E_{ext} \quad (2.12)$$

When the solution of *v(s, t)* stabilizes, the term v_t disappears and the solution for (2.12) is achieved. Solution for (2.12) can be found by making the equation discrete and solving the discrete system iteratively [55].
The snake algorithm is then developed and include gradient vector flow snake (GVF). GVF replace the external force term in equation (2.12), which is $-\nabla E_{ext}$ .So, GVF is defined as a vector field *g(x, y) = (u(x, y),v(x, y))*. Thus, the energy function becomes:

$$v_t(s,t) = \alpha v^{ii}(s,t) + \beta v^{iiii}(s,t) + g \quad (2.13)$$

An edge map of the image *(f(x, y))* is needed to make a GVF field. The edge map is derived from the image data and has larger values near the edges as it is known that gradient image are sufficient to map an edge. The GVF is a force field that minimizes the energy function [55].

2.4.8 Curvature of a Planar Curve

Edges in images are low-level features that can be recognized by human vision. Curvature is used to analyze the edges of low features in images. It is also known as the two-dimensional shape analysis technique in pattern recognition and image analysis applications. Curvature is defined as the rate of change in the direction of the edge.

Mathematically, curvature is considered a parametric form of planar curve [56]. This is represented using the parametric form:

$$v(t) = x(t)U_x + y(t)U_y \tag{2.14}$$

where, *x, y* are coordinate points along a continuous curve, t is a parametric value between 0 and 1 and U_x=[1,0], U_y=[0,1] are unit vectors. It is intuitive that changes in this position vector can be calculated by the tangent vector function of *v(t)*, which is:

$$\dot{v}(t) = \dot{x}(t)U_x + \dot{y}(t)U_y \tag{2.15}$$

the (2.15) implies that, if a point is moving along the curve in time t, then the tangent vector defines its instantaneous motion. The direction of the point at any instant can be calculated as:

$$\varphi(t) = \tan^{-1}(\dot{y}(t)/\dot{x}(t)) \tag{2.16}$$

The curvature at any point v(t) describes directional changes φ(t) with respect to changes in length of the arc of the given curve, that is:

$$K(\mathrm{t}) = \frac{\mathrm{d}\varphi(\mathrm{t})}{\mathrm{ds}} \tag{2.17}$$

Where, *s* is the length of the curve and φ is the angle of the tangent to the curve at point t. For every pixel along the edge, a gradient direction value can be obtained that represents the normal direction at that point. The tangent is represented by an orthogonal vector and curvature is given with respect to arc length, because a curve parameterized by arc length retains a constant speed of motion. The direction of the tangent vector change at point *v(t)* can be calculated using (2.17):

$$K(\mathrm{t}) = \frac{\dot{\mathrm{x}}(\mathrm{t})-\dot{\mathrm{y}}(\mathrm{t})\ddot{\mathrm{x}}(\mathrm{t})}{[\dot{\mathrm{x}}^2(\mathrm{t})+\dot{\mathrm{y}}^2(\mathrm{t})]^{3/2}} \tag{2.18}$$

There exists a very clear relationship between the derivative of a tangential vector and the normal vector. This can be deduced as follows. The tangential vector can be represented in polar form as follows:

$$\ddot{\mathrm{v}}(\mathrm{t}) = |\dot{\mathrm{v}}(\mathrm{t})|(\cos(\varphi(\mathrm{t})) + \mathrm{j}\sin(\varphi(\mathrm{t}))) \tag{2.19}$$

$|\dot{v}(t)|$ is a constant if the curve is parametrised by s. The parametric form of the curve can be represented by the parameter t (not necessarily the arc length parameter), which has two single-value functions: *x=X (t)* and *y =Y(r)*. Since the formula to compute the curvature involves first- and second-order derivatives, it can be expressed as a tangent vector:

$$\ddot{\mathrm{v}}(\mathrm{t}) = \mathrm{K}(\mathrm{t})\,\mathrm{n}(\mathrm{t}) \tag{2.20}$$

where, the derivative of a normal vector is given as:

$$\dot{n}(t) = -K(t)\dot{v}(t) \tag{2.21}$$

It is obvious that *n(t)* is normal to $\dot{v}(t)$. Hence, for each point in the curve, there exists a pair of orthogonal vectors $\dot{v}(t)$ and *n(t)* whose moduli are proportionally related by the curvature. This analysis provides a handy tool for evaluation detected edges. Clearly, for a straight edge, the second-order derivatives *ẍ(t)* and *ÿ(t)* are almost zero; hence the curvature function is zero. However, for a curve with radius r:

$$\dot{x}(t) = r\cos(t) \text{ and } \dot{y}(t) = -r\sin(t) \tag{2.22}$$

$$\ddot{y}(t) = -r\cos, \ddot{x}(t) = -r\sin(t) \text{ and } K(t) = 1/r \tag{2.23}$$

Curvature is used to detect low-level features where the image surface bends sharply; these features are computed then defined as maximum curvature points on the image. This technique can be applied to discrete data such as edges consisting of pixels where it can clearly indicate the amount of bending at each point along a path and ascertain whether lines bend very sharply with high curvature (r) or (0) curvature, as in the case of straight lines.

2.4.9 Affine Length Parametrization

The affine approach is based on the distance between an invariant set of Legendre descriptors of the target and reference shapes[57].

The affine-length τ between two points P_1 and P_2 is:

$$\tau = \int_{P_1}^{P_2} \left(\dot{x}(t)\ddot{y}(t)\right) - \left(\ddot{x}(t)\dot{y}(t)\right)^{1/3} \quad dt \tag{2.24}$$

Which, is absolutely invariant to rotation, however, it relatively invariant to scale change [57], and to affine transformations. Calculating affine length

parameterization involves up to third order derivatives of x(t) and y(t) [57] using (2.17) and (2.24). The numerator of (1), which incurs higher order derivatives, equals to one in the case of affine-length parameterization as now by differentiating x(τ) and y(τ):

$$\dot{x}(\tau) = \frac{\dot{x}(t)}{(\dot{x}(t)\ddot{y}(t)) - (\ddot{x}(t)\dot{y}(t))^{1/3}}, \dot{y}(\tau) = \frac{\dot{y}(t)}{(\dot{x}(t)\ddot{y}(t)) - (\ddot{x}(t)\dot{y}(t))^{1/3}} \tag{2.25}$$

Again by differentiating $\dot{x}(\tau)$ and $\dot{y}(\tau)$ we have:

$$\ddot{x}(\tau) = \frac{3\ddot{x}(t)(\dot{x}(t)\ddot{y}(t) - \ddot{x}(t)\dot{y}(t) - \dot{x}(t)\dddot{y}(t) - \dddot{x}(t)\dot{y}(t))}{3(\dot{x}(t)\ddot{y}(t)) - (\ddot{x}(t)\dot{y}(t))^{5/3}}$$

$$\ddot{y}(\tau) = \frac{3\ddot{y}(t)(\dot{x}(t)\ddot{y}(t) - \ddot{x}(t)\dot{y}(t) - \dot{y}(t)\dddot{y}(t) - \dddot{x}(t)\dot{y}(t))}{3(\dot{x}(t)\ddot{y}(t)) - (\ddot{x}(t)\dot{y}(t))^{5/3}} \tag{2.26}$$

Where, $\dddot{x}(\tau)$ *and* $\dddot{y}(\tau)$ are third order derivatives. From (2.23) and (2.24)

$$\dot{x}(\tau)\ddot{y}(\tau) - \ddot{x}(\tau)\dot{y}(\tau) = 1$$

Therefore, the curvature on the affine-length parameterized curve is given by according to (2.17) as:

$$K(\tau, \sigma) = \frac{1}{[\dot{x}^2(\tau, \sigma) + \dot{y}^2(\tau, \sigma)]^{3/2}} \tag{2.27}$$

Where, according to the property of the Gaussian convolution

$$\dot{X}(\tau, \sigma) = x(\tau) * \dot{g}(\tau, \sigma) \text{ and } \dot{Y}(\tau, \sigma) = y(\tau) * \dot{g}(\tau, \sigma) \tag{2.28}$$

The planar curves are parameterized using affine-length. This can be exploited to extract corners with the same computational cost as the arc-length parameterized curvature [56].

2.4.10 Harris Corner Detection Algorithm

The Harris corner detection algorithm is performed by calculating each pixel's gradient. Basically, the algorithm tells us whether the absolute gradient values in two directions are both great, in which case the pixel assumed to be a corner. The following equation is applied to determine if a point is a corner [58]:

$$R = \det(M) - ktr^2\,(M) \tag{2.29}$$

where M is the evaluated matrix of gradient, ktr^2 is the trace, det is determinants and R is response; R is positive for corners, negative for edges and small for flat regions (constant intensity). Suppose M is defined as follows:

$$M(x,y) = \begin{bmatrix} I_u^2(x,y) & I_{uv}(x,y) \\ I_{uv}(x,y) & I_v^2(x,y) \end{bmatrix} \tag{2.30}$$

$$\begin{aligned} I_u^2(x,y) &= X^2 \oplus h(x,y), \\ I_v^2(x,y) &= Y^2 \oplus h(x,y), \\ I_{uv}(x,y) &= XY \oplus h(x,y), \end{aligned} \tag{2.31}$$

$$h(x,y) = \frac{1}{2\pi}\, e^{-\frac{x^2+y^2}{2}} \tag{2.32}$$

where, in (2.31), *Iu(x,y)* and *Iv(x,y)* are the partial derivatives of the values in direction u and *v* at point *(x,y)*. If *f(x,y)* is the second-order mixed partial derivative. The Gaussian filter (2.32) is *h(x,y)*, where *X* and *Y* are the first-order directional

differentials, which are calculated by convolving the grey values and their variance in directions u and v. The Gaussian filter is applied to reduce noise, because first-order directional differentials are sensitive to noise. A Gaussian filter is a typical 2D linear filter that is widely used to de-noise images. The goal of using this 2D filter is to reduce high-frequency noise in an image while retaining the important image features, like edges and details, as much as possible. The linear filter convolves the image with a constant matrix to obtain a linear combination of neighborhood values, which are used to eliminate the noise in the presence of additive noise. However, this can create blurred and smoothed images.

2.5. Conclusion

This chapter has provided the reader with a medical and conceptual background of total hip replacement and its complications. It also summarizes state of art and most common approaches used for the interpretation of THR complications based on medical assessments, supported by image processing and by other technological means. Existing approaches to automated computer assisted analysis of some of the complications were also reviewed. Further related theoretical background behind fundamental computer vision and image processing algorithms were provided as this knowledge is essential in building novel, fully automated systems approaches to THR image analysis.

From the literature review, it is obvious that there is a critical need of well-informed analysis and interpretation of THR complications leading to accurate and timely clinical diagnosis by medical experts. However the tools that exist do not cover the detection of all types of faults and the approaches proposed to date requires automation. In Chapters 3-6 we proposes novel, fully automated approaches to prosthesis detection and detection of subsidence, loosency and infections.

Chapter 3.

Automatic Prosthesis Extraction and Key Point localization

3.1 Introduction

Radiography is the standard imaging modality used for evaluating THR complications. The challenges of segmentation of objects of interest in such a modality are often associated with low contrast, presence of noise and other artefacts. In contrast to the use of some generic segmentation methods the use prior knowledge the structure of an object of interest, such shape models, relative orientation or texture, can often be effectively utilised. Providing an automatic and accurate image processing solution that extracts a prosthesis from within a THR radiograph is of a realistic significance towards designing and implementing a computer aided system that aims to minimise the post-processing cost of detecting and recognizing complications in THR surgery.

During the initial stages of the proposed research image histogram thresholding was adopted as an image segmentation technique to extract the prosthesis of a THR image. The associated x-ray images were binarised as foreground objects and background where the prosthesis only was made clearly visible in order to enable subsequent detailed analysis of the associated THR image. However this work revealed the difficulty of using a fully automated approach to determine the optimal threshold value given the variabilities of image contrast and clarity often present in THR images (see Section 3.2). Thus, there was a need for an

adaptation of a more efficient approach where the image processing to be carried out is automatic and the results obtainable are more prominent. Therefore as a solution to the abovementioned challenge in using histogram thresholding, subsequently the use of active contour approaches to automatically extract the prosthesis was investigated. Due to its demonstrable success, its use in extracting the obturator foramina was subsequently investigated as a successful outcome can be used as a pre-processing approach to support the detection of misalignment in THR surgery [13].

This chapter is primarily focused on introducing effective segmentation techniques for the extraction of the prosthesis and the obturator foramina that can lead to the capability to carry out more effective further processing of THR images aimed at automatically detecting surgical complications such loosening, subsidence and infection. For clarity of presentation the chapter is divided into three main sections introducing three segmentation methods including the result of each adopted appraoch: section 3.2 describes the extraction of prosthesis using histogram thresholding, section 3.3 demonstrates the automatic extraction of prosthesis using the active contour method and finally section 3.4 presents an approach to the segmentation of obturator foramen using an active contour based approach.

3.2 Prosthesis Extraction Uing Histogram Thresholding

In medical imaging applications the separation of regions of interest in often a mandatory procedure as it enables subsequent image analysis that uses the prosthesis as a reference.

Histogram thresholding is one of the widely-used techniques in object segmentation. This method assumes that the images are composed of regions with

different intensity grey levels and each region corresponds to an object; where the intensity grey levels are similar or within a given range. An intenisty can separate an image into a number of regions represented by its peaks. The threshold value is selected as an intensity value within the valley between two adjacent peaks [36]. The approach generates two regions, the foreground that represent the brightest object/s (i.e. the prosthesis) and the background. This method was proposed by *Oprea et al. [15]* to segment the prosthesis stem components: prosthesis, bone (femur) and soft tissue regions from x-ray images and was then compared with other potential segmentation techniques. The extracted prosthesis was compared with the correct prosthesis component segmentation obtained by manual annotation. A further attempt on the same problem was made by *Florea et al. [16]*. Florea focused in the separation of bone and medullar channel that separate the bone from the prosthesis in order to determine the limits of both area. A histogram based segmentation method was used for segmenting the femoral parts and in order to achieve better results an expectation maximization (EM) algorithm and Canny Edge Operator were applied *[16]*. Moreover, a median filter was chosen to impose contour continuity. Both methods *[15,16]* concentrated on segmenting prosthesis components automatically into three parts considering that *Oprea et al. [15]* used original x-ray images before the execution of any segmentation techniques and *Florea et al. [16]* enhanced the quality of x-ray images by adjusting the luminance of pixels prior to reduce the noise.

At the initial stage of this work we adopted the method histogram thresholding to extract the prosthesis from the x-ray image so that it can be used as a reference in further image analysis to identify THR complications. Histogram thresholding applied on the original THR x-ray images manually. Before applying histogram thresholding the images first were cropped so the surrounded area of the prosthesis stem is clearly visible. By this we limit the quantity of available spatial information within the image and perofrm simple computational solution for

determining the ultimate threshold value. (Note: as this is not an ideal practical solution; in section 3.3 we propose a solution to this problem].

The histogram thresholding process divides the image into two regions representing the prosthesis and background. This method transform the input image, *f*, to a binary image, g, by clustering the pixels with similar intensities, i.e. pixels with higher pixel intensity than the threshold clustered into one class and the remaining pixels clustered into a second class. The threshold value (T) separates these two clusters into foreground and background and the value is chosen manually between two peaks of histogram [38]. The target background results are demonstrated in figure 3.1. The histogram of sampled image is graphed as taller line shows intensity distribution from 0 to 255 and returns an output of binary image. The default threshold values can be adjusted as required by clicking with mouse on intensity distribution line.

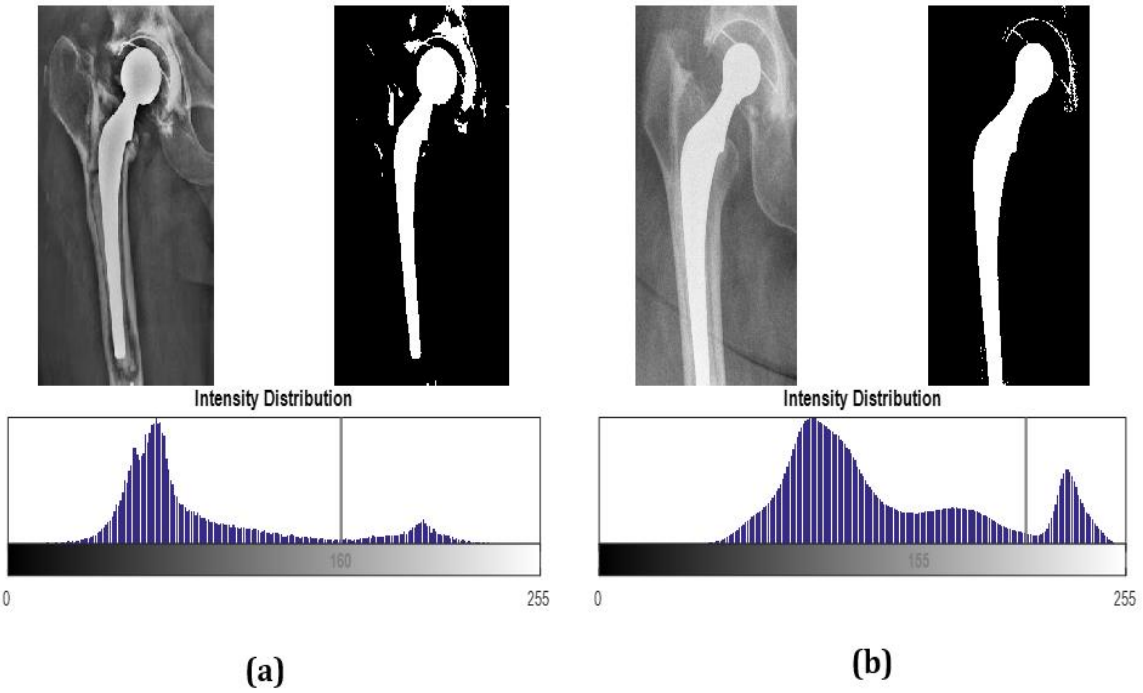

Figure 3. 1: Results of Histogram Thresholding in (a) & (b)

Although this method is simple and effective for segmentation, it is often difficult to set an optimal threshold value precisely for all the sampled x-ray images, especially, in such cases when the images imbued with noise or two peaks are equal in height. The threshold values in this experiment ranged from 145 to 200 upon appropriateness to the x-ray image. This might be considered as a weakness for the adopted method as we were looking for an automated solution. Additionally, the segmented prosthesis is attached with extra white unwanted pixels/regions. In order to have clear prosthesis boundary; we used flood fill method [59], as a filtering step performed on binary image that clear the borders of prosthesis and remove weak edges around it. This method estimates of a set of parameters that best fits the available data of the connected background pixels with (0's) and foreground (1's), stopping when it reaches prosthesis boundaries in the binary THR x-ray image. The results are shown in figure 3.2.

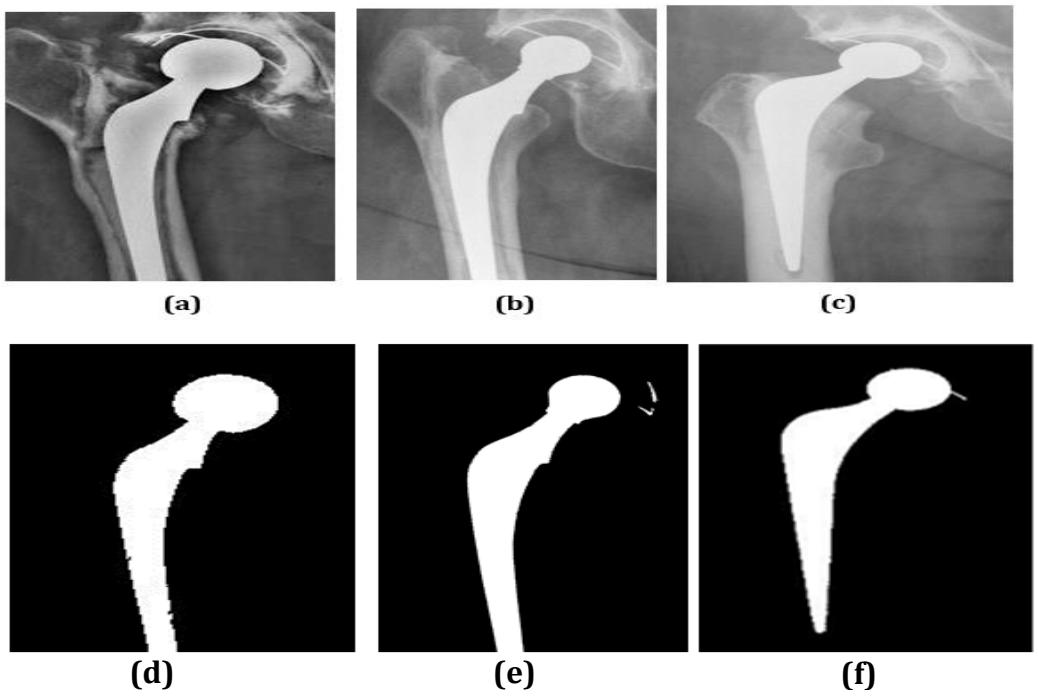

Figure 3.2: (a),(b) and (c) are segmented THR x-ray images and (d), (e) and (f) are corresponding threshold images that shows clear prosthesis boundaries after clarifying the edge

In addition, this method failed to find a proper threshold for complex (blurry) THR x-ray images as shown in figure 3.3.

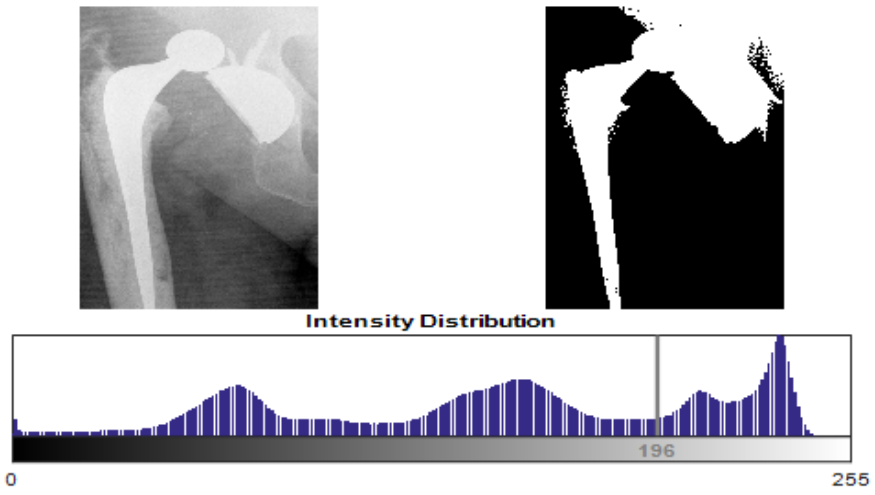

(a)

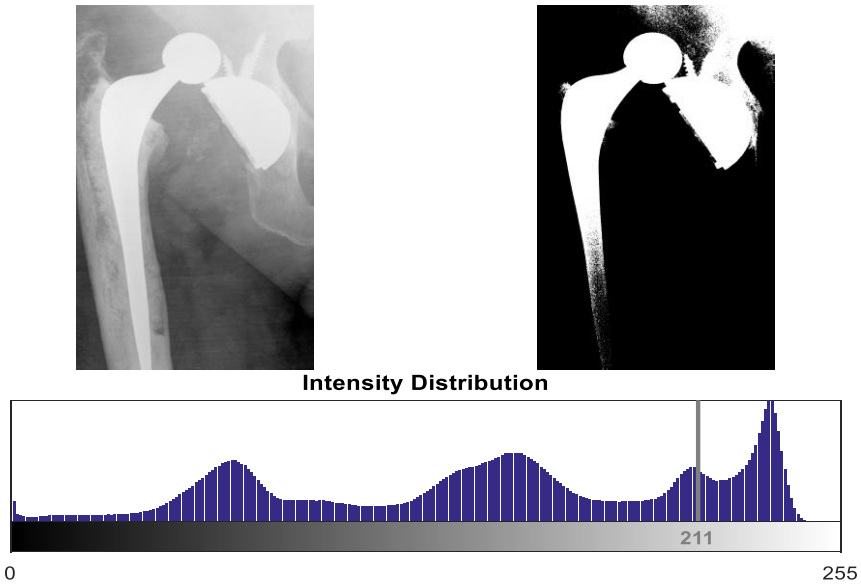

(b)

Figure 3.3: Example of Threshold selection; (a) shows the default threshold value (196) and (b) when we raised the threshold value to (211), broken edge appears

Figure 3.3, illustrates a segmented prosthesis having weak edges around it. As shown in figure 3.3(a), if the threshold value is set at 196 over-segmentation results and if it is raised to the value to 211, broken edges appear as can be seen in figure 3.3(b).

Histogram thresholding is a quite effective technique in segmenting the prosthesis without dividing the prosthesis into varouis component as *Oprea et al. [15]* and *Florea et al. [16]* applied. However, it does not provide an automated solution for prosthesis segmentation as well as it is not suitable to be used in extracting prostheses from THR x-ray images having weak edges. The presence of noise or weak image gradients and other artefacts deteriorate the performance resulting in either the approach failing to extract prostheses effectively or requiring pre-processing steps to obtain ideal results. Therefore, in the following section image processing techniques that fully automate prosthesis extraction and results in more accurate segmentation of prosthesis is sought.

3.3 Automatic Prosthesis Extraction Using Active Contour Method

One further possible image processing technique that has been used with regards to prostheses segmentation is template matching [60]. However, to define the boundary of a shape to be extracted using template matching; requires exact prior knowledge of that object. In THR imaging the prostheses to be extracted can be of a different shape depending of the manufacturer or the prostheses, choice of use and decisions made by the surgeons. Therefore this approach is considered to be less useful due to practical reasons.

To overcome possible difficulty caused by intensity inhomogeneity and possible concavity of boundaries in an object; active contour methods (snake) can be used to attain better segmentation accuracy as compared to the above mentioned and popularly used segmentation techniques in THR imaging. Active contours are a set of points that aims to extract the shape of an object. The points are expressed as energy minimization points that formulates under principal of functional energy. This energy function has the ability to evolve and capture curved objects based on image gradient information that identifies object boundaries. This approach is inspired from the work of [44],[54] & [63]. Although active contour approach is widely used in medical applications; no literature was found during the literature reviews conducted within the research context of this thesis that proposed the use of extracting the implant prostheses from THR x-ray images automatically. Therefore in the following sections our attempt to use a snake based approach [44] for automatic prosthesis extraction is presented.

3.3.1 Proposed Approach

For extracting the prosthesis automatically; it is proposed to use the active contour method as illustrated by the block diagram in figure 3.4:

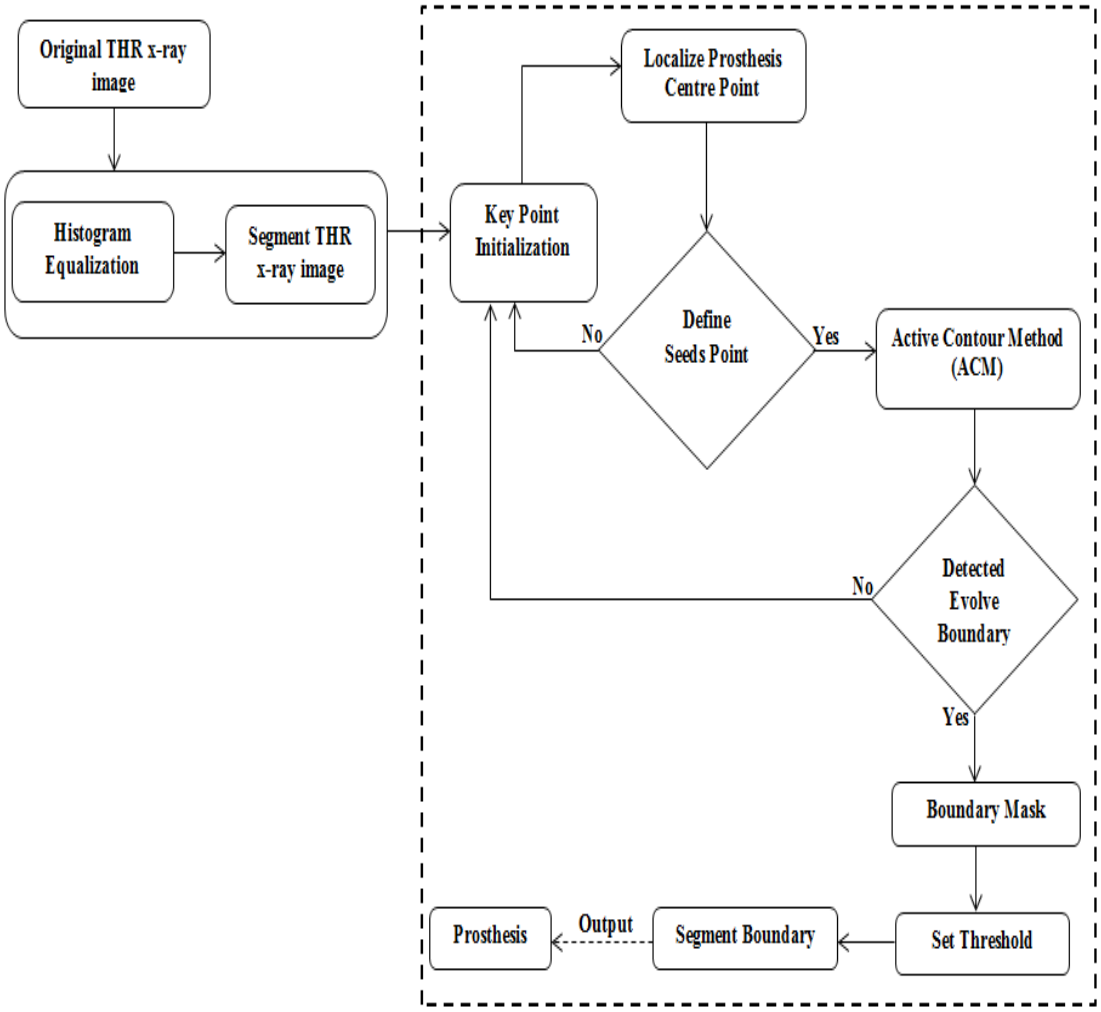

Figure 3. 4: Diagram of Prosthesis Extraction from THR X-ray Images

To ensure that the ACM operates similarly on various THR x-ray images; histogram equalization [70] was initially applied to normalize the x-ray images, so that the edges become more evident. Enhancing the edges is necessary as the aim is to segment the prosthesis from the entire THR x-ray images automatically, for less computational cost and accurately capturing the target in the region of interest.

The Active Contour Method requires the selection of a seed point from within the prosthesis to start the process of clarifying the pixels belonging to the

prosthesis automatically. To locate the seed point, we consider the prosthesis cup as a circular shape which has a centre point as **C** within a given radius **r**, so the location of **C** as **(h, k)** in the image can be determined using subsequent predefined measurements of height as **h** and width as **w** (where **h > w);** we crop the image to include the prosthesis as in figure 3.5.

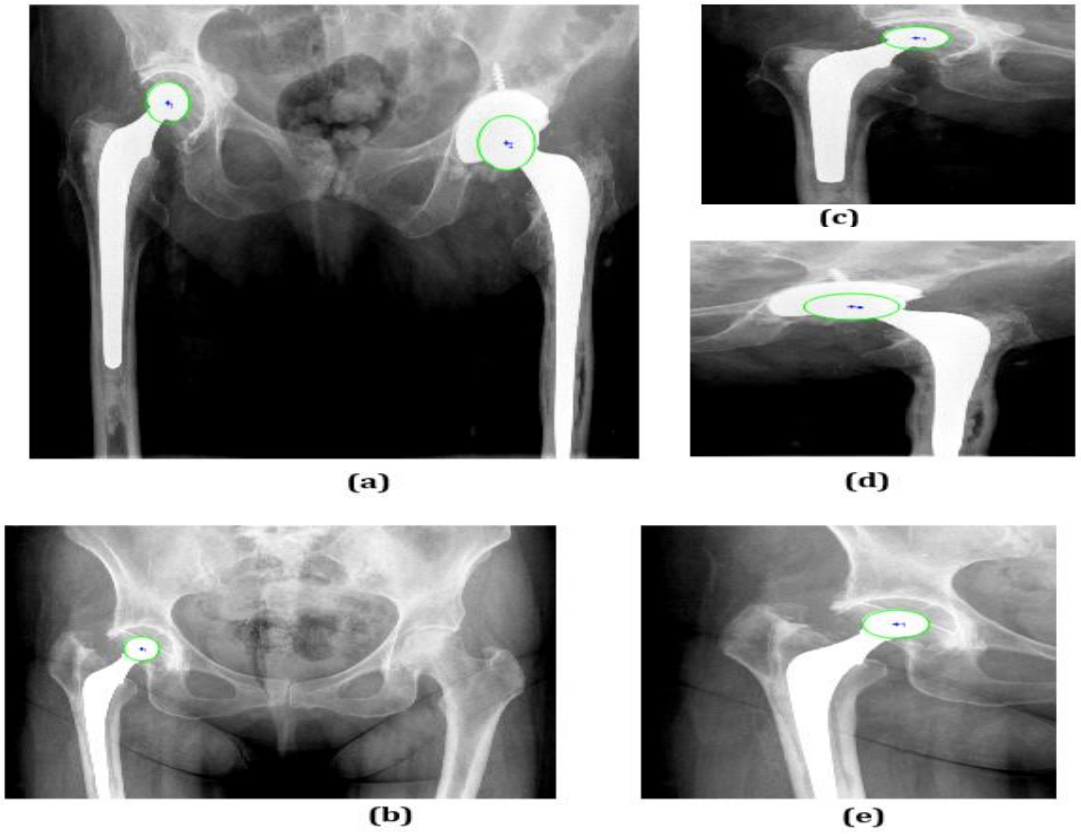

Figure 3.5: (a) and (b)sample THR x-ray images and corresponding segmented images are (c) ,(d) and (e) respectivly

This solved the problem of the segmenting the required region from the entire THR x-ray image. More details of centre point detection approach is explained in subsection 3.3.2.

3.3.2 Key Point Initialization

A requirement of automatic extraction of the prosthesis shape using an active contour method is that the initial contour has to be placed near the prosthesis boundary in an image inorder to limit the capturing range within the prosthesis edge. The prosthesis cup is circular in shape; so we used a fast randomized circle detection algorithm [61] to determine the center and the radius of the prosthesis cup. This algorithm is widly used to detect location of circulaur objects in an image. The principle of fast randomized circle detection is depend on gradient vector of an edge pixel points at the center of the circle. A line is defined, which is coincident with the gradient vector of the edge pixel in which pixels are passesing through. The gradient lines of all the edge pixels are lying on the edge of a circle that intersect at the center of the circle. The radius of the circle is determined by computing the distances between the edge pixels and the center [61]. Subsequently, those point were used in deriving a key/seed point of the active contour approach as seen in figure 3.6.

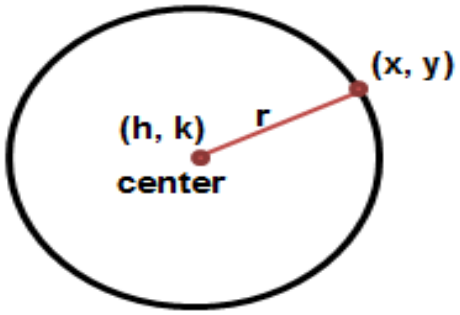

Figure 3.6: Center point of circle and radius

Suppose pixle of an image is represented as f(x,y). We compute gradients of f(x,y) by applying the Guassain smoothing filter. Then we create an edge map using Sobel edge detector [62] to define the pixels that belongs to edges of the image. The

edge pixels are grouped into segment according to their connectivity with their neighbour using connected component approach. We used 8-adjacent connected pixel that construct the edge curve set of V, and No_v indicates number of pixels in V. By assuming that Nov indicates the number of pixels in V , if No_v >T, where T is threshold to determine whether a point belong to the curve as it set 0.5 and 0.6. Then each point of the curve is picked up by the homogeneous distribution and gradient line of the point is computed. The point through which the most lines passed is yielded as the intersection point, i.e. as C, as we assumed it as the centre of the potentially circular shape. The accumulation of point C is indicated as Cnum. If $C_{num} > T_{num}$, the point C is then indicated as a center of a circle. We compute the radious by averging the distance between C and the edge point. The result of the proposed approach illustrated in figure 3.7, the circular cup region of the prosthesis is clearly detected on the sampled THR x-ray images.

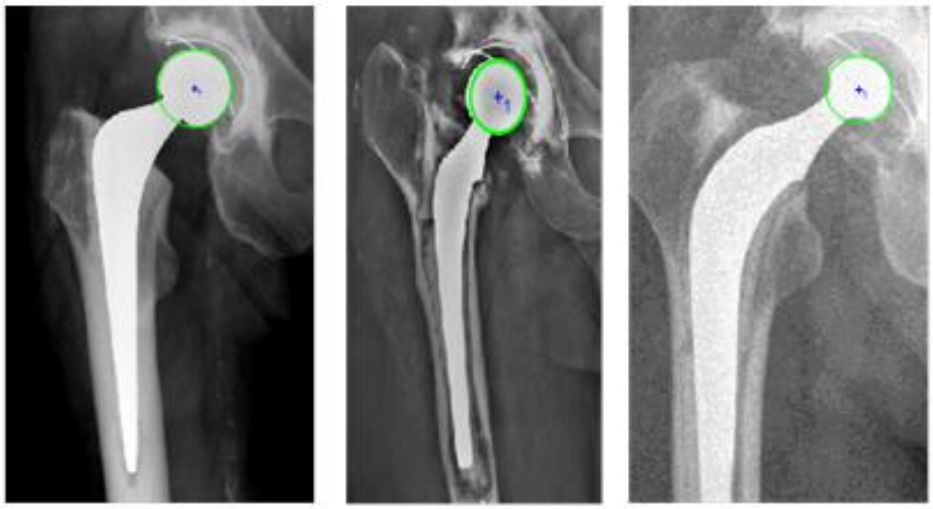

Figure 3. 7: Detected circular cup region of the prosthesis

After locating the centre **C** and radius **r** of the prosthesis cup, we can define seeds point of the active contour method. As we know that all the points on the circle

must be within distance of **r** from **C** (**x, y)**, we can find all the point on such as **(x, y)** using either of the following coordinates:

For the right most point: ***(x+r, y),*** (3.1)

For the left most point: ***(x-r, y),*** (3.2)

For the top most point: ***(x, y+r),*** (3.3)

For the bottom most point: ***(x, y-r),*** (3.4)

Since the x-coordinate is added to r to get the most right point and y-coordinate is added to get the top most point. The same is performed for the left most point and bottom most point. In our experiment we used the right most point as the seed point for the ACM to avoid detection of any weak edges. Also this point lies within the cup of the prosthesis that is closest to the boundary. More details about seeds point in the next section.

3.3.3 Active Contour Method

Our interest is to separate the prosthesis from the surrounded region in x-ray image automatically. A robust and accurate deformable snake based segmentation approach is used. The approach starts with a predefined set of seeds point as described in subsection 3.3.1. These points include the initial contour parts of the interested object which is the cup of the prosthesis. It starts deforming from these seeds by appending nearby nonzero pixel points based on an energy minimization method. If a line is parametrized through a variable **v** that goes from 0 to 1, then two functions of this variable define the coordinates of the snake point along the line which are v(x) and v(y). It can be defined as a vector $\underline{v}$= (x (v), y (v)). Since snakes are often implemented as closed contours it enforces setting $\underline{v}$ (0) =$\underline{v}$ (1). The energy function that is used to define as:

$$E = \int_0^1 (E_{int.}(v(s)) + E_{ext.}(v(s))) \quad (3.5)$$

$Ei_{nt.}$ is an internal energy defined within the curve (or line), designed to keep the snake curve smooth during deformation process while $E_{ext.}$ is an external energy defined by image properties such image gradient, it moves the snake curve toward the edge of an object as the inverse of image gradient magnitude represents low energies at the edges and higher energies elsewhere on the image. Due to this property the snake is pushed into a directional attraction within the boundary concavities. However, the property of energy function is controlled by set of predefined parameters , β and α to have an appropriate convergence condition on the images. Those points are isolated and guided by a Partial Derivative Equation (PDE) [64] where it causes the energy forces to be defined in such a way as to provide a sufficiently large range for the forces to evolve the relevant structure of the prosthesis boundary. The PDE runs in an iteration scheme of energy forces for each point as in figure 3.8 (a) and (b), that is then incorporated into a level set formulation with a level set regularization term, for more details see [65]. The level set preserves stability of accurate computation to properly evolve the contour in order to fit the boundary as without it the contour becomes much slower and can even stop before it reaches the desired object boundary. In case if the desired boundary is not evolved properly then the initialization key point is reset.

3.3.4 Prosthesis Extraction

Although ACM display an intermediate output of a closed contour of the prosthesis, the final segmentation results have nothing much to do with the initial contour initialization, since the active contour method is contingent on level set in developing the contour. The level set maintains [65] a real mask of initial state of the active contour. Therefore, once the iteration stops, a mask is generated of the

same size as the input image, where the object or ROI is highlighted. The final contour extraction is performed by a threshold to distinguish the prosthesis from the background as a binary image where the object boundary is white (logical true) and the background is black (logical false). The extracted binary image gives us a better approximated shape of prosthesis as a closed contour. The extracted prosthesis boundary and featured points on this boundary plays an important role as reference points in the research that will be presented in chapters 4-6.

3.3.5 Results of Application of ACM to Automatic Prosthesis Extraction

This approach deforms an initial curve based that is based on seed points that are defined via a circle detection of the prosthesis cup in THR x-ray images. It continuous to converge toward the edge of prosthesis with fixed parameters with energy forces are at their minimum. For consistency in this experiment, the influential parameters for all sampled images are kept constant. The weights of smoothing the contour are set to: $\lambda=1$, $\beta = 0.2$ and $\alpha = 2$. In addition, we tuned the adopted method of ACM in an attempt to capture the prosthesis at a radius of $\boldsymbol{r} = 45$ in pixels, based on prior knowledge of the image sizes we processed. This method successfully outlines the desired boundary with high accuracy as seen in figure 3.8, figure 3.9 and figure 3.10. In the illustrated figures, we show the initialization of the seeds point first and then the deformation process till it converge the prosthesis boundary completely with 2100 iteration.

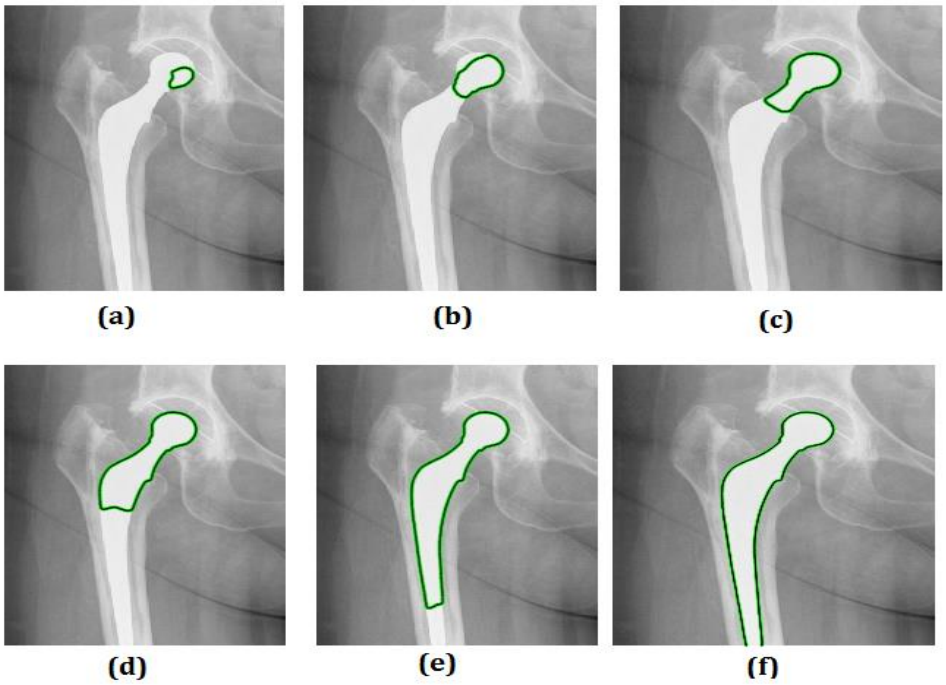

Figure 3. 8: An Illustration of Active Contour Method deformation process

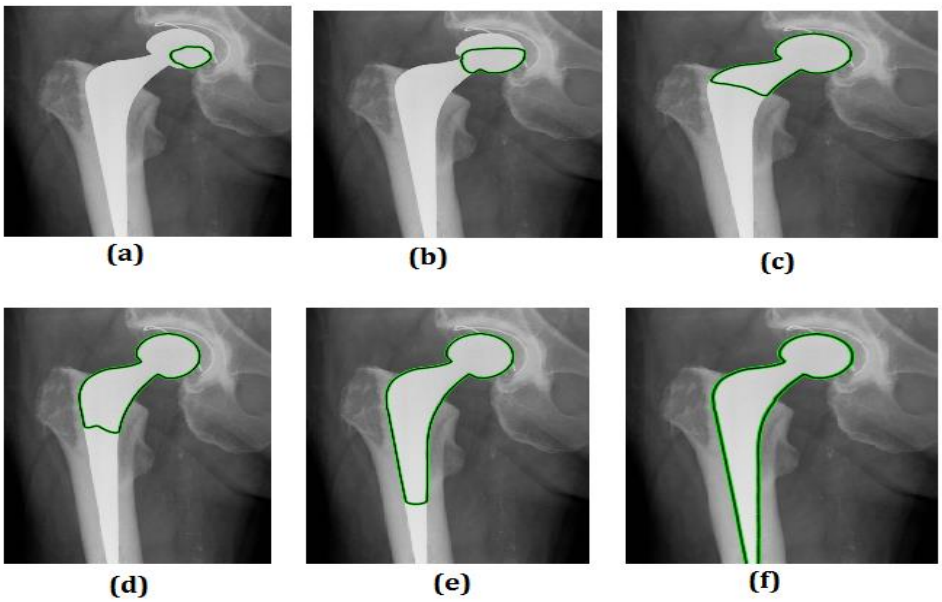

Figure 3. 9: Another example of Active Contour Method deformation process

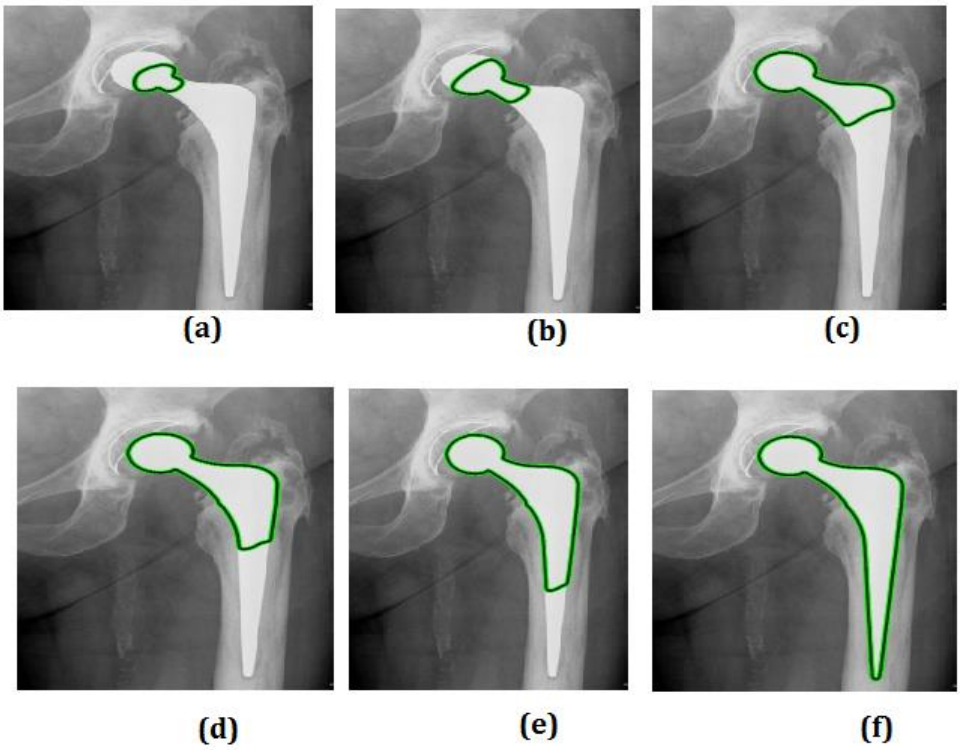

Figure 3. 10: Another example of Active Contour Method deformation process

As can be noted by the above results the curve starts to first converge to the rightmost point of the prosthesis cup (as the seed point was selected to be closest to the rightmost edge of the prosthesis as described in section 3.3.2) and subsequently converge towards the prosthesis boundary after number of iteration. As implanted prostheses are not the same in shape in all experimented THR x-ray images and to ensure the proposed method evolve the anticipated shape of prosthesis; the iteration were set to 2500. It takes on average up to t=0.76 seconds to complete the converging process to the prosthesis boundary with the original THR x-ray images resized by a factor of 0.5. The prosthesis extraction was tested on 35 THR x-ray images and the ACM execution was set to terminate once the iteration process is completed. The results indicated that the approach outlines the prosthesis boundary accurately and generates segmented binary masked images as illustrated in figure 3.11.

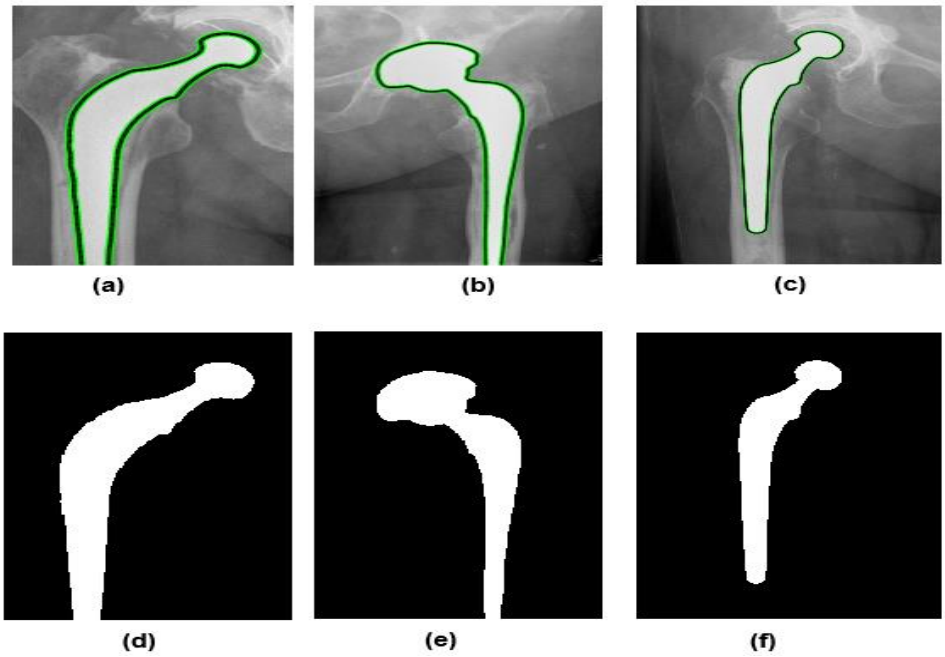

Figure 3.11: Final ACM prosthsis segmentation results in (d),(e)&(f) of image (a),(b) &(c)

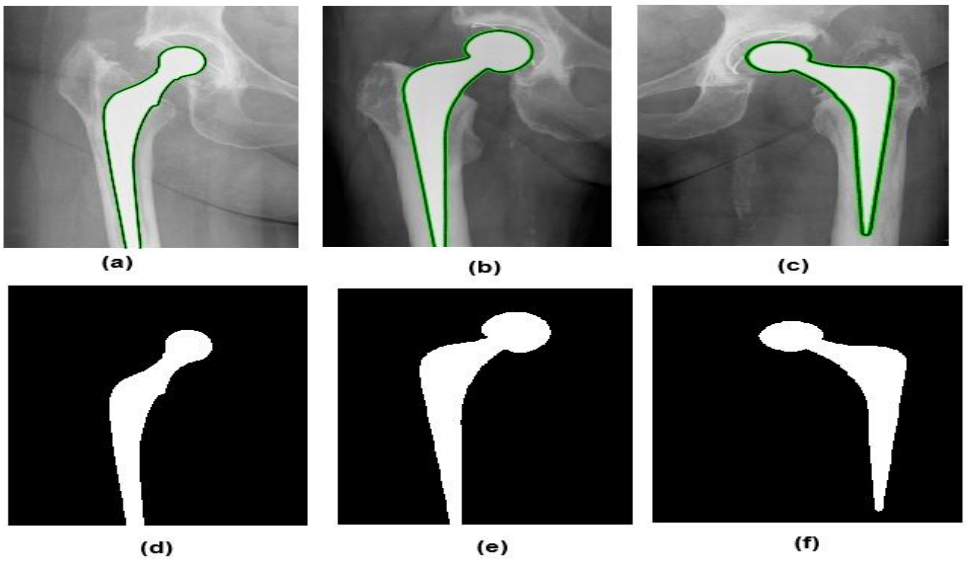

Figure 3.12:More results of final ACM prosthesis segmentation in (d), (e) & (f) of image (a),(b) &(c)

Figure 3.12, illustrate the generated binary masked images of the prosthesis extracted via ACM of figure 3.8, figure 3.9 and figure 3.10 respectively. The extracted prosthesis.

A further experiment is performed to demonstrate the effect of choosing different ACM parameters in capturing the prosthesis boundaries in particular from images containing extreme amounts of background details and clutter. The converging boundary range and the convergence speed when extracting different implanted prosthesis was analysed. Results showed that with the careful selection on ACM parameters, it is possible to extract the prosthesis even from blurry and complex THR x-ray images as seen in figure 3.13 (a), (b) and (c). The prosthesis conuntor is clearly extracted.

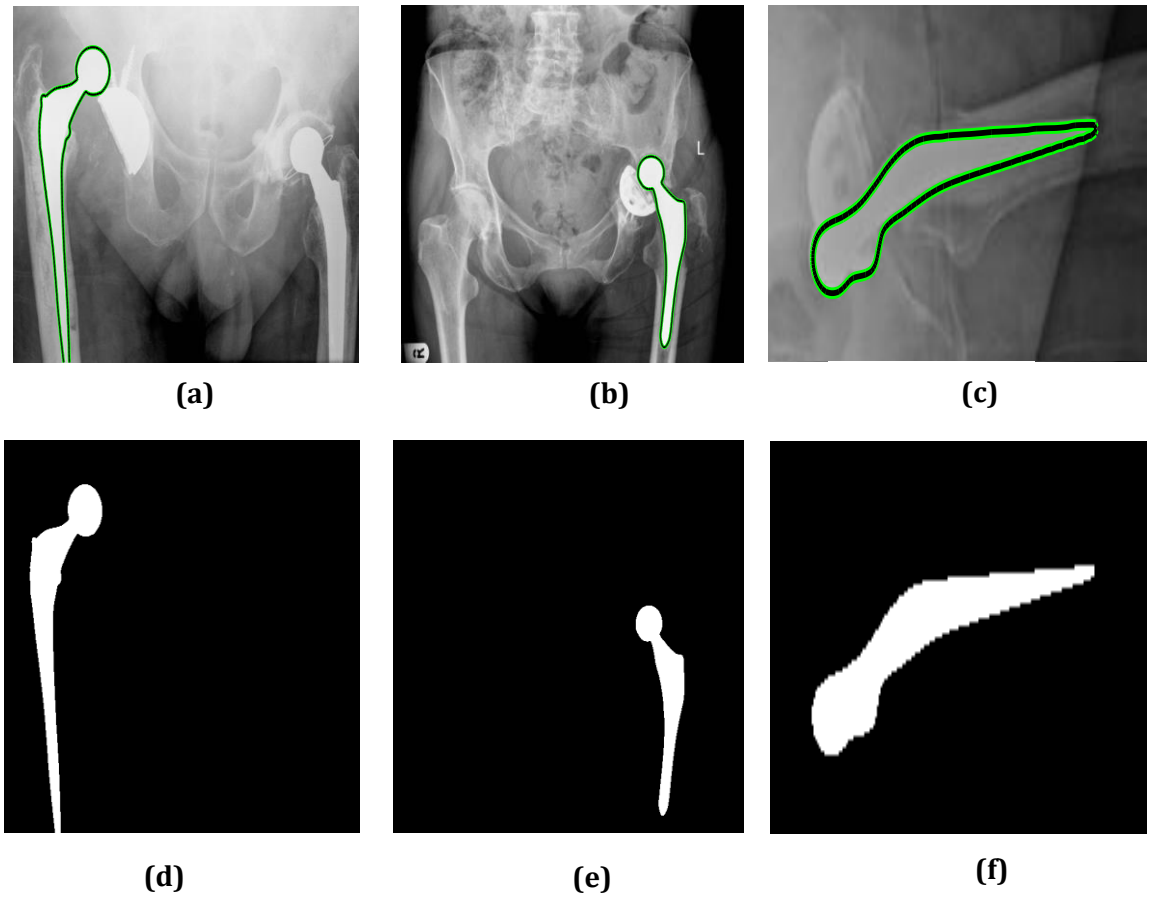

Figure 3. 13: ACM results of blurry and complex THR x-ray images in (a),(b) &(c) crrosponds final prosthsis segemtation in (d),(e) &(f)

Conversely, the extraction processes were much slower than the extraction of prostheses from segmented THR x-ray images; it took up to t=.97 seconds with

same iteration number for images (a) and (b) of figure 3.13. Thus we recommend that the prosthesis region is pre-extracted from a whole THR x-ray image before ACM is used for the extraction of prosthesis and boundary detection. Henceforth, we adopt this approach as a base of the coming chapters.

3.4 Segmentation of Obturator Foramen

According to the clinical background presented in subsection 2.2.2.4, the obturator foramen plays an essential role as a reference to measure misalignment or leg discrepancy after total hip replacement. The outline of bone structure of the obturator foramen is more visible and circular than the alternative, the ischia spine which is often obscured. Referring back to the literature review in subsection 2.3.1, either obturator foramen or ischia spine can be used to define misalignment or leg discrepancy. ACM is also applied to detect obturature foramen in THR x-ray images automatically. We increase the capture range so that the initialization seeds points are close to the boundary of obturator foramen. This was done by adjusting the parameters of the key point location of circle detection. However, it failed to detect the hole of obturator foramen. This is due to homogeneous regions within obturator foramen, besides the noise and poor contrast of x-ray images. Thus, we manually selected predefined initialization seed points close to obturator foramen at the inner edge of obturator foramen. Prior applying ACM, we enhanced the contrast of THR x-ray images, so the edges are more prominent. We used adaptive histogram equalization specified by the 'Distribution' parameter of 0.05. The method is able to iteratively fine tune the initial contour toward the final boundary detection. It extracts obturator from the other parts of the pelvic bone in THR image as can be seen in figure 3.14.

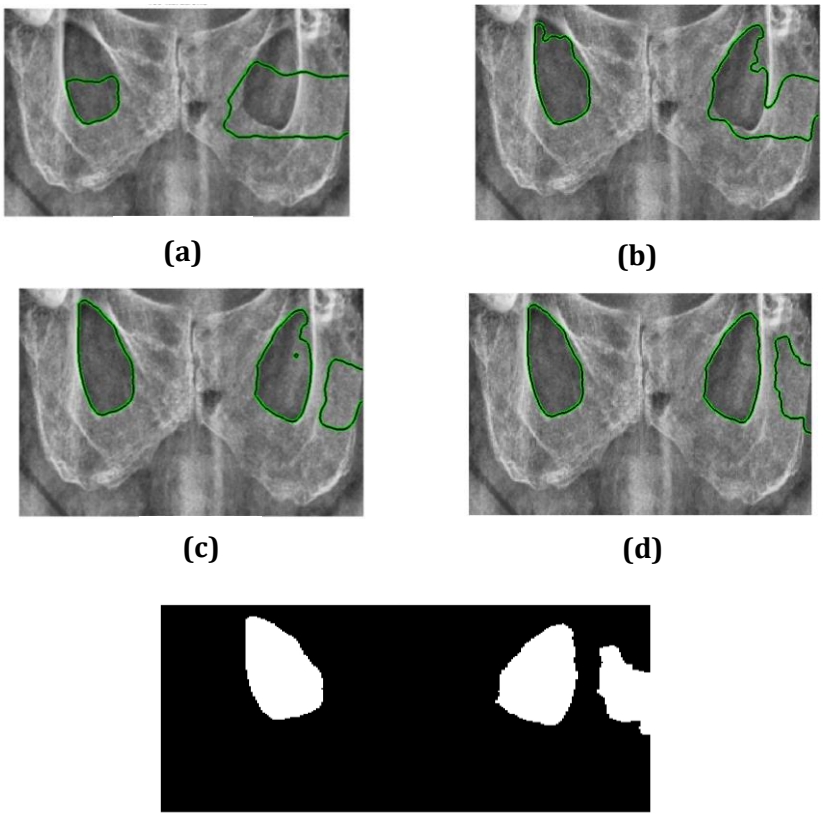

Figure 3. 14: Segmentation of obturator foramen using ACM
(a) Initial curve , (b) &(c) curve deformation , (d) final results of ACM and (e) segmentation results

In figure 3.14, we demonstrate the deformation process of ACM. As can be seen the obturator foramen is perfectly extracted. The influential smoothing parameter are set as $\lambda=1$, $\beta = 0.2$ and $\alpha = 0.2$. More results of obturator foramen segmentation are in figure 3.15.

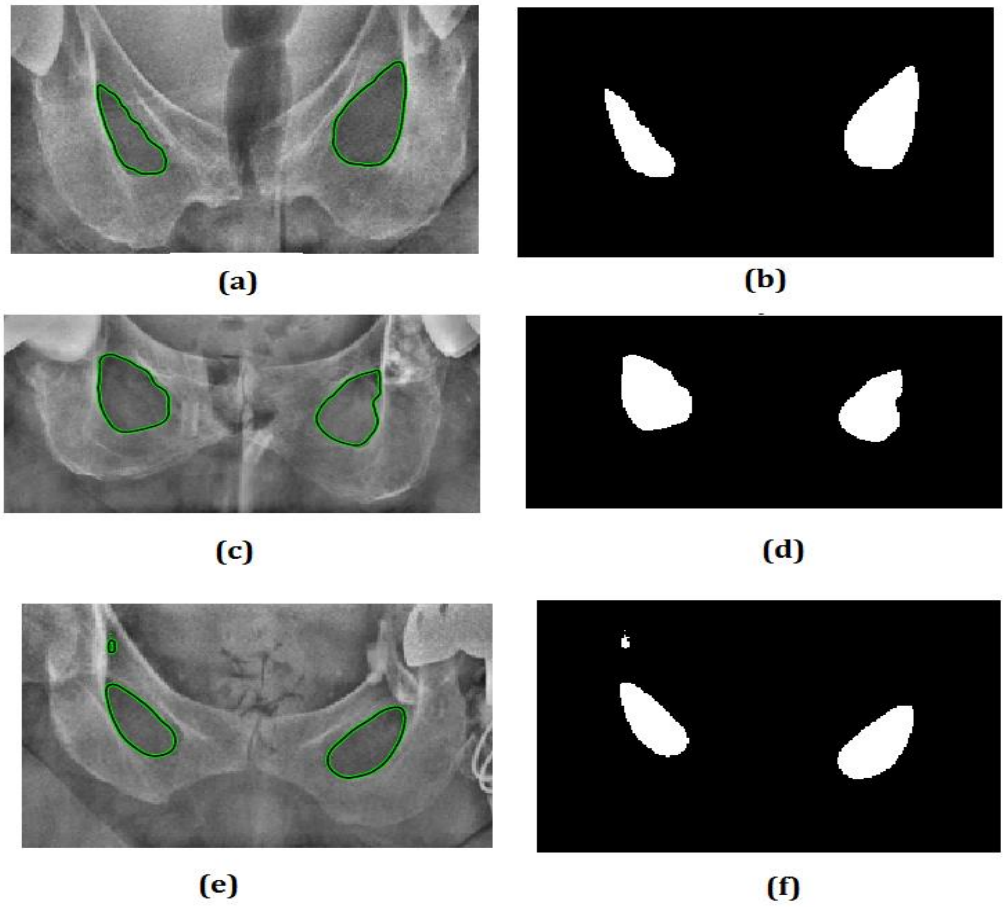

Figure 3.15: Segmentation of obturator foramen using ACM in (a) , (c) &(e) and final results in (b),(d), (f)

However, the ACM detects spurious regions/edge in some of the test images as illustrated in figure 3.15 in (e). This is due to homogeneous distribution of grey level intensity that has similar contrast in other regions. Such segmentation results can be can be improved by removing the extra detected object by applying further image processing techniques, such as ignoring small regions and ignoring regions which do not have a twin like object mirrored elsewhere on the image. In addition, some intermediate results of the contour evolution require different numbers of iterations; e.g., the number of iterations varied from 800 to 1200 base on the x-ray image quality. We also experiment the algorithm on various THR x-ray image as in

figure 3.16, however, the convergence time was longer when compared the convergence time of a partially segmented image.

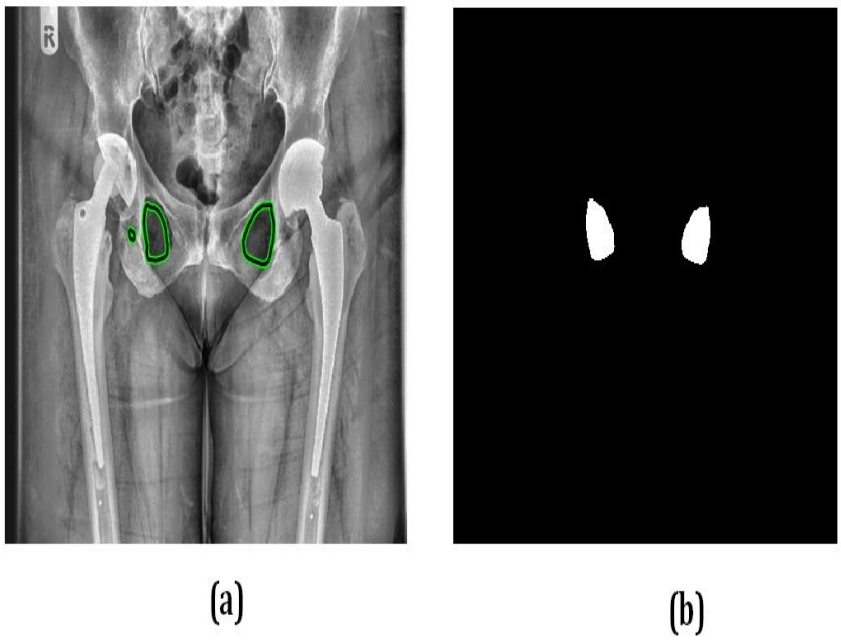

Figure 3.16: Segmentation of obturator foramen using ACM, (a) enhanced image and (b) Segmentation result as binary image

A recent study of [20] presents segmentation of obturator foramen using marker-controlled watershed segmentation and zernike moments. However, they applied marker-controlled watershed on region of interest that is drawn by hand to create a template obturator foramen. Our experimental results demonstrate effectiveness of active contour method in segmenting obturator foramen semi-automatically. This can be readily used as a template for further applications such defining misalignment after total hip replacement.

3.5 Conclusion

The aim of this work is to develop an accurate and efficient delineation tool for prosthesis detection in THR x-ray images. Often noise and low contrast undermines the automatic outlining of the prosthesis in THR x-ray images using the histogram thresholding. To overcome this difficulty; the active contour method were utilised in this chapter which automatically segment the prosthesis boundary from THR x-ray images accuratley. In addition, we implement the active contour method for the extraction of the obturator foramina in THR x-ray images. It perfectly segments the obturator foramina which can provide key points for the clinical identification of leg discrepancy / misalignment.

Having extracted the prosthesis it is now possible to identify certain featured points on the boundary of a prosthesis that can be used as reference/key points for the detection and analysis of THR complications (see Chapters 4, 5 and 6) as will be experimented and evaluated.

Chapter 4.

Detection of Prosthetic Loosening in THR Images

4. 1 Introduction

In this chapter a novel approach to automatic identification of prosthetic loosening in THR x-ray images is proposed. The proposed approach first measures the curvature along the boundary of the prosthesis to identify key points on the boundary around which loosening is likely to happen. By inspecting the pixel value gradients across the boundary of the prosthesis at these points and points surrounding these points that lie of the boundary of the prosthesis, it is shown that loosening can be identified if it exists.

For clarity of presentation this chapter is divided into several subsections. Apart from this section which provides an overview to the work to be presented in this chapter, section 4.2, introduces the proposed approach to identifying loosening in THR x-ray images. Section 4.3, summarises the prosthesis extraction approach presented in chapter-3 as it is used as a pre-processing step to identify the prosthesis boundary pixels followed by a description of generating and tracing the prosthesis edge map in section 4.4. Section 4.5, presents calculation of curvature at each of the prosthesis boundary points which is used to identify points of interest in a typical prosthesis boundary. Section 4.6, presents calculation of pixel value gradients across the prosthesis boundary, at the key points and those points on the prosthesis that surrounds them. Subsequently the results are presented in section 4.7. Finally, the chapter ends with a conclusion in section 4.8.

4. 2 Proposed Approach of Defining Loosening

Loosening can be identified from the boundary around the inserted steel 'prosthesis'. As stated in subsection 2.2.2.1, loosening refers to a condition which results in a radiolucent line/narrow region to be clearly visible just outside the implanted cemented prosthesis where loosening may have happened. For example, in figure 2.3, this line is visible around implant's femoral stem. A close inspection of THR images where the presence of loosening has been identified and confirmed by medical specialists showed that a narrow dark intensity region exists outside the prosthesis near points of loosening.

In figure 4.2, points of interest (POIs) are marked on the surface of the prosthesis as A, B, C, D, E, F, G and H respectively; it is clearly seen that the curvature at these key points vary significantly along the boundary. In general, for a 2D curve, curvature is defined as the reciprocal of the radius of a circle that is tangent to the given curve at a particular point as illustrated in figure 4.1. Note that the anticlinal features are assigned to a positive value while synclinal features has a negative value [66].

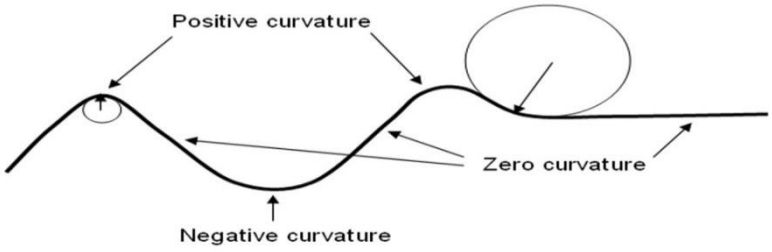

Figure 4. 1: An example of 2D curvature of a line, anticlinal features have positive curvature, synclinal features have negative curvature and planar features (horizontal or vertical) have zero curvature.

For the two prosthesis illustrated in figure 4.2, at points between points A and B, the direction of the tangent vector would not change indicating a region of

zero curvature points. From point B to C, the direction of the tangent vector changes sharply and we would expect the curvature to be inscribed in a circle tangent to the curve where the radius of curvature fluctuates in its absolute value. The same applies from point C to D, where at points in particular closer to D and slightly beyond the tangent changes in direction to what it was at point C. Similar explanations can be given for points on the prosthesis boundary between points E to H. When carefully inspecting the prosthesis of both images in figure 4.2 and any other design of a prosthesis it is seen that curvature of points between A to B (approximately) remains as 0, increases, peaks and decrease to a very low value between B to C, keeps low and again increases to a significant value at D which is the point where the circular cup area begins. Similarly the curvature at points between E to F remains close to zero, increases and decreases to a low value from F to G, continues to be low until very close to H and then increases significantly at H which is the start of the circular cup area.

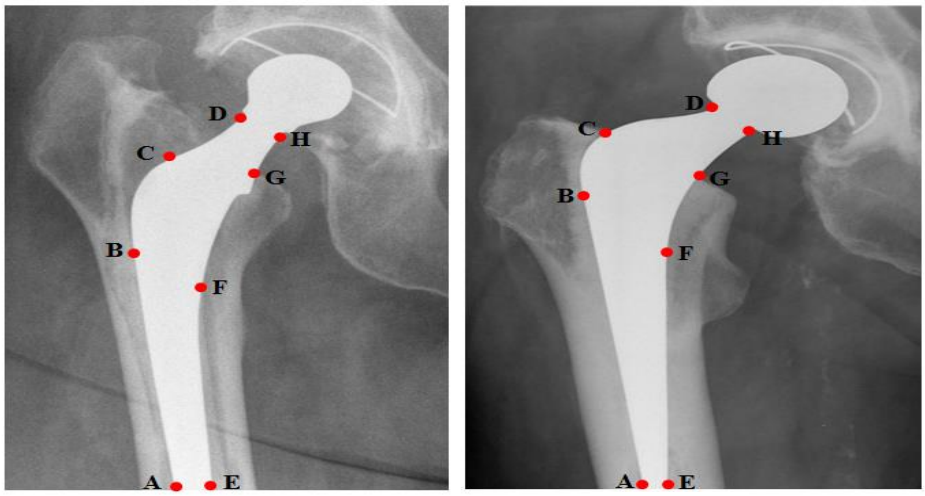

(a) **(b)**

Figure 4. 2: POI identified within X-ray images (a) with loosening and (b) without loosening

In figure4.2 (a) and (b), illustrates two THR images with loosening indicated in figure 4.2 (a) and a perfectly cemented prosthesis indicated in figure 4.2 (b). The

design of prosthesis is such that when properly sealed within the cement placed within the hole/shaft drilled in the bone, all points between A-C, E-F and especially the point with the highest curvature between B and C are securely placed within the cement. If this is the case the pixel value variation from within the prosthesis to the outside, will change from the pixel value of the bone to the pixel value of the cemented areas. This can be clearly understood by analyzing pixel values inside and outside the prosthesis boundary, between points A-C and E-D of figure 4.2 (b). As long as the cement is secure and secures the prosthesis within the bone the pixel value gradients in the above regions remain similar and low.

However in the presence of loosening, the pixel value variation across the boundary of the prosthesis from inside to outside, changes between points A-C and E-D, showing higher variations at points that indicate possible loosening or breakage of the cement bonds. The gradients will increase at these points. This is illustrated by figure 4.2 (a) that shows a prosthesis that indicates loosening in the region E-F-G. The pixels just outside the bone are not from a cemented area but much darker background pixels of the area where the cement has disintegrated. It is also common that where ever severe loosening occurs subsidence is also present. This is also illustrated by the example in figure 4.2 (a). The point with the highest curvature between points B and C and at point C, the pixel value variation is now different changing from the pixel value within the prosthesis to a pixel value of a non-cemented/background area, i.e. a rather smaller pixel value. Hence the pixel value gradient increases beyond point B in the presence of subsidence due to loosening. It is noted that in severe cases of loosency, subsidence is often present.

In the sections that follow, the above observations are used in the analysis of THR images in search for the presence of loosening. Even though the approach used in this chapter can also identify subsidence, in chapter-5 we study subsidence and its detection in more detail as there is possibility to conduct a more detailed analysis when subsidence is present in the absence of loosening.

4. 3 Block Diagram of Pre-processing Steps

In Chapter-3 it was mentioned that the precise extraction of prosthesis edge is vital in subsequent identification and recognition of loosening in THR images. The concept presented in section 4.2 revealed in more detail the possible use of the prosthesis boundary points and pixel value variations across the prosthesis boundary at selected key-points can lead to effective detection of loosening. The block diagram in figure 4.3 shows the pre-processing stages used for the segmentation and boundary detection of the prosthesis.

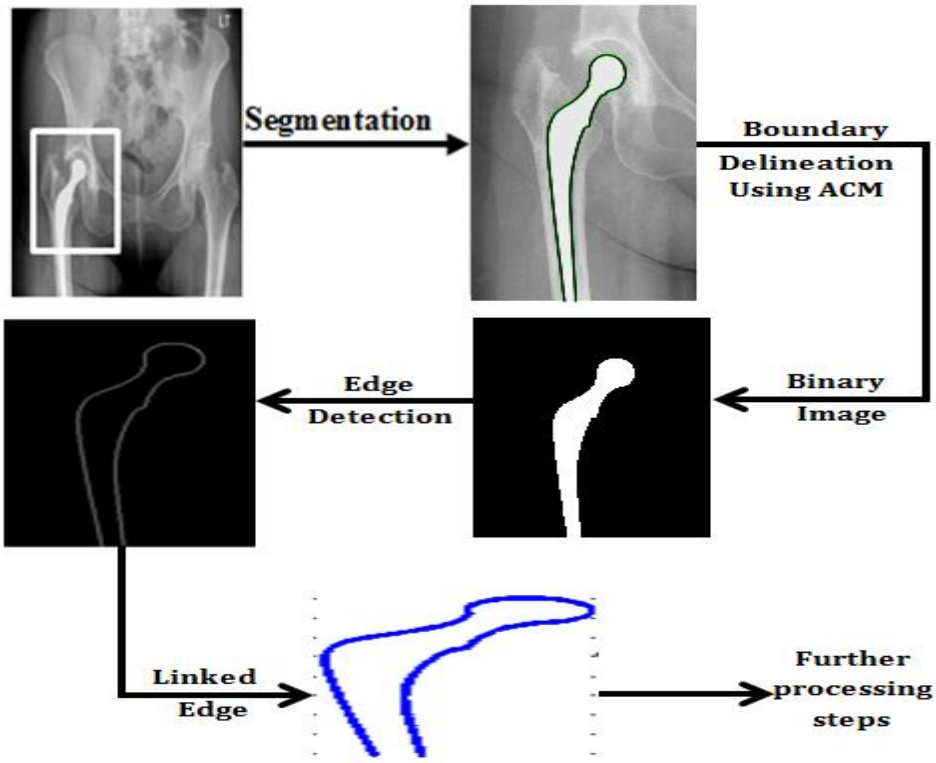

Figure 4. 3: Diagram illustrating the pre-processing steps of detecting the prosthesis

In an x-ray image, the steel prosthesis appears as the brightest object. Thus, the initial step is to segment the region with the brightest pixels in the x-ray image, which has been performed in subsection 3.3 in chapter 3. The prosthesis has been segmented automatically using ACM and a binary image is generated that is used to create an edge map. The edge map is traced using edge link algorithm; more details of which is presented in the following subsection.

4. 4 Generate and Trace Edge Map

To compute curvature information of an edge; we need to generate an edge map. For this purpose we employ Sobel edge detection [62]. The result of edge detection is an edge map of the prosthesis which contains pixel values of all pixels that lie on the prosthesis boundary. However, typical edge detection methods like sobel have a major drawback that the edges detected may not be continuous as noise and/or lack of contrast will often result in breakages. The edge detectors are tuned to detect step edges, as illustrated in figure 4.4(b).

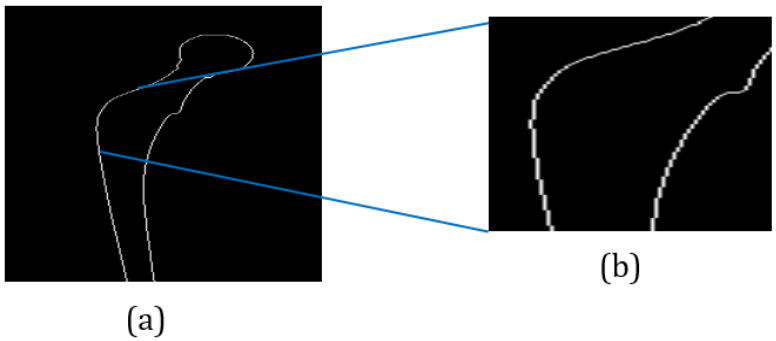

Figure 4. 4: Detected edge (a) using Sobel operator and (b) step edge

Further, the proposed work requires tracing the edge pixel information in sequence, thus, a further step is carried out to trace the detected edge using an edge link algorithm. The edge link algorithm ensures the connectivity of the edge contour

and sorts the pixels as a sequence of points *(x, y)* that represent the shape of the boundary. The algorithms start scanning the image and locate the edge pixels precisely from the points detected by Sobel edge detector. We define the start point of scanning for edges as the bottom-left point of the image. All the traced pixel points are stored in a list. Although this step is necessary to accurately sort the pixels into a proper list for further processing, it does not solve the issue of step edges of figure 4.4(b). To deal with this problem, the detected step edge was smoothened further using an Average Filter [67], see figure 4.5.

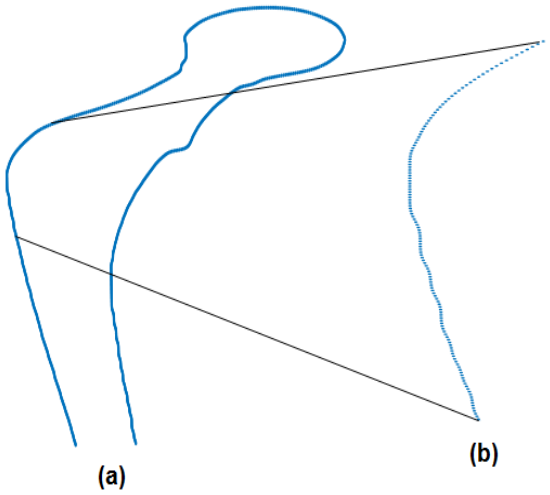

Figure 4. 5: (a) Smoothed edge map and (b) smoothed edge

Subsequent to obtaining a smooth and connected edge map of prosthesis following the procedures described above, we can compute the curvature for each point, traversing along the contour as explained in the following section.

4. 5 Curvature Calculation at Each Point on the Contour

The goal of finding the curvature *K* of a point on the prosthesis contour is to discriminate linear features either straight or curved along the outer line of the

contour. Considering that the prosthesis contour is defined as a continuous curve of a set of points having position vectors of (*x, y)* that are the coordinates; then any changes in position vector is specified by its tangent slope. To describe the rate of curvature change along the boundary points; let's set $P_t = (x_t, y_t)$ to be a coordinate of the edge as mentioned earlier in the edge list. The *k(t)* is a direction vector between points that k edges apart and it is calculated using :

$$k(t) = \frac{d\varphi(t)}{ds} \tag{4.1}$$

The left k-slope is direction from Pk-t to Pt and the right k is slope direction from P_{k+t} to P_t, then *k(t)* is the difference between left and right *k-slop*.

According to the obtained *k(t)* each consecutive point is distinguish immediately and filter out as an new vector; therefore we validate if *k(t)=0* which means that there is no change in the curve's direction at that particular point and the tangent is straight; conversely, if *k(t) >0* , then there is a positive change at that particular point and if *k(t) <0* then there is a negative change at that particular point. Regardless of positive and negative sign of *k(t)*, there is a slope tangent at the particular point if *k(t)* not *0*. Since, *k(t)* values are similar over a series of consecutive points for a small region within the edge, the set of points obtained finally would also include the varying levels of slope details present on the edge. We illustrate the output of the first derivatives along the *x* and *y* directions in figure4.6 (a) and (b) respectively. As the curvature is denoted by *k*, which depends on the calculation of the second derivative, this is illustrated in figure 4.6 (c).

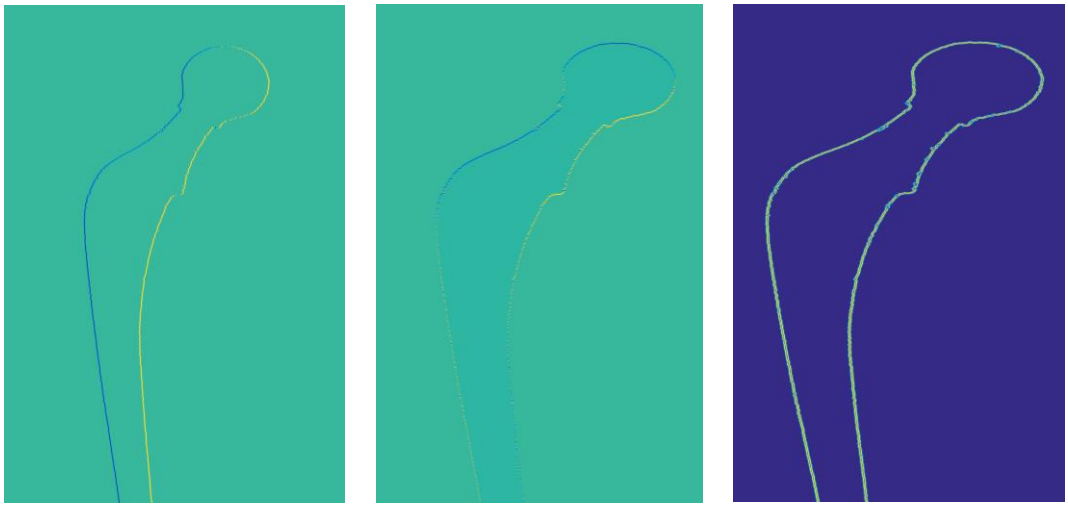

(a) (b) (c)

Figure 4. 6: (a) First derivative of prosthesis contour along x-direction, (b) First derivative of prosthesis contour along y-direction (c) Second derivative of prosthesis contour

4. 6 Computation of Pixel Gradient

The Pixel Gradient can be referred to a direction of greatest intensity change in neighborhood of a pixel of an image. The edge point that has maximum gradient vector variation as can be seen in figure 4.7; mainly varies at few pixels at a transitional area of the pixel intensity homogeneity, especially between an object and background. To define the extreme rate of change between each pixel and its neighbors, we compute gradient vector with respect to edge directions along the x-direction and the y-direction around each pixel.

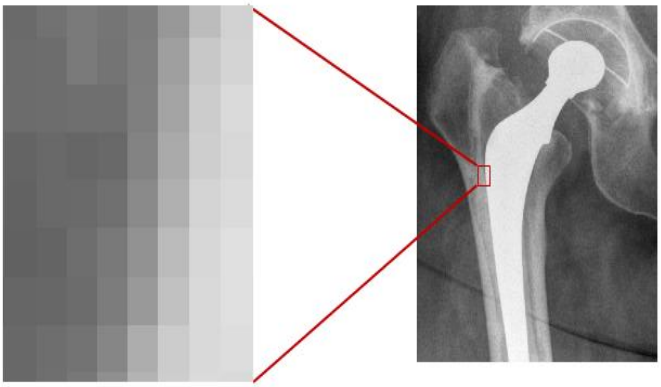

Figure 4. 7: Transitional area between prosthesis and background

This type of computation involves smoothing an image. A 1-D Gaussian filter, with a 0.5 standard deveiation is applied to get a normalized gradient image of figure 4.2 (a). Considering the x and y components of a gradient vector at point A(x,y) are :

$$G_x(x,y) \approx A(x+1,y) - A(x-1,y) \quad and \; G_y(x,y) \approx A(x,y+1) - Ax,y-1)$$

The magnitude of the gradient vector is computed using the standard formulas as follow:

$$Magnitude\ of\ G(x,y) = \sqrt{Gx^2 + Gy^2} \tag{4.2}$$

And the gradient rate of change in the direction of the gradient vector, Gx, Gy; is given by the angle measured with respect to the x-axis using:

$$\theta = tan^{-1}(Gy/Gx) \tag{4.3}$$

The gradient orientation of an edge at a G(x,y), is perpendicular to the direction θ ofthe gradient vector at the pixel point[68],where it orient along the direction of maximum rate of increase of the grey level of A(x,y). The gradient vector at the edge pixel can be seen in figure 4.8, that shows the direction of maximal rate from black(or dark gray) A(x,y)=0 to white A(x,y)=255.

Although the gradient vectors point out uniformly within the transitional area in figure 4.8, we can visualize it. The reason of visualizing the gradient direction is to see clearly how it alter with the associated region of the bone and the prosthesis.

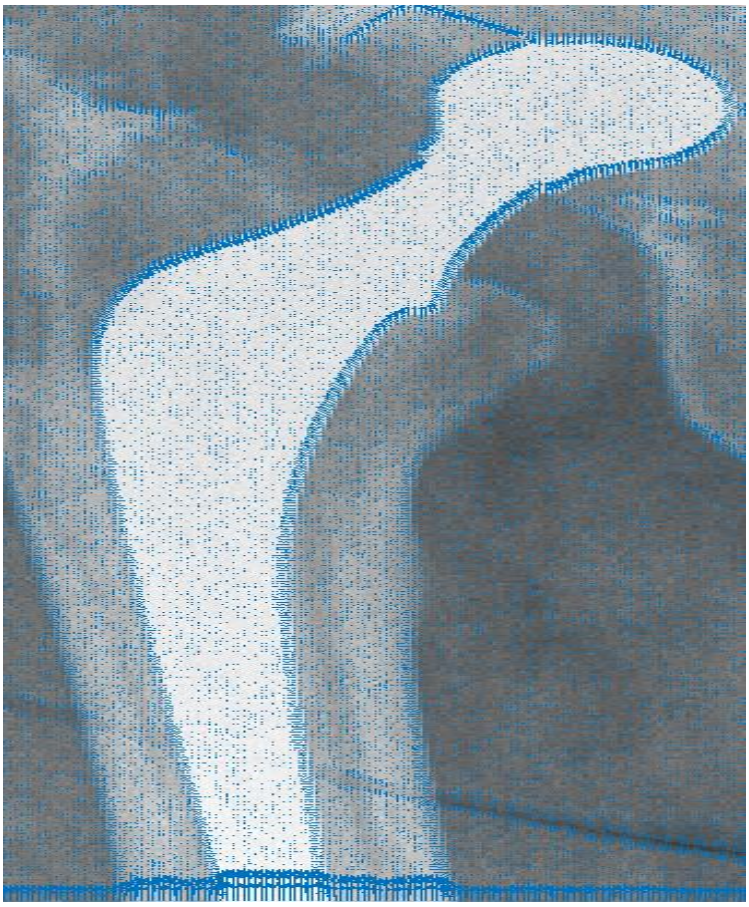

Figure 4. 8: The direction of Gradient vector of THR x-ray image

The edge map of prosthesis has already being obtained via the use of a Sobel Edge Detector in figure 4.4. Subsequently we refine the gradient computation on the generated edge map image; as the gradient at a point on the edge map has vectors pointing toward the edges, which are normal to the edges at the edge level. Moreover, these vectors generally have large magnitudes only in the immediate

transitional area at the edges which we present them in the result section see figure 4.13(a).

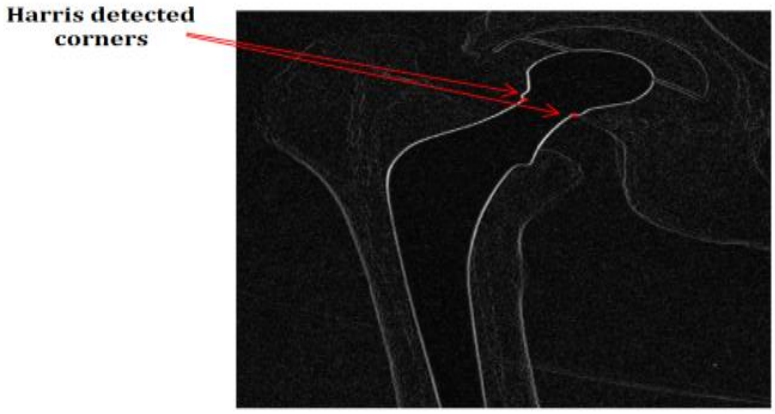

Figure 4. 9: Corner detected using Harris algorithm on gradient image

For detailed analysis of loosening, two important points D & G marked in red in figure 4.9 of the prosthesis are defined as end points of calculating gradient, because beyond these points we can not define the presence of loosency. We use Harris Corner Detector [58] to recognize these points.

4. 7 Results Analysis

To investigate the performance of the proposed in terms of reliability and robustness in automatically identifying loosening in THR x-ray images, we tested it on normal and abnormal x-ray images of THR. Given a THR image the first step therefore is to extract the prosthesis and subsequently obtain edge map of the prosthesis. Pixels along the edge are numbered starting from the bottom left-most point on the prosthesis as pixel, 0 (point denoted by A in figure 4.10). Point E is the

bottom right-most point on the prosthesis. Figure 4.10, illustrates the curvature value plot for all pixels on the boundary of the prosthesis of figure 4.2(a), note: this is an image indicating loosening.

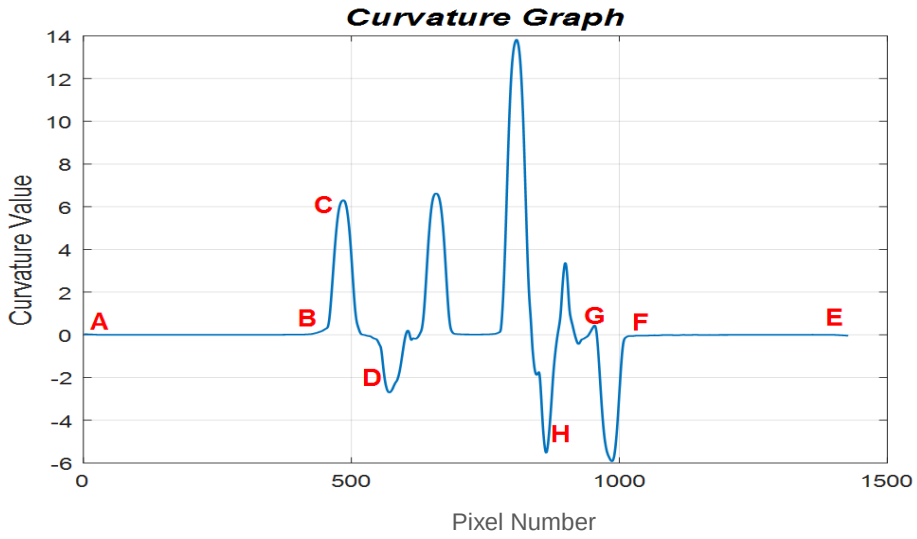

Figure 4. 10: Curvature graph of figure 4.2(a) showing loosening

In reference to figure 4.2(a), point A and B indicates start and end of the straight line area of the prosthesis boundary on the left side of the stem of the prosthesis. Both points show a zero values curvature. Point C that is indicated by a positive peak in figure 4.10, refers to the point where the prosthesis bends sharp. The point D with a negative peak illustrates the point on the prosthesis that bends to the right in figure 4.2 (a), just before the start of the circular cup part. The two peaks between Peaks marked as D and H in figure 4.10, reveal the start and end of the circular prosthesis cup. These two points of a less importance in determining as points on the cup part are within the movable parts of the prosthesis and thus will be not cemented to any fixed bone of the human body for loosening to happen. Starting from point E which is the right-most bottom point of the prosthesis a

similar explanation can be given about the curvature values obtained for points E, F, G and H as marked in figure 4.10.

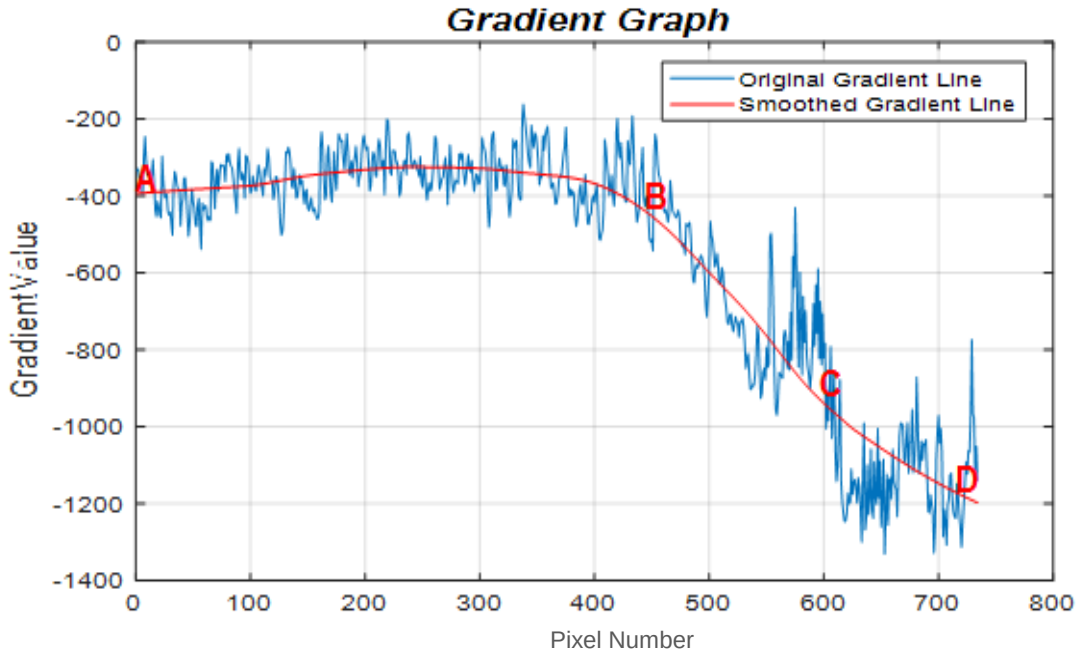

Figure 4. 11:Gradient graph of figure 4.1(a) from point A to point D showing loosening

figure 4.2 (a). It is noted here that this THR image shows signs of loosening as indicated by the slightly dark textured areas just outside the edge AB of the prosthesis and even darker areas outside the prosthesis closer to point C which should have been embedded within securely cemented (i.e. bright) areas. The pixel gradients across the boundary of all points between A and B are somewhat larger (above 200) indicating the presence of disintegrated cement bonds. The gradient at C is significantly high indicating that in the immediate vicinity of the point there is no cement present, which leads to determining the presence of loosency.

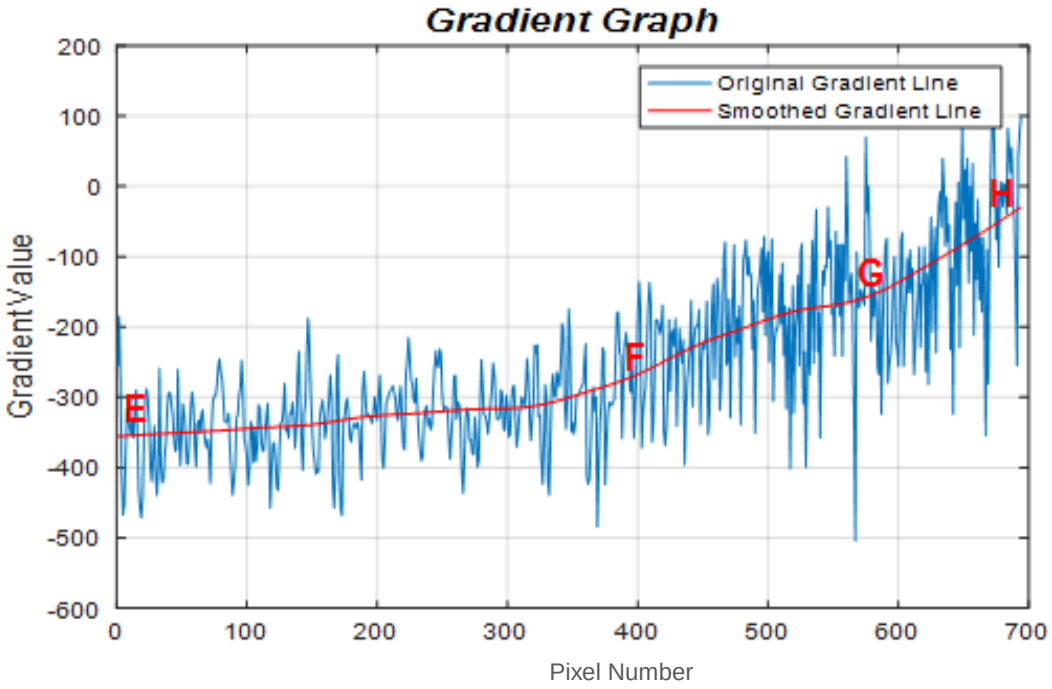

Figure 4. 12: Gradient graph of figure 4.2(a) from point E to point G with loosening

Figure 4.12, illustrates the Gradient graph of the right side of the prosthesis of figure 4.2 (a). It is noted here that this THR image shows signs of loosening as indicated by the slightly dark textured areas just outside the edge EF. The gradient values which are in excess of -300 is beyond the gradient value that will be obtained if the cement was intact just outside the prosthesis boundary in this area.

Figure 4.13, provides an illustration of gradient direction at two points of the prosthesis boundary in its left side. The two example of (b) and (c) points out the direction of maximal gradient where in (b) the gradient vector appear as intense dark blue colour represent higher values of gradient which obviously, indicate a region of gap between bone and prosthesis. Whereas in (b) the gradient vector appear as light blue colour represent lower values of gradient which clearly indicates a homogeneous region between the bone the prosthsis.

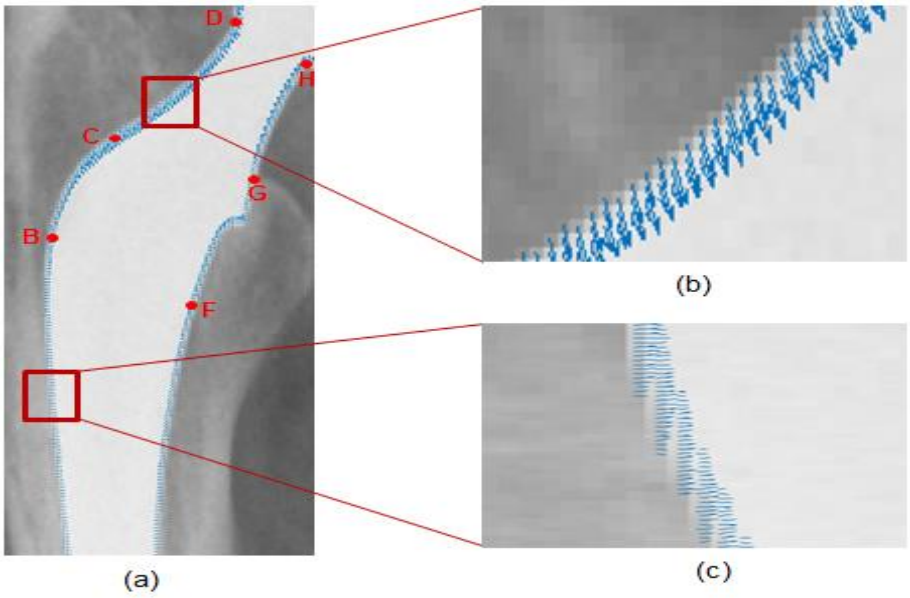

Figure 4. 13: (a) Gradient vector of figure 4.2(a), (b) Gradient vector at the curved level of the edge contour and (c) Gradient vector at the straight level of the edge contour

Another example of a loosened THR x-ray image is presented in figure 4.14. The POI along the contour, A-D and E-H, are marked using a procedure similar to that described above.

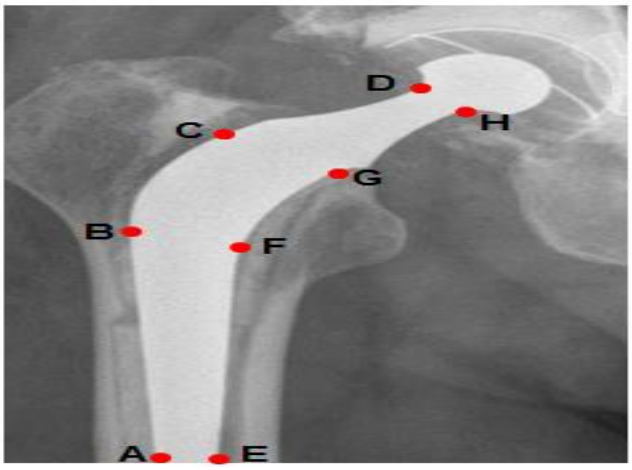

Figure 4.14: Another example of loosening in THR

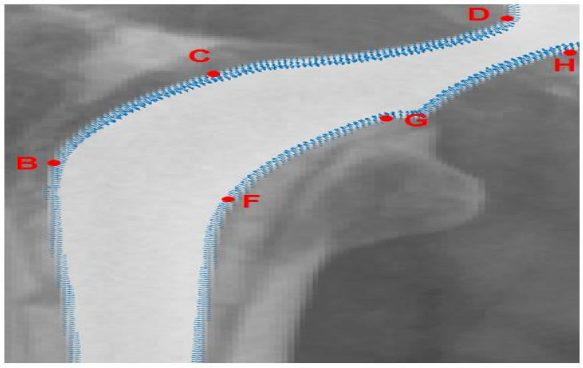

Figure 4.15: An illustration of the gradient vectors of the prosthesis of figure 4.14

Figure 4.15, illustrates a visualization of the gradient vector variation of the prosthesis of figure 4.15 at along the contour points. The variations indicate the presence of loosening on both sides of the prosthesis and subsidence starting from B to the mid-way point between C&D. Note that the edge contours have been smoothened and this has resulted in a gradual variation of gradients.

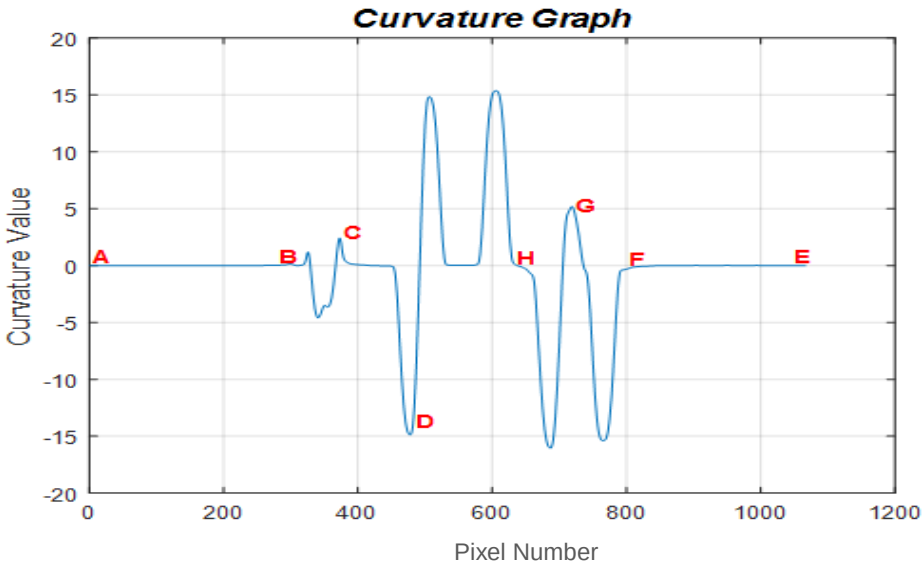

Figure 4.16: Curvature graph of figure 4.14 showing loosening

The presented curvature graph in figure 4.16; shows zero-curvature values at all points between A and B as well as all **points** between E and F. These areas correspond to the straight edges of the prosthesis stem see figure 4.14 and hence the reason for zero curvature. The readings of curvature values between points B and C differ from that of figure 4.10; which can be attributed towards the shape differences between the prosthesis. However, from point B the curvature values decrease and then increases followed by sharp decrease at point D, which corresponds to the edge point near to the circular area of the prosthesis of figure 4.14. The points between F-H have similar curvature rate change patterns that can be attributed to the shape in figure 4.14 of the prosthesis. The above attributions lead to the identification of the precise location of key points along the prosthesis boundary.

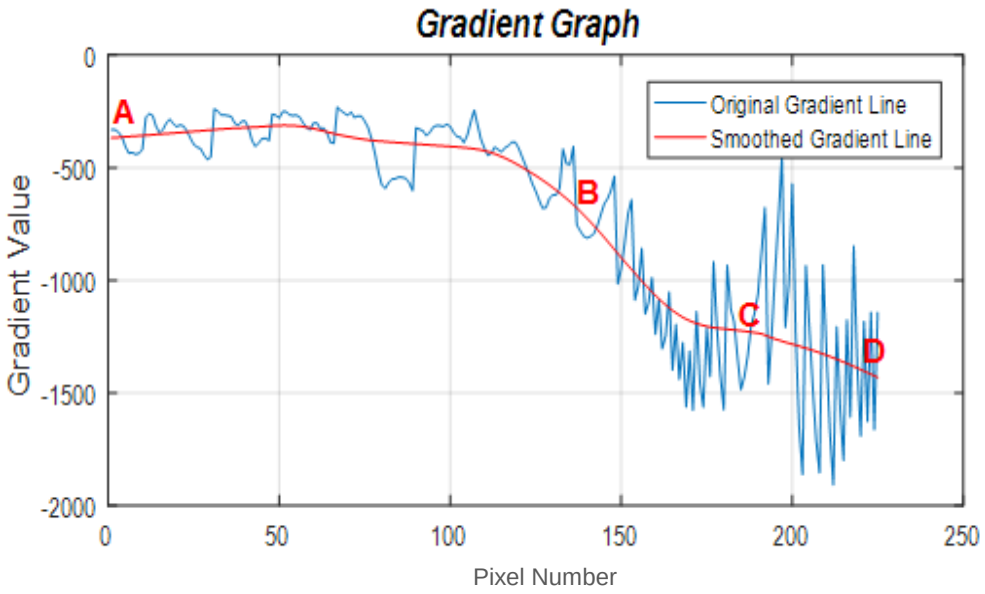

Figure 4.17: Gradient graph of figure 4.15 between points A (bottom of prosthesis) to D, as also (marked in red) in figure4.14 showing loosening

As can be seen from the gradient graph of figure 4.17 the gradient values remains high (negative) and stable from point A-B indicating the presence of loosening and increases further beyond point B and C. It is noted that the presence of subsidence in soon after point C and towards point D. Given the fact that all steel implants will appear as similar in brightness a gradient value beyond 150 in magnitude indicates the presence of loosening for most types of cement used for bonding.

Figure 4.18: False corner point is detected

It is noted that not all the steel implants are the same in shape. Therefore, the prosthesis edge contours differ as observed in figure 4.18; point G is detected as corner point which is incorrect. False corner points can be detected at both sides of prosthesis edge. However, by testing five different implant shapes and with the edge contour smoothened; it was found that the smoothing results in detecting the ideal corner as an end point, especially, on the left side of the edge (from E to H), where, the detected corner points might become two. This was simply resolved by considering the last maximum detected corner point as H as can be shown in figure 4.19.

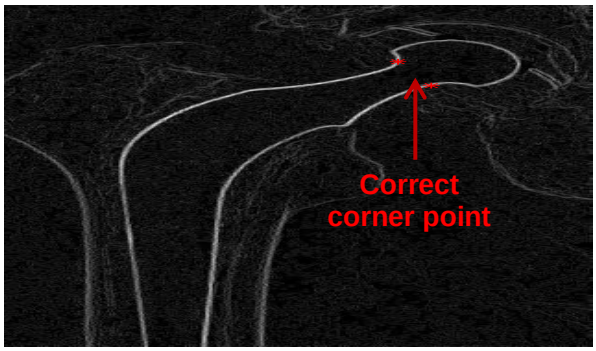

Figure 4.19: The desired corner point is detected as an end point

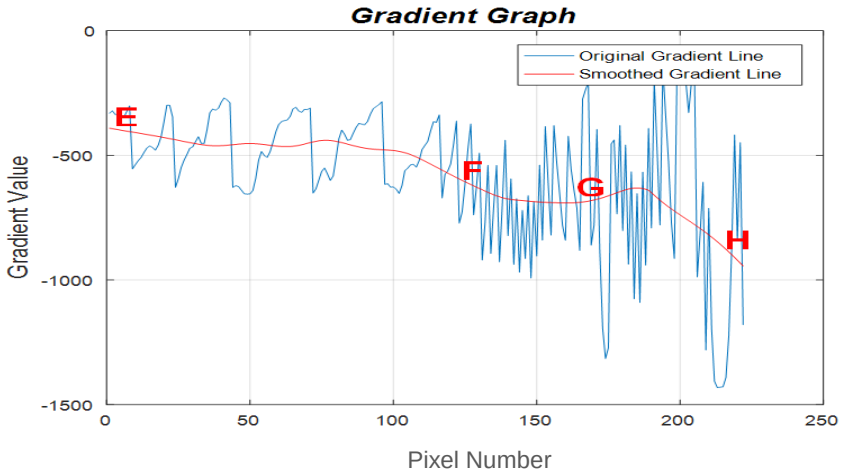

Figure 4.20: Gradient graph of figure 4.15 between points E (bottom of prosthesis) to H (marked in red) in figure 4.14 showing loosening

Thus, the reading of gradients at points E-H is presented in figure 4.19; the gradient values increase slowly starting from about -350, indicating the presence of loosening, and is followed by a slightly stable maintenance of gradient between -500 to -600 between points F-G. Beyond point G the gradient increases further and sharply. By comparing the gradient graphs obtained for the prosthesis illustrated in both figure 4.2 (a) and figure 4.15, we can see the general trend of pixel gradient value variation is similar from points A-D and from points E-H.

The above observations of variation of gradient vectors in figure 4.15, along the boundary can be compared with the same of prostheses that do not show the presence of either subsidence or loosening see figure 4.2(b). The same key-points were detected along the boundary by analyzing curvature value changes along the boundary of the prosthesis see figure 4.21. When comparing figure 4.10 with figure 4.16, it is obvious that the curvature values are quite different. This can be attributed to the difference in shape of the prostheses.

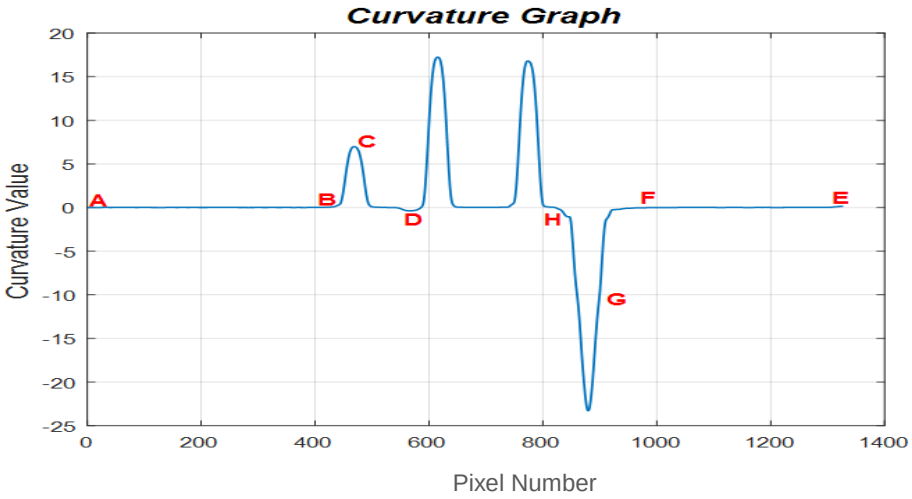

Figure 4.21: Curvature graph of figure 4.2(b), without loosening

Between A-B and E-F the curvature values are maintained at zero indicating that the two sides of the stem area are straight. The curvature value of the left side of the prosthesis increases to a maximum at point C as expected, which is followed by a straight line area just beyond C. At point D the curvature begins to peak. A similar explanation can be given to the curvature value changes on the right side of the prosthesis from E to H.

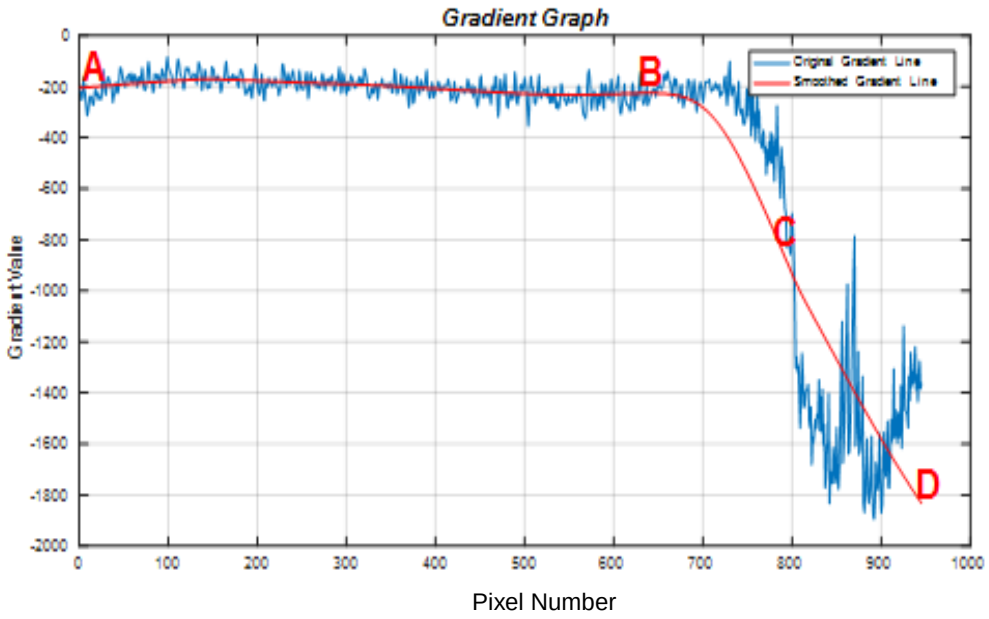

Figure 4.22: Gradient graph figure 4.2(b), between points A to D, without loosening

Similarly, the gradient graph in figure 4.22; also, appears to be quite different from the gradient graph depicted in figure 4.11. As can be seen, the gradient values in figure 4.22 between points A to B remains constant and low around -200 and steadily increases after B and C. When inspecting figure 4.2 (b) it is revealed that this is a THR image where in the surgical proses, bonding cement has not been used. Instead the steal part has been pushed in tight inside the bone. As the bone is slightly darker in colour than the cement our previous threshold value, -150, to check whether loosening happens, now need to be increased substantially in magnitude. As there is no loosening apparent between A & B one thing we are certain is that the threshold now needs to be increased at least just above -200.

Figure 4.23, illustrates the gradient value changes on the right side of the prosthesis. Again the gradient values remain largely constant from E to F and subsequently increases after F and after G in magnitude. Given that we are aware that this prosthesis binding does not involve the use of a cemented bond, the

threshold value requires to be set over about -370 if this THR is to be classified as not indicating loosency.

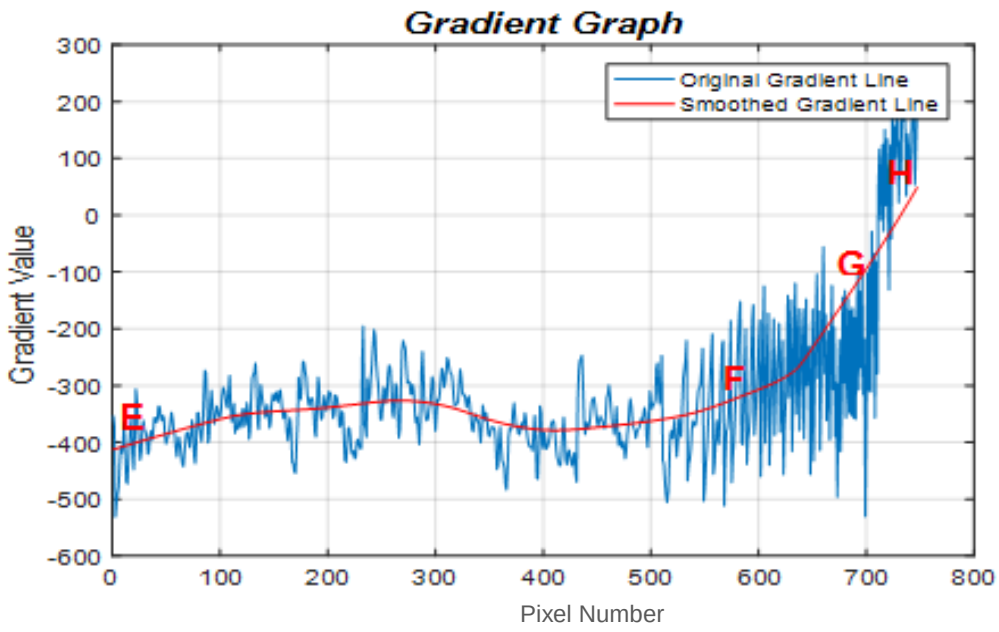

Figure 4.23: Gradient graph figure 4.2(b), between points E to G without loosening

The above experimental results reveal that setting the appropriate threshold is important in order to come to the correct diagnostics. Especially it should be checked whether the bonding is done as tight or as a cemented bond.

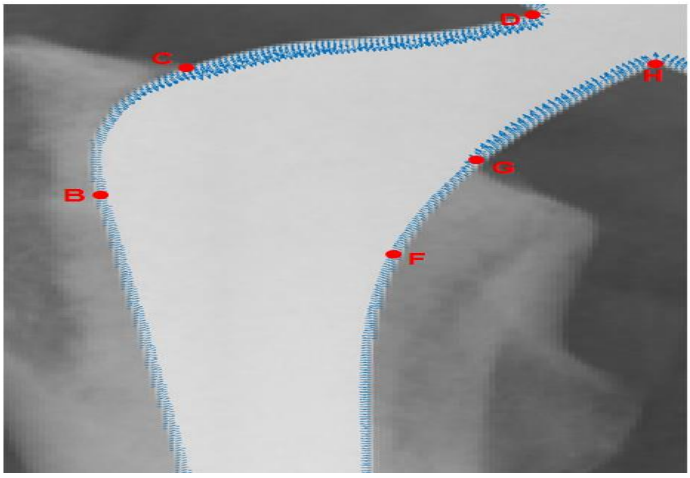

Figure 4.24: (a) Gradient vector of figure 4.2(b) straight and curved level of the edge contour along the sampled POI

Figure 4.24, visualises the gradient value change around the contour of the prosthesis of figure 4.2(b) in which loosening or subsidence do not appear. Very low and constant gradient values in the regions A-C and E-G indicates that there is no loosening. Some early sings of subsidence is however demonstrated when considering the slightly increased gradient value to the points immediately to the left of point C.

As the presence of loosening is demonstrated by the presence of dark regions just outside the straight edges of the stem area of the prosthesis, when loosening is present in these regions, if the magnitude of gradient values increased beyond, 150 for a cemented bond and 350 for a non-cemented (bone to metal/steel) bond. It was shown that the detection of the presence of loosening can be carried out accurately by a comprehensive analysis of gradients as explained above which can provide the medical expert a clue whether there is loosening or not. Results in relation to carrying out the search for the potential present of loosening was demonstrated using two THR images that demonstrated loosening figure 4.2 (a) , figure 4.14 and one that did not indicate loosening in figure 4.2 (b).

Further results are provided in the appendix-A of this thesis is support of the results already presented within the chapter.

4. 8 Conclusion

This chapter has presented a scientific approach that can be followed to detect the presence of loosening in THR images. After following the steps proposed in Chapter-3 for the extraction of the prosthesis, the boundary pixels of the prosthesis were located and numbered for traversal. Subsequently a curvature analysis along the boundary was conducted to determine a number of key feature points present in any prosthesis. In relation to these extracted key-points, pixel gradient changes across the boundary of the prosthesis were calculated.

The experiments conducted in this chapter also revealed that often when sever levels of loosening is present, there is an indication that subsidence will also be present. However there will be cases where subsidence is present in the absence of loosening. Chapter-5 will present a more refined and detailed approach to the analysis of presence of subsidence.

Chapter 5.

Detection and Localization of Interest Point to Diagnoses Subsidence in THR Radiographs

5. 1 Introduction

Prediction of implant stem subsidence in x-ray images of THR is a challenge due to the discrepancy between the cavity at the end of the implant, a possibly sinking prosthetic in the bone along with other common THR defects such as loosening. Number of studies indicated that cemented femoral components that subside greater than 1 mm run an increased risk of loosening as early as four to seven years after implantation [71, 72, 73]. Therefore there is a need to develop a reliable technique to automatically assess any evidence of early subsidence in order to reduce the impact of subsidence on the prosthesis and hence the patient. The determination of subsidence can be used as means for predicting possibilities of fracture, identifying loosening of the femoral component, determining implant component instability and a need for revision surgery.

This chapter proposes a novel approach to automatically detect subsidence in THR x-ray images which is initially based on the detection of some key interest points. This chapter starts with section 5.2 that describes the proposed concept of subsidence detection from a clinical point of view, literature review and how it differs from loosening (chapter 4) because both dilemmas are related. Section 5.3

presents the experimental results and a comparison between THR x-ray images with and without subsidence. Finally section 5.4 concludes the work presented in this chapter.

5. 2 Subsidence Detection

In clinical practice, subsidence of the prosthesis is assessed manually and indirectly after several attempts of the radiographer measuring changes in the relative positions of the prosthetic convex and cement interface or bone interface in the THR x-ray image as shown in figure 5.1 (b). In other words, it is the gap at the convex of the prosthesis that seen in figure 5.1 (b) between the two positions, A and B. From the ideas presented in literature reviewed a straight, distally tapered implant femoral stem is usually not a sign of loosening as the graft compaction around hip stems provides a stronger predictor of subsidence than the stem design [74]. Loosening as defined in chapter 4 is the radiolucent dark lines around the prosthesis. As known to clinical practitioners the measurement of any expansion of radiolucent lines around prosthesis at some later stage of THR subsidence can be considered as a loosened prosthesis due to the instability of the prosthesis at this stage. Therefore, there is a clear relationship and also a similarity in the ideas being proposed in this thesis for detecting the two THR complications, loosency and subsidence. Identifying the dark pixel intensity areas just outside the prosthesis, in the vicinity of the most convex point of the prosthesis means the presence of subsidence and around the prosthesis stem means the presence of loosening. Thus the difference between these two THR complications is the ***region of interest*** where the dark pixels (hence higher pixel gradients) are found. Consequently, the proposed method of detecting both THR complications is based upon the accurate identification of each region of interest in THR x-ray images. Further, the

subsidence detection is executed accurately based on the theoretical and clinical aspects that were discussed in detail in chapter 2, subsection 2.2.2.2. As indicated, subsidence refers to a condition in which the prosthesis unexpectedly subsides further into the cement or bone; if this happens, an area of darker intensity is clearly visible (for example, in figure 5.1 (a), this is visible just above the convex bend near the top of the prosthesis). In figure 5.1 (a), region of interest is marked on the prosthesis as A and B; the points in between A & B that lie on the boundary of the prosthesis represent the convex part of the prosthesis.

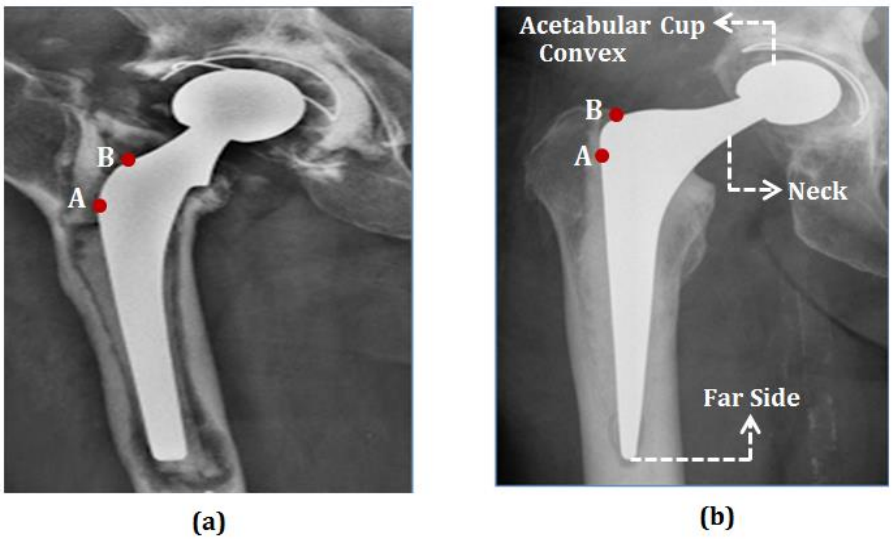

Figure 5.1: ROI identified within X-ray images (a) with subsidence and (b) without subsidence

In the proposed approach for subsidence detection the main key point is detected as the point with the highest curvature on the convex side of the prosthesis stem. Once the point is identified it can be used as a reference point to segment the surrounding region for further analysis whereby, points on the prosthesis boundary showing, brighter pixel intensity neighbours just outside the prosthesis signify a perfect fit; and darker pixel intensity pixels signify abnormality

or the absence of the cement bonds. The automatic detection of the above key-point requires a corner detector.

Although the notion of a corner according to figure 5.1, seems intuitively unclear, according to Guru et al. [75] a corner is defined as the intersection of two adjacent relatively straight curve-segments. Thus the corner point is found at a location where the direction of the curve changes abruptly and this also might include T-junctions as well as locations of significant texture variations. Conversely, state that information of a curve where the points are dominants have a high curvature regardless of whether the contour shape is either a close contour or an open contour. Several algorithms have been proposed with this regard [76] [77] [78]& [79]. A reliable method that is used to compute the curvature extreme points on a curve is curvature scale-space (CSS) [80]. This method is used widely as a corner detector on an edge contour for object matching, shape analysis and pattern recognition [124]. Similarly, our proposed method is based first obtaining planar curves using edge detection algorithms and computing curvature maxima points along the extracted contour. Yet, the corners are determined by comparing the curvature maxima points on the contour. The diagram in figure 5.2, describes the proposed approach of interest point detection and segmenting the surrounded region.

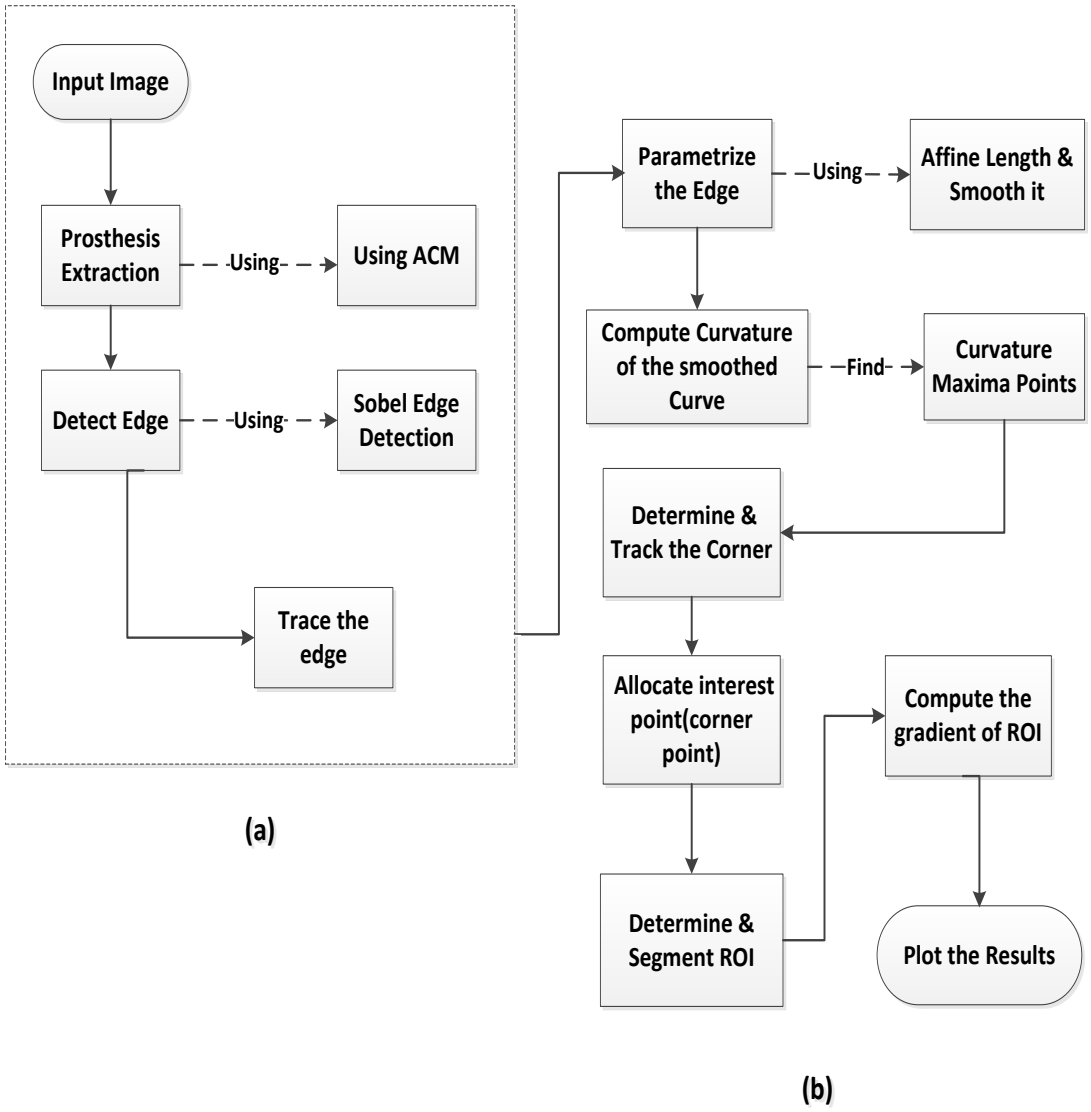

Figure 5. 2:Diagram illustrate subsidence detection;(a) automatic prosthesis detection from chapter 3 and (b) the proposed approach to detect subsidence

The proposed approach includes serval stages; as illustrated in figure 5.2. The part (a) was implemented in chapter 3, where the prosthesis is extracted automatically using ACM and then a sobel edge detection algorithm is applied to detect the prosthesis edge as described in chapter 4. However, within the research

context of this chapter further steps were carried out to detect the interest point, i.e. the 'corner' automatically as described in the following subsections in detail.

5.2.1 Edge Parameterization and Corner Detection

After detecting and tracing the edge, we parametrized the selected edges using an affine length [80] based approach. The affine length is invariant to geometric curve transformation; that derived from images when it is weighted at smoothing different scales. This eliminates spurious details and extract edge feature as "scale space" that are more stable for curvature estimation and provide more accurate corner detection performance. The curve is smoothed prior corner localization in order to differentiate curvature extreme points from other curve points thereafter. Each coordinate of the parameterized edge $T(\tau)$ is convolved with a Gaussian function g_σ of width σ, which is also known as the standard deviation of the Gaussian distribution as in equation :

$$X(\tau,\sigma) = x(\tau) * g_\sigma \text{ and } Y(\tau,\sigma) = y(\tau) * g_\sigma, \quad (5.1)$$

where * represents the convolution.

Following the equation (5.1), each parametrized edge is smoothed using smoothing scales determined based on the number n_s of sample points on it. The smoothing scale set at σ=3, 4, 5 for entire closed contour as if we set σ small false corner are detected and if σ is large important curve details smoothed out. The edge curvature-threshold value, T_K is set to *0.02.* The edge parametrization is defined by $n_s \leq 40$, $n_s > 100$ respectively. Since we have parametrized and smoothed

edge T (τ, σ) =(X(τ,σ), Y(τ,σ)), the derivatives of a convolved function can be computed using:

$$\dot{X}(\tau,\sigma) = x(\tau) * \dot{g}_{\sigma} \text{ and } \dot{Y}(\tau,\sigma) = y(\tau) * \dot{g}_{\sigma}, \tag{5.2}$$

As the exact form of $\dot{g}_{\sigma}$ is identified, to detect the desired corner we look for curvature extreme points that are calculated at each point of the smoothed affine parametrized curve using equation:

$$\mathbf{K}(\boldsymbol{\tau}, \boldsymbol{\sigma}) = \frac{\mathbf{1}}{\left[\dot{X}^{2}(\boldsymbol{\tau},\boldsymbol{\sigma}) + \dot{Y}^{2}(\boldsymbol{\tau},\boldsymbol{\sigma})\right]^{3/2}} \tag{5.3}$$

The absolute curvature values represents strong corners [80] or peaks. Yet, the curvature localization of these point usually prominent because either there is an actual corner or there is a significant change in slope (or convex) along the prosthetic edge. All the true corners are detected as can braly seen in figure 5.4 (a), however, we point out some detected corners along edge contour.

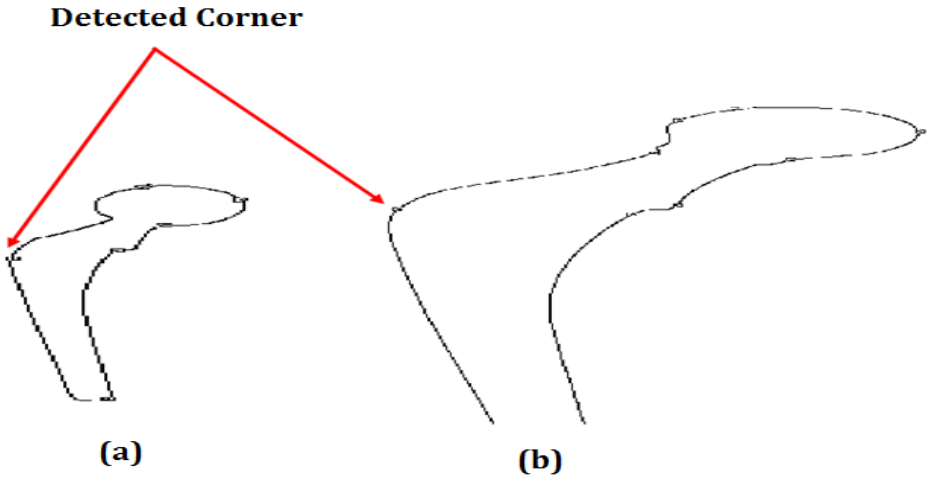

Figure 5.3: Detected corners (a) and (b)

To detect the corner within the ROI between A and B, we subsequently, refined the true corners and eliminate unwanted corners using a threshold. The

corner were initially, set where if curvature value is lower than TK then the corner is removed. Any false corners are removed by comparing with its two neighbor minima on the same edge and if the curvature value of corner is not least twice that of its neighbor minima then it removed from the corner set as well as the very close corners. The corners on T (τ) are tracked and T-corner is added without using any threshold. As a result, only the position of the tracked corners change not the number of detected corners [80].

5.2.2 Interest point Localization and Local Gradients

Once the interest point is determined; an ROI (the red dashed box) is used to surround in center point enclosing the point of interest as illustrated in figure 5.5 counting about 100 pixels (50 pixels to each side) surrounding the interest point and segments the region accordingly.

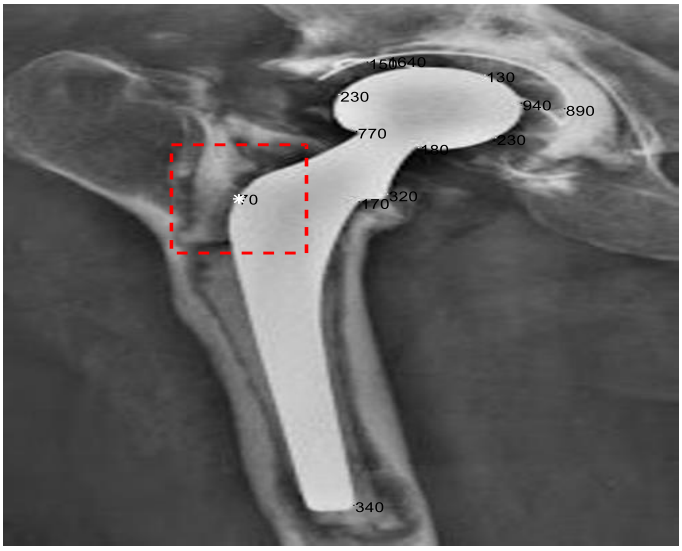

Figure 5. 4: A THR x-ray image with subsidence; interst point is marked in white surrounded with red dashed box

Interest point localization is followed by defining a spatial gradient as the edge gradient information depends on the derivative of the pixel intensity, which is more resistant to illumination variations than the normal gray level(color) of an image. The gradient is calculated using equation:

$$G = \sqrt{Gx^2 + Gy^2} \tag{5.3}$$

$$\theta = tan^{-1}(Gy/Gx) \tag{5.4}$$

where $G_\sigma(x, y)$ and $G_\sigma(x, y)$ are values of the directional derivative of both horizontal and vertical directions respectively at point (x,y) for scale σ. The gradient is computed using multi-scale derivatives of Gaussian kernels to adapt the spatial scale of edges in THR image as seen in figure 5.5 (a).

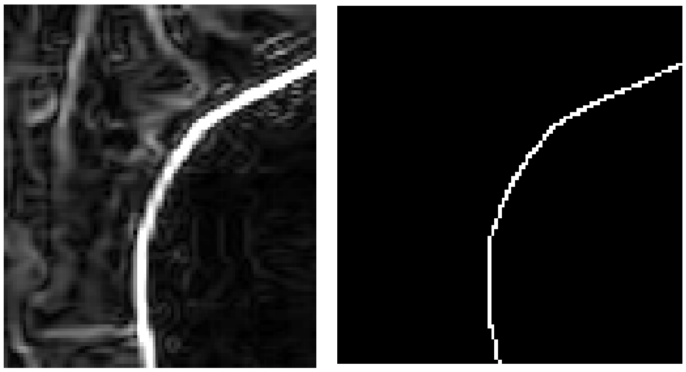

(a) (b)

Figure 5. 5: (a) Sample of Segmented ROI of THR x-ray image of figure 5.4 and (b) edge image of ROI

To ensure that only the prosthesis edge contour gradient is mapped but not the entire ROI; we matched with the edge image as in figure 5.5 (b) with gradient ROI, so, the gradient of edge contour is mapped graphically as is discussed in the next section.

5. 3 Experimental Results and Comparison

Experiments were conducted on THR images that have been annotated by medical experts to indicate subsidence and those THR images that do not indicate subsidence. For each image the key-point is extracted and around the key-point, 50 points along either side of the prosthesis boundary is considered for analysis. With the pixels on the boundary with the key-point numbered as pixel-50, numbered from 1-100, pixel value gradient at each point across the boundary is measured using the presented in section 5.2.2. What follows is a presentation of the results and the corresponding discussions/analysis for each THR image experimented.

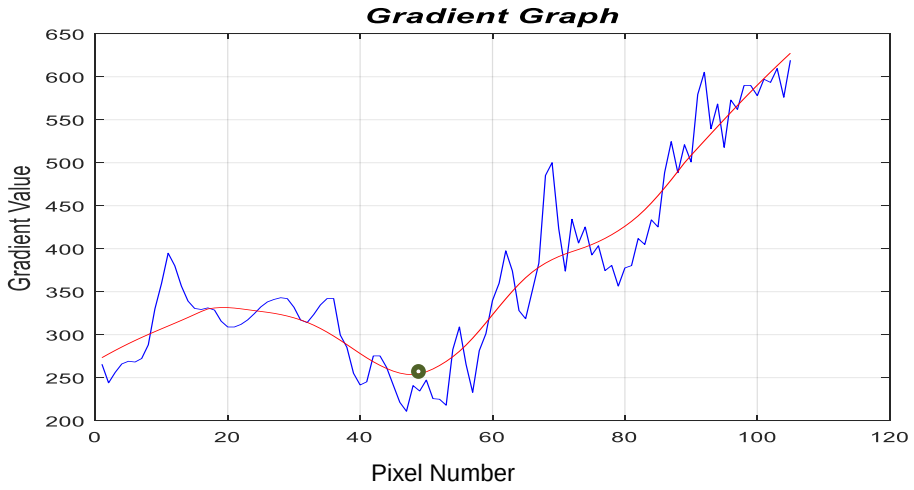

Figure 5.6: Gradient of ROI of figure 5.5

Figure 5.6, illustrates the pixel value gradients across the prosthesis boundary for the pixels within the ROI of the THR image of figure 5.5. The red line shows the smoothened graph. Recognizing that the THR image of figure 5.5 indicates subsidence, this is indicated in figure 5.6 by the continues rise of gradient value after the key-point moving towards the cup area of the prosthesis. As this image also demonstrates loosency, pixls before the key-point also indicates higher

gradient values. This indicates the presence of significant amount of subsidence as the cement bond seems to have disintegrated on both sides of the key-point. Similar observations can be made when inspecting figure 5.7 that represent gradient

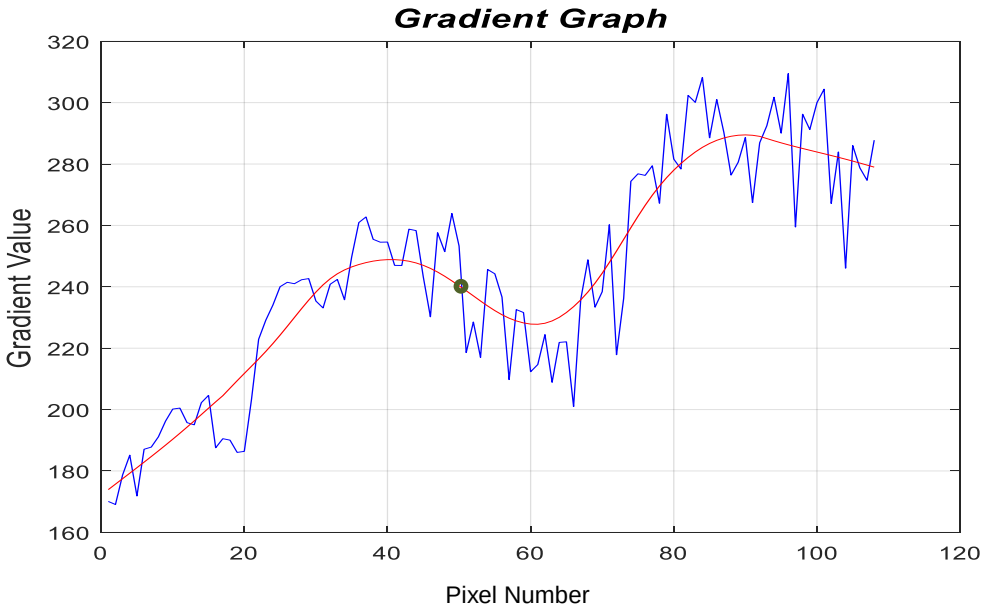

Figure 5. 7: Gradient of ROI of figure 5.8

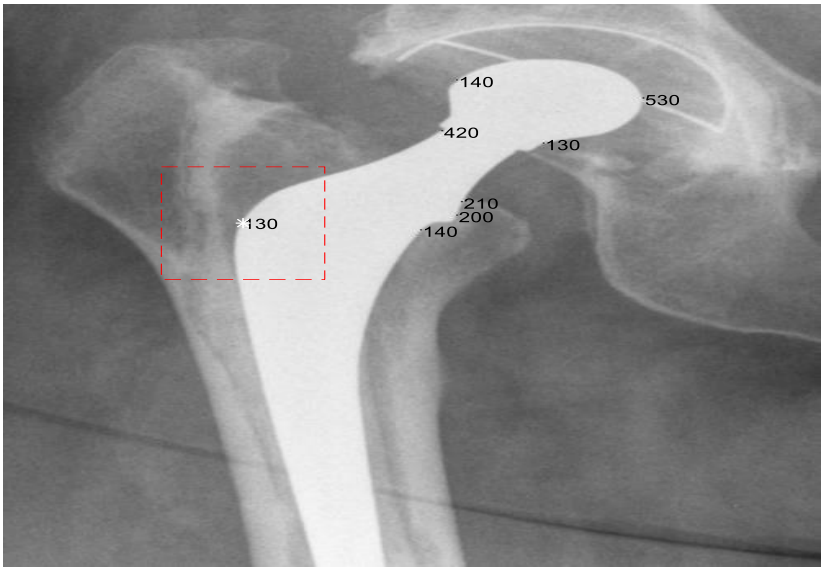

Figure 5. 8: Sample x-ray image with subsdience, ROI is highlight in red

plot of the ROI of the THR image illustrated in figure 5.8. The ROI is highlighted with a red rectangular area. As can be observed in figure 5.7, the pixel value gradient increases from the start of the pixels within the ROI, goes down slightly after the key-point and increases after. The presence of peaks on either side of the key-point illustrates subsidence as this is due to darker regions that are a part of the bone's shaft.

A further example of gradient plot for pixels within an ROI is illustrated in figure 5.9, where figure 5.10 shows the THR image which indicates presence of subsidence. Once again the increased pixel value gradients at points on either side of the key-point illustrates the lack of a solid bonding between the prosthesis and the bone structure.

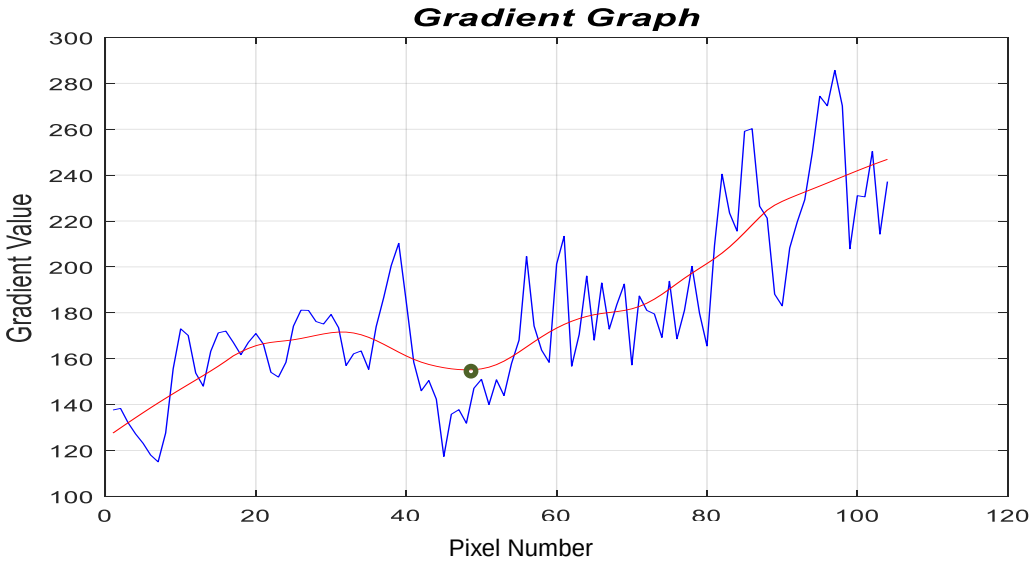

Figure 5. 9: Gradient of ROI of figure 5.10

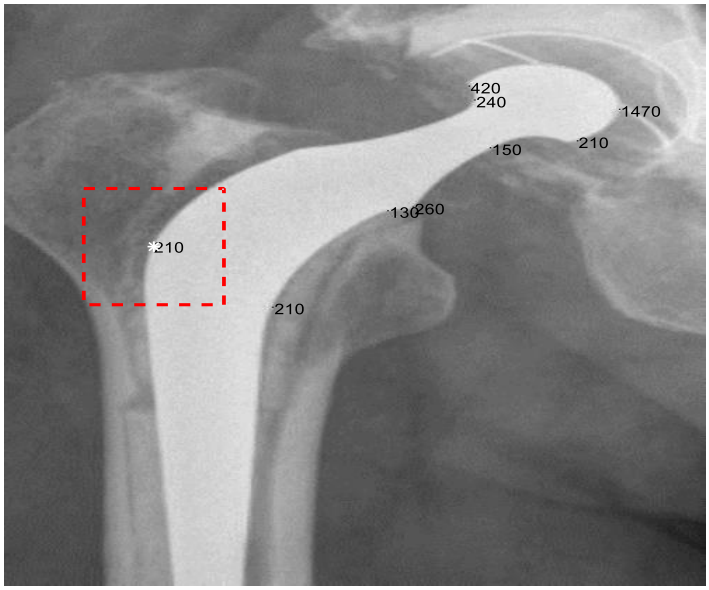

Figure 5. 10: Sample x-ray image with subsdience, ROI is highlight in red

Figure 5.11, illustrates a pixel value gradient graph of pixels within the ROI of the THR image illustrated in figure 5.12. Note that this THR image does not indicate the presence of subsidence. The bonding at the pixels before and soon after the key-point appears to be solid and this is represented by the fact that the gradient graph remaining at a constant low value until and after the key-point. In other words the key-point is embedded within a region that has been solidly bonded, that is the prosthesis is well ponded by cement. The trends indicated by the gradient graph therefore corresponds to a THR image with no subsidence.

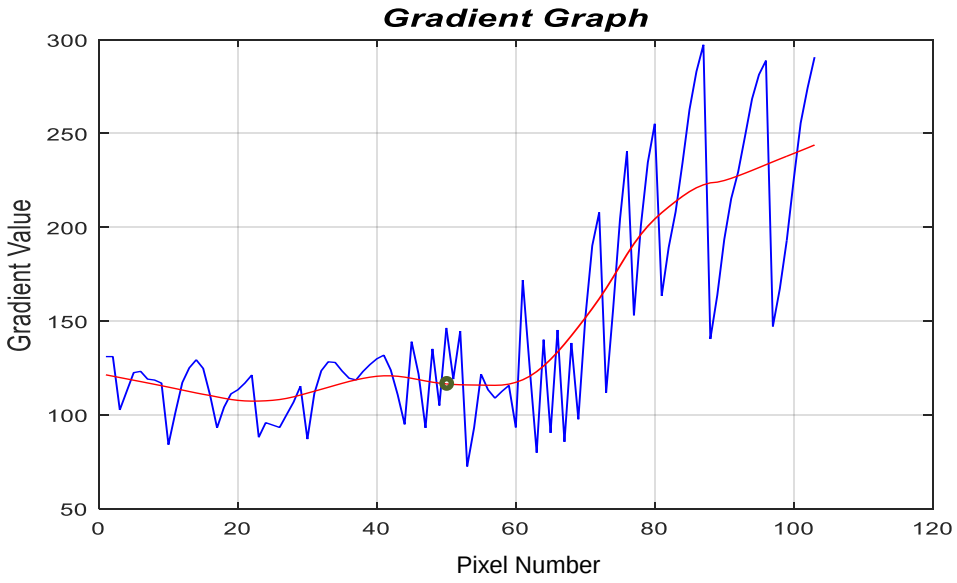

Figure 5. 11: Gradient of ROI of figure 5.12

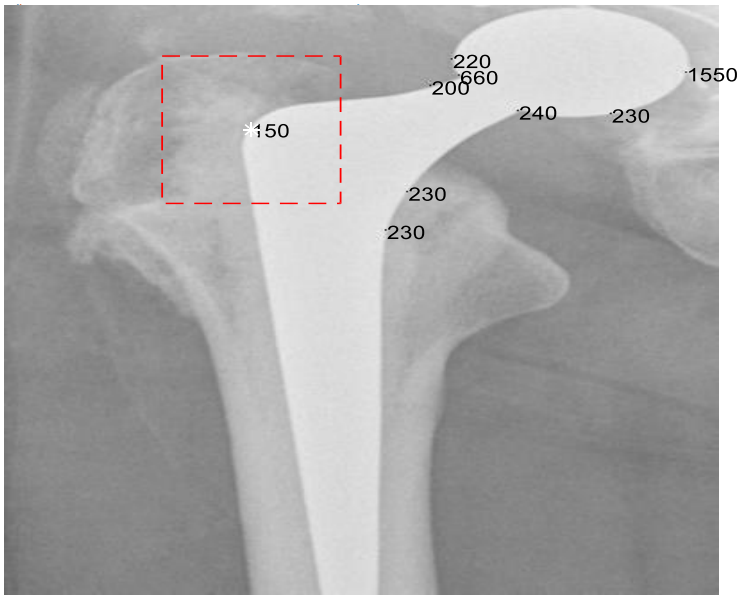

Figure 5. 12: Sample x-ray image without subsdience, ROI is highlight in red

Similar observation of a pixel gradient value trend within the ROI of a THR image with no subsidence figure 5.14 is illustrated in figure 5.13. The inclusion of

the key-point within a solidly bonded area is illustrated by the fact that the gradient values remain at a constantly low value until and after the key-point.

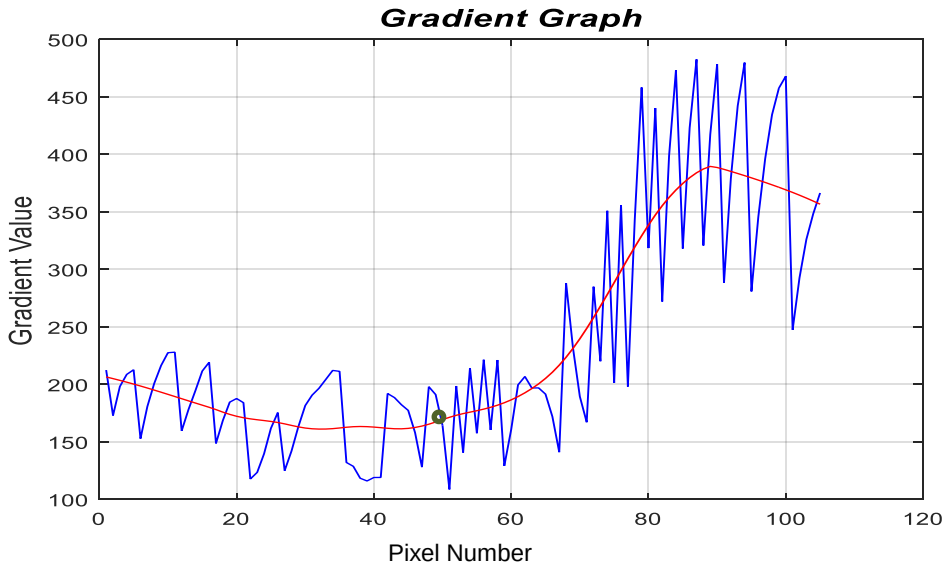

Figure 5. 13: Gradient of ROI of figure 5.14

The figure 5.13 represent ROI of figure 5.14 that as well highlighted with red rectangle box.

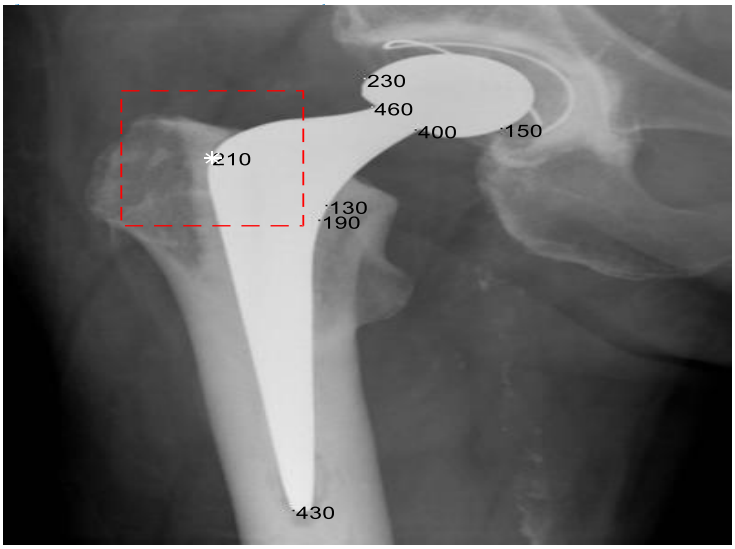

Figure 5. 14: Sample x-ray image without subsdience, ROI is highlight in red

A somewhat similar observation can be made when inspecting the gradient value changes illustrated in figure 5.15 that shows the gradient plot of pixels within the ROI of the THR image of figure 5.16. It is noted that in this specific case the pixel gradient value starts increasing immediately after the key-point. However the key-point seems to be well embedded within a solidly bonded area. Therefore it can be argued that this THR image does not indicate the presence of subsidence.

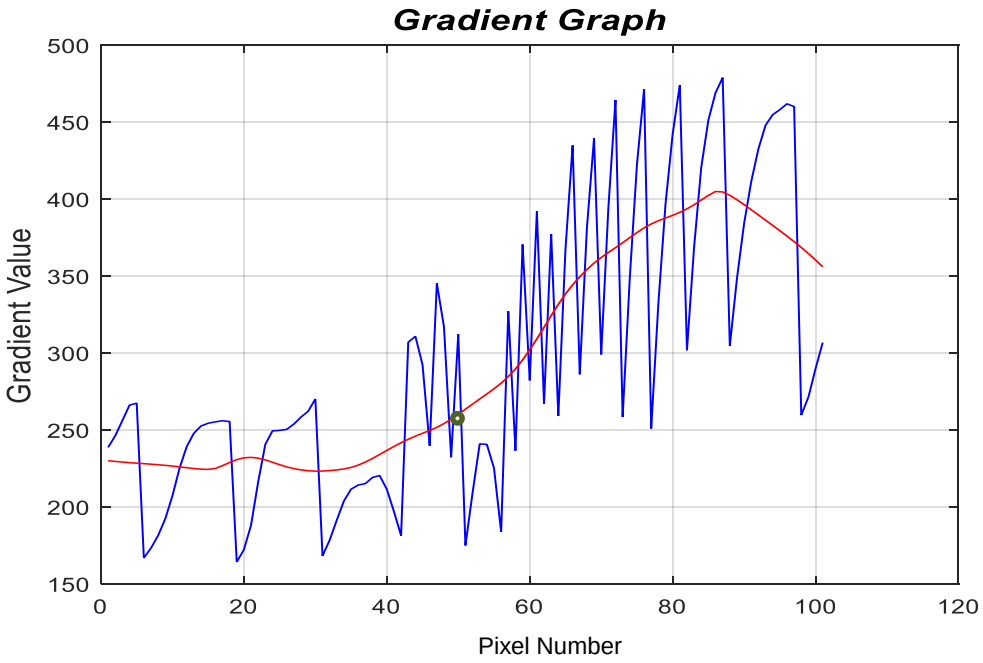

Figure 5. 15: Gradient of ROI of figure 5.16

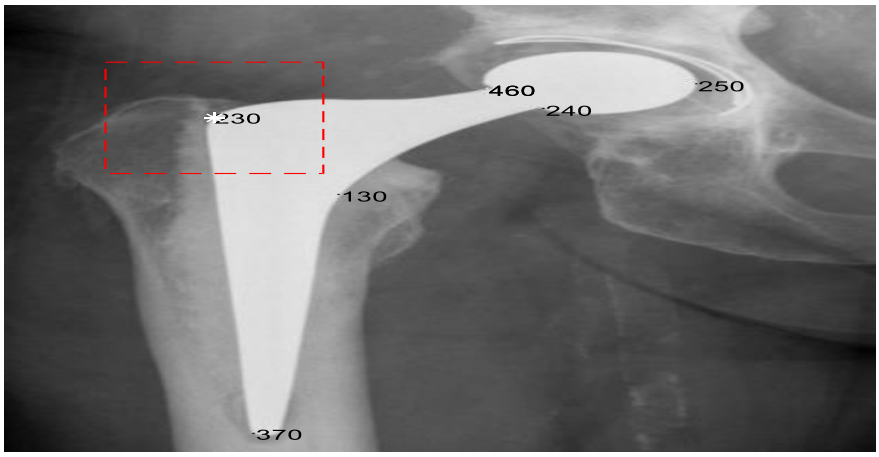

Figure 5. 16: Sample x-ray image without subsdience, ROI is highlight in red

A further example is illustrated by figure 5.17 which is the gradient plot of pixels within the ROI of the THR image illustrated in figure 5.18. This THR image also does not indicate the presence of subsidence.

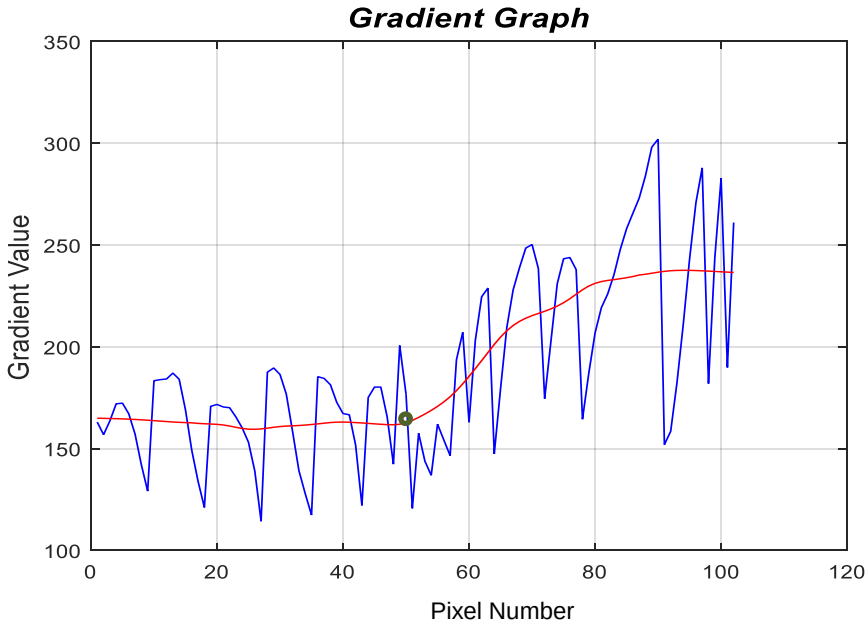

Figure 5. 17: Gradient of ROI of figure 5. 18

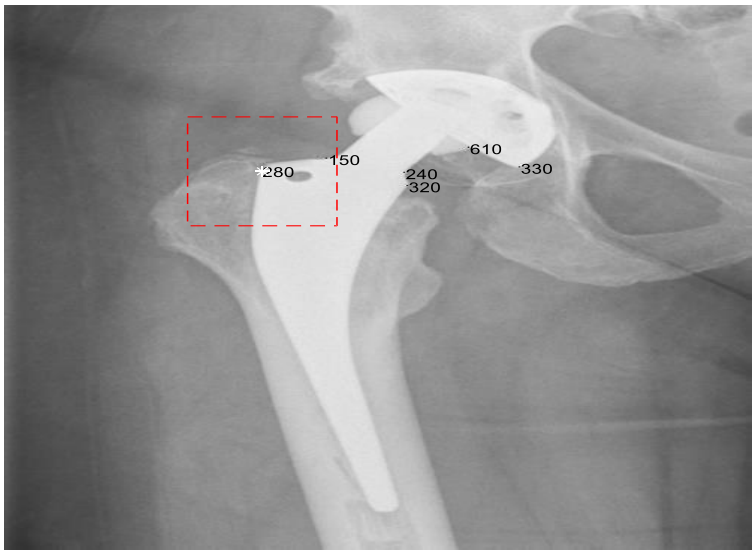

Figure 5. 18: Sample x-ray image without subsdience, ROI is highlight in red

The above experiments indicates that by studying the pixel value gradient across the prosthesis boundary of pixels within an ROI that centres the key-point can lead us to an approach that can effectively be used to determine the presence of subsidence. If on either side of the key-point, there are pixels of higher gradient value, this means that the on both sides of the keypoint there is either the bone shaft or broken cement bonds. The key-point is thus not secured and there is every chance that subsidence is present as in an ideal THR surgical procedure the key-point will well be fully embedded within a securely bonded area to both sides on the key-point, as illustrated when analyzing THR images with no evidence of subsidence.

Further experimental results for a number of other THR images showing the presence or absence of subsidence is presented in Appendix-B. The results are in comparison with the results presented above, leading to consistent justifications.

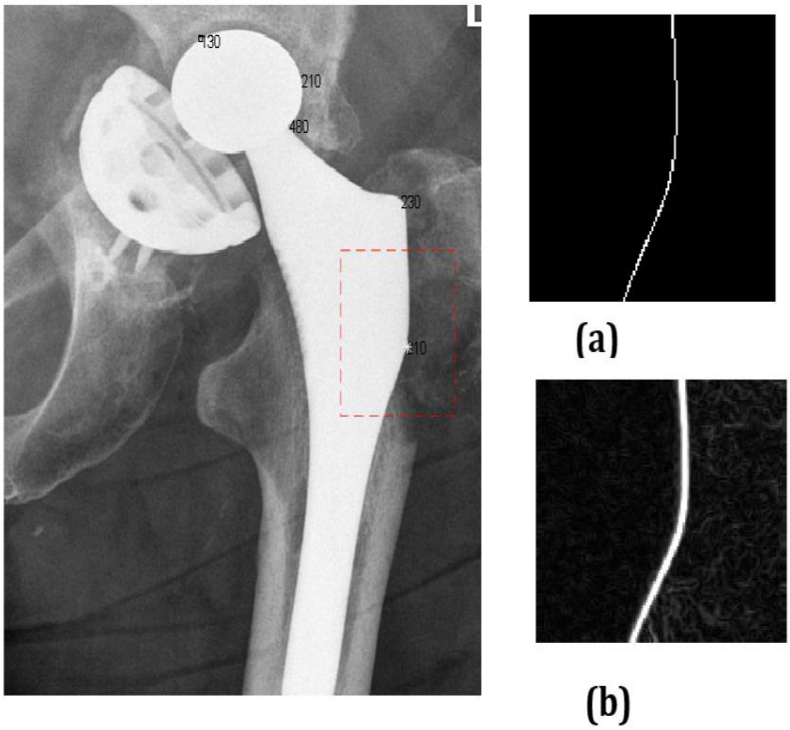

Figure 5. 19: A false corner detected; (a) and (b) shows the segmented ROI

Figure 5.19, illustrates a prosthesis with a rare shape where a wrong corner point is detected due to the presence of two corner points. The odd shape of the prosthesis has resulted in the above. Since the algorithms implemented picks up the first corner point that appears when traversing from the tip of the prosthesis stem, the wrong point was identified. In situations like this the algorithms needs to be modified to find the corner point with the highest curvature. If this was done, the correct point would have been picked up as the key-point. As such an irregular shape of prosthesis is rare, the algorithm presented initially will be valied for most prosthesis shapes.

5. 4 Conclusion

In this chapter we proposed a novel approach to automatically detect subsidence in THR x-ray images. A smoothed prosthetic edge contour is extracted followed by edge parametrization and corner detection. Based on this information we define the interest point on convex part of the prosthesis edge and a region of interest is segmented for further analysis. It was shown that by studying the gradient variations within prosthesis edge pixels within the ROI it is possible to detect the presence of subsidence. If the key-point is well embedded within a region of constant low gradient, this indicates a solid bonding of the prosthesis to the bone, hence no subsidence.

Chapter 6.

Detection of THR Infection in Radiographs

6. 1 Introduction

Infections after THR surgery occurs in a small percentage of patients that may lead to the need of prolonged antibiotics therapy or the ultimate removal of prosthesis. Studies [8],[9] and [10] show that relaying on pure eye observation of medical expert to detect infection can be challenging and inaccurate in some cases. Using computer aided diagnosis solutions improves medical expert's interpretation and may reduce number of errors. This chapter aims to introduce a simple coherent approach that identifies the presence of infection in THR x-ray images. The proposed method scans a THR image in cross sections and mark suspicious regions via calculating local maxima and local minima of the absolute pixel value gradient magnitude.

For clarity of presentation this chapter is divided into several subsections. Section 6.2, introduces the proposed technique to identify infection from THR x-ray images. Section 6.3, describes the methods used to enhance THR x-ray image appearance prior to processing for infection detection. Details of calculation of pixel value gradient magnitude across cross sections is explained in section 6.4; followed by section 6.5 of results, analysis and discussion. The chapter ends with a conclusion in section 6.7.

6. 2 Proposed Technique

In x-ray images of bones have a high x-ray attenuation compared to the surrounding tissues that have different gray level intensity values. A grey level of a pixel is described in the context of visual spatial distribution of pixel value over a relatively small area. One of the discriminative properties of infection in THR x-ray images is their grey level values of pixels around the prosthetic, which are significantly different from those within the prosthetic, cement bond (if used) or the bones. This information can be analyzed and extracted via calculating the gradient magnitude of pixel values across the edges of the prosthesis. It is noted that in general "the points that have local maxima in gradient values are considered edge points" [69].

When conducting the proposed research, x-ray images of patients who suffer from infection in THR were examined with the expert opinion of medical specialists before conducting any experiment to ensure correctness of the proposed concept, as well as defining the suspicious region in x-ray images for investigation. Pre-processing steps were carried out to segment and enhance these images prior to computing the absolute gradient magnitudes.

Figure 6.1 provides an overview of the proposed technique to identify infection from THR x-ray images.

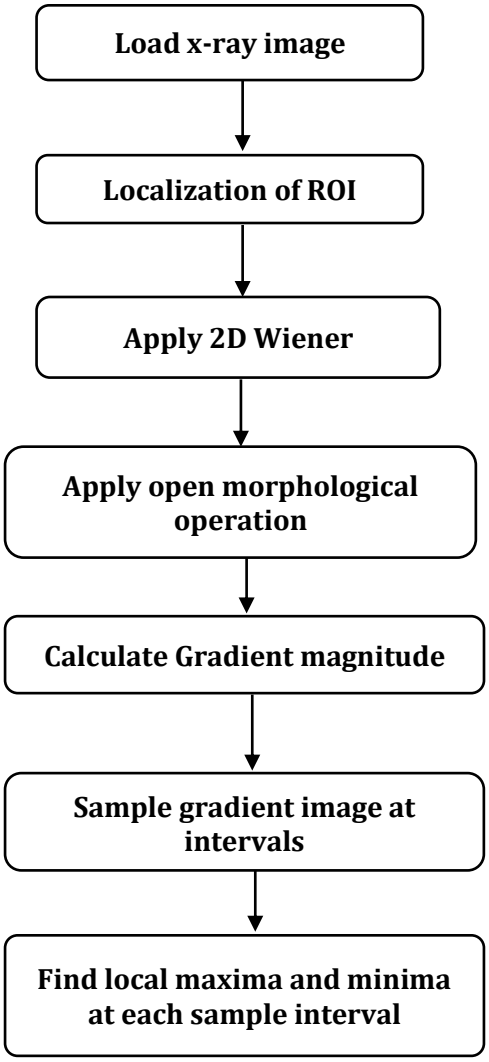

Figure 6.1: Proposed technique to detect infection in THR x-rays

The main idea that is being proposed is to take each cross section of the segmented THR image that centers the prosthesis region and across each cross section calculate the gradient values at each pixels. In the presence of a solid bond between the prosthesis and the cement / bonding material or the bone, the gradient value change pattern across the cross section will be different to what can be observed in the presence of an infection. The reason being the infected regions

being significantly darker than any other pixel belonging to the prosthesis, bonding material or the bone. It is also noted that one needs to discriminate the infections from loosency as loosency can also demonstrate similar trends in the gradient values across a cross section. However the two cases are distinguishable as loosency regions tends to be longer and have a linear boundary whereas the infection regions are relatively shorter and mostly present closer to the tip of the stem of the prosthesis having irregular boundaries.

6. 3 Image Enhancement

Medical images suffer from a wide variety of imperfections that may cause interpreting the abnormalities due to THR complications in x-ray images more complex. Therefore, we propose to improve the appearance of THR x-ray images by using a winner filter to reduce noise and an open morphological operation that sharpens faint but important details of x-ray images.

For the purpose of this research we use 22 THR x-ray images manually annotated and diagnosed by medical experts. An imperfection is defined around the bottom edge of the prosthesis in particular, between the cement/bone and prosthesis surface that appears as a dark region as shown in figure 6.2. Thus, first we localize ROI by cropping all test THR images as shown in figure 6.2. The reason of localizing this region only is due to various intensity levels in other unwanted regions that may mislead infection identification process if the whole hip bone has been delineated thereby end up with similar magnitude values or patterns. Two-dimensional Wiener filter is employed to remove noise and enhance the anatomical visualization. The Wiener filter degrades greyness by the constant power of additive Gaussian noise [40]. Then a low-pass filter is used to determine the least square mean and the variance around each pixel. This suppresses the inversion of

noise. A blurring filter is subsequently used for scaling it down using statistics from neighboring pixels. Logically, it cannot use a pure pixel basis, because there is no separation of signal and noise in each pixel. However, it decomposes the image into a smoothed background image and then takes deviations from this by estimating signal power plus noise power. The output of the filter is shown in figure 6.2(b).

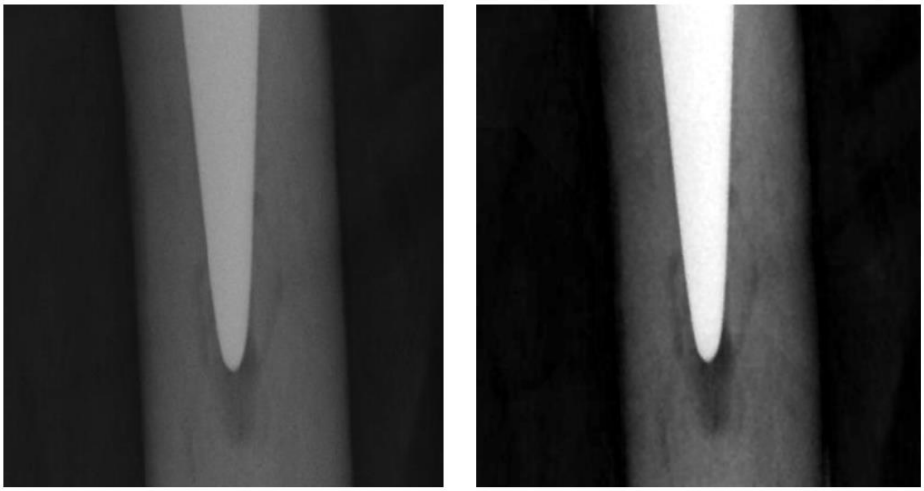

(a) **(b)**

Figure 6. 2: (a) ROI of THR Image & (b) filtered ROI

Since we want to compute the pixel value gradient magnitudes on an images that consists of noise, a morphological operation was further applied to reduce the structuring element of the noise present. In morphology, objects in an image are considered as sets of points that have special structuring elements (SE). Obviously, SEs play an important role in extracting the features or objects of a given shape in an image. This step refines the filtered image without changing the image intensity. It aims to eliminate irrelevant details that may add extra difficulties in outlining the boundaries of the prosthesis and the surrounding area. Thus, the open

morphological technique used performed grey level erosion process, followed by a grey level dilation process, by applying the same structuring pixels for both operations. This removes small objects from the images while preserving the shape and size of larger objects in the images. Further it opens up dark gaps between bright features in x-ray images whereas it clearly demonstrates the variation of color of the prosthetic and the surrounding area.

6. 4 Gradient Magnitude

The image gradient is defined as a directional change in intensity or color of an image. Sobel operator [42] manipulates image intensity to obtain the gradient features that assist to determine and separate objects from the background of an image. We choose Sobel operator to compute the gradient magnitude because it detects the edges where the gradient magnitude is high, with low computational cost. The gradient has a direction and a magnitude, this information is encoded in a vector. The gradient may be different at every point in an image. Therefore it is presented with a different vector at every location in the image; calculating the length of this vector provides the magnitude value, while its direction gives the gradient direction of that particular location in the image. Thus, if the gradient image is defined as a vector G= [Gx Gy], the absolute gradient magnitude at each point in an image can be computed by combining the gradient approximations, using:

$$G = \sqrt{Gx^2 + Gy^2} \tag{6.1}$$

Edges are demarcated clearly by the large gradient magnitudes that determine the boundary of the prosthetic and the bone, as shown in (Figure6.3), where the surrounding region has a lower gradient magnitudes.

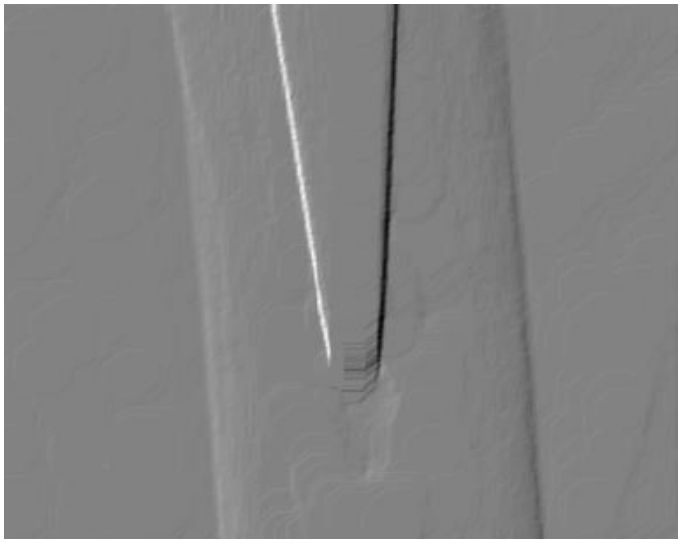

Figure 6. 3: An image shows gradient magnitude of figure 6.2(b)

However, it is difficult to synthesize any assumptions about gradient magnitude variations from the gradient image illustrated in figure 6.3. In-order to visualize intrinsic variance of the changing gradient magnitude values the output gradient image is sampled by taking image cross sections and plotted as a graph, where it used to validate the gradient magnitude at each point within target region described in detail in the section 6.5. This avail in assessing the changes of gradient magnitude values at each adjacent pixel or regions in the THR image.

6. 5 Results and Discussion

The proposed technique discussed above was tested on various THR x-ray images. To provide a vigorous evaluation of tested results a comparison was conducted between normal and abnormal THR x-ray images. Comparison in such cases aids in ensuring the effectiveness of the proposed method with limited THR x-ray images that were available for this research. Each image were sampled, i.e. cross sectioned, at equal intervals. To have a proper verification of results, let us first observe the test images illustrated in figure 6.4 (a) and (b). Here the images were purposely scaled to envisage the axes as x-axis and y-axis.

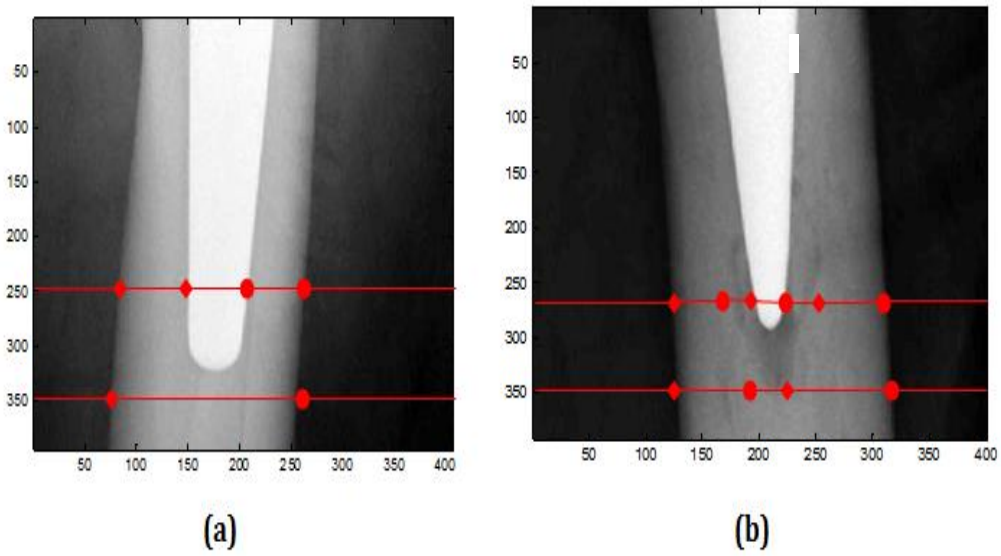

Figure 6. 4: Detecting local maxima and minima in (a) normal THR x-ray image (b) infected THR x-ray image

The reason for showing scale is to sight the target region and the sampled intervals as well as to deliberate the similarities and differences between compared images that may provide a sign of suspicious region in the THR image. The gradient magnitude is “sampled” at equal intervals across the target region in the gradient

image. As shown in (Figure6.4), the "sampled" intervals are carried between lines 250 and 350. For every line sampled, gradient values were plotted. The pixels along each line that exhibited the largest changes in gradient values are depicted as ♦ and • respectively. These values indicate the edges of the surrounding tissue, bone and the prosthesis and are referred to as local maxima and local minima. They are depicted as **(+)** and **(O)** respectively in figure 6.4. The graphs were slightly smoothed using a Gaussian filter as .05. The magnitude values can verify the correlation between the prosthetic and the surrounding region and as a fact is that edge pixels are at local maxima of gradient magnitude [69]; thus, defining those points is essential. To define periodic local maxima and local minima across the magnitude values a threshold of 0.5 and -0.5 were set respectively.

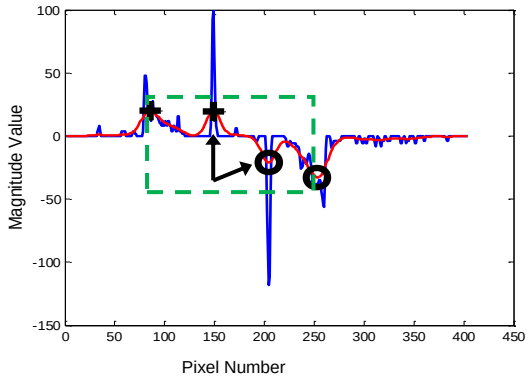

Graph 1: Magnitude at line 250

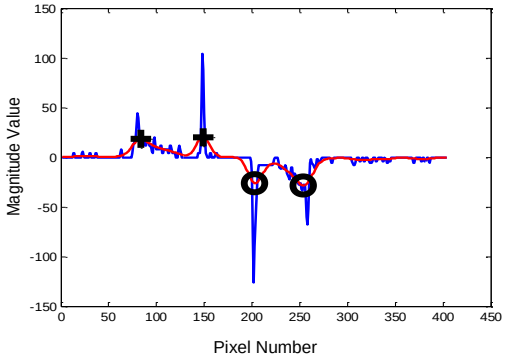

Graph 2: Magnitude at line 270

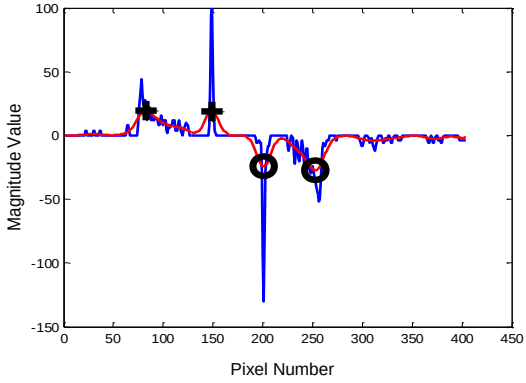

Graph 3: Magnitude at line 290

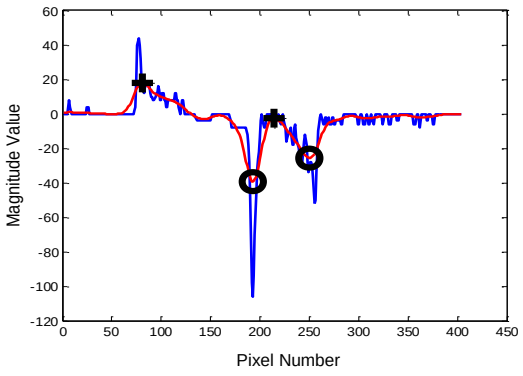

Graph 4: Magnitude at line 310

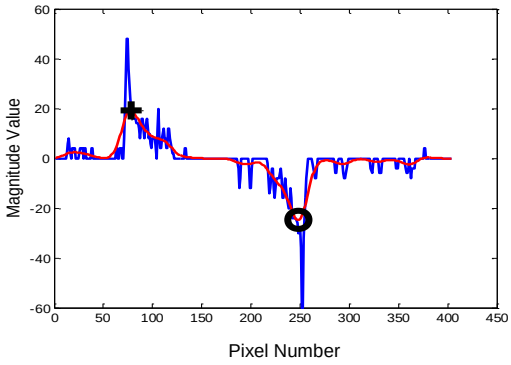

Graph 5: Magnitude at line 330

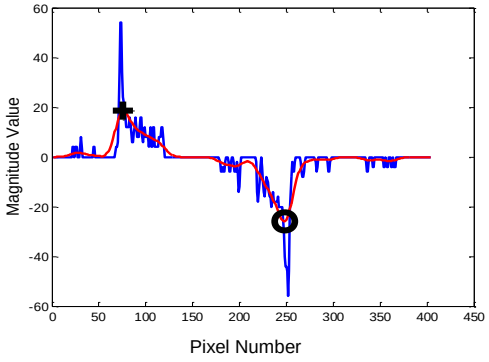

Graph 6: Magnitude at line 350

Figure 6.5: Gradient magnitudes obtained from a normal THR X-ray of figure 6.4 (a)

It should be noted that the gradient magnitude graphs in figure 6.5 correspond to the uninfected THR image in figure 6.4 (a). For instance, Graph 1 illustrates the gradient magnitude on line 250. The blue curve denotes the actual magnitude graph, which was smoothed using a Gaussian filter in order to have a better visualization of the magnitude values. This is represented as a red curve within the same graph.

Furthermore, the green highlighted area represents the **edges of the bone**, and the arrows represent the **edges of the prosthesis.** This has been defined as a target region to spot the gradient magnitudes behavior across these two edges. As can be seen in Graphs 1-4, there are two local maxima and two local minima. However, moving towards the bottom of the image, in a normal THR x-ray image, there is only one local maxima and one local minima, which correspond to the edges of the bone. This fact can be corroborated by looking at sample line **330 and 350** in figure 6.4 (a) that demonstrated **in Graphs 5 and 6**. The gradient magnitude graphs for the infected THR x-ray image of figure 6.4 (b) are depicted in figure 6.6. It is clear that, unlike the graphs for the normal THR images, there exists an alternation between local maxima and minima within the region of prosthetic edges.

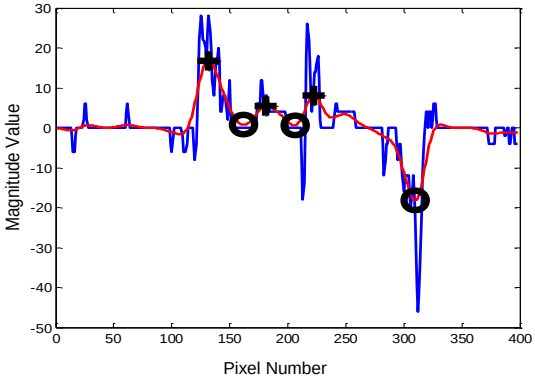

Graph 1: Magnitude at line 250

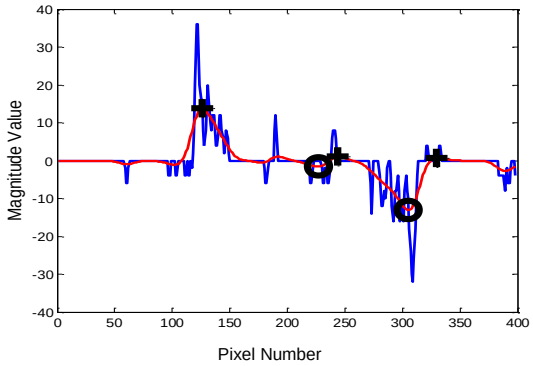

Graph 2: Magnitude at line 270

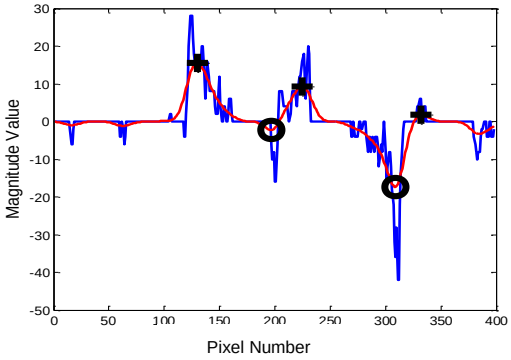

Graph 4: Magnitude at line 310

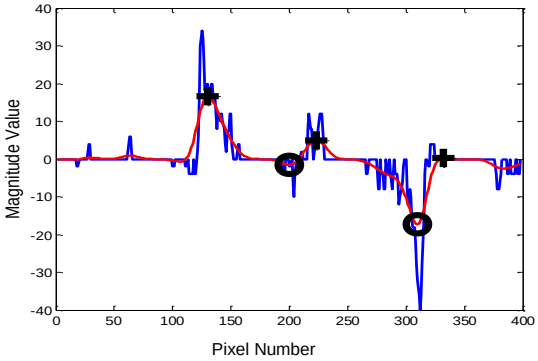

Graph 3: Magnitude at line 290

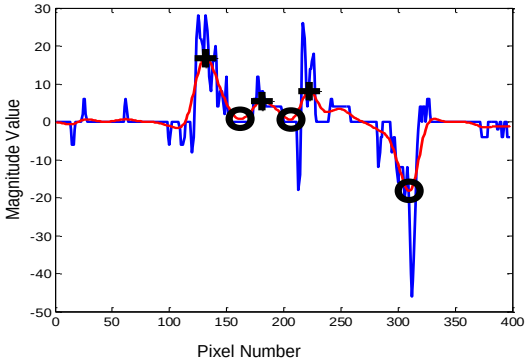

Graph 5: Magnitude at line 330

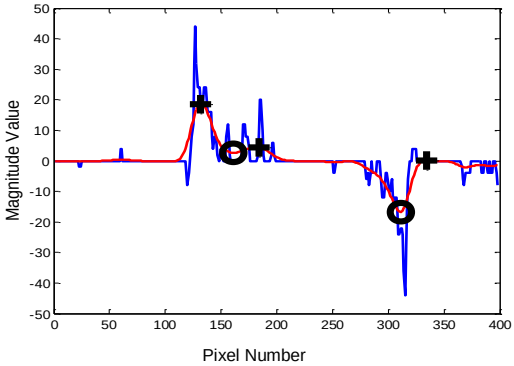

Graph 6: Magnitude at line 350

Figure 6. 6: Gradient magnitudes obtained from an infected THR X-ray figure 6.4 (b)

By observing the same region of the bone and the prosthesis in figure 6.6, the total number of peaks of both maxima and minima is usually more than four; while the case for a normal THR image is two local maxima and two local minima. Such an occurrence can be observed in all graphs. Similar anticipation of gradient magnitude is noted in figure 6.8 that represents another sample of normal THR x-ray image in figure 6.7 (a).

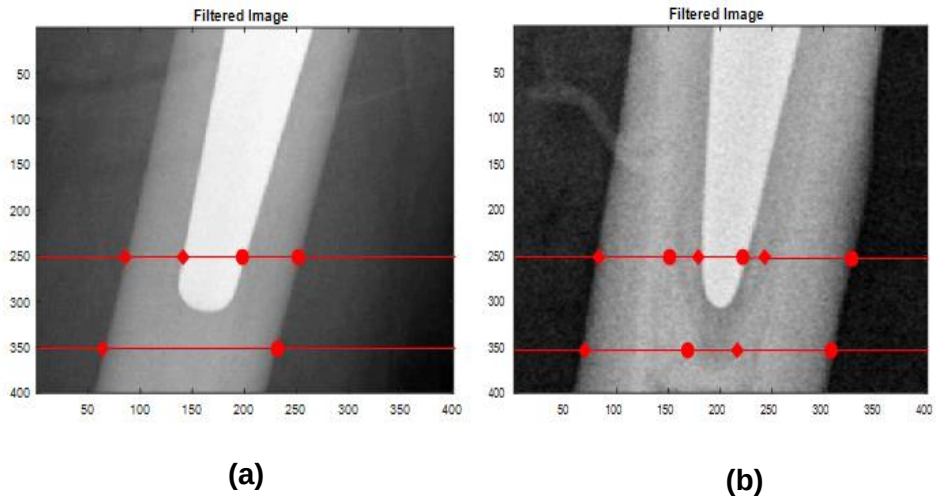

Figure 6. 7: Detecting local maxima and minima in (a) normal THR x-ray image (b) infected THR x-ray image

It should be clear that calculation of gradient magnitude is performed exactly the same as in figure 6.5 & figure 6.6. Likewise, the sampled intervals are performed between lines 250 and 350.

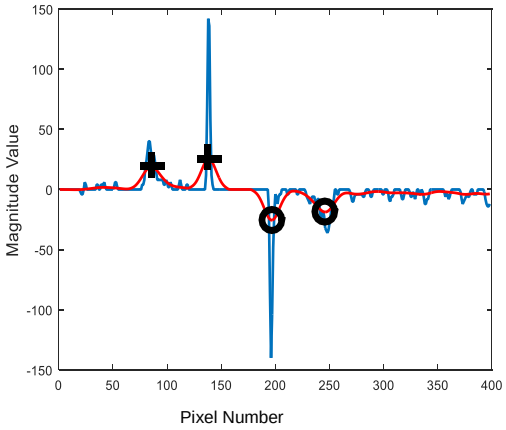

Graph 1: Magnitude at line 250

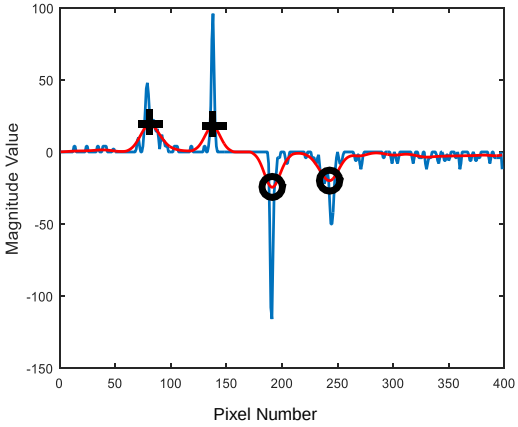

Graph 2: Magnitude at line 270

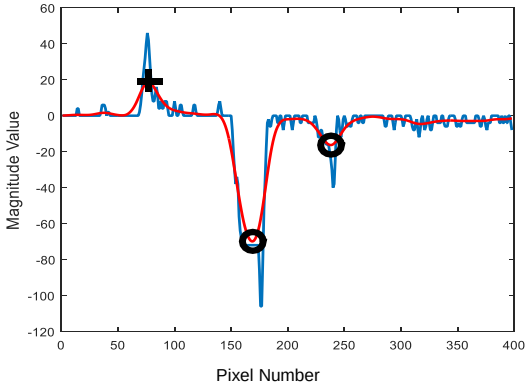

Graph 4: Magnitude at line 310

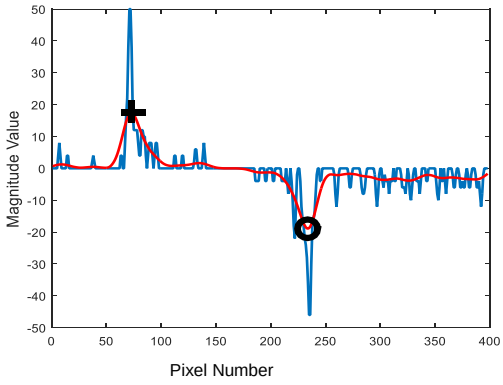

Graph 3: Magnitude at line 290

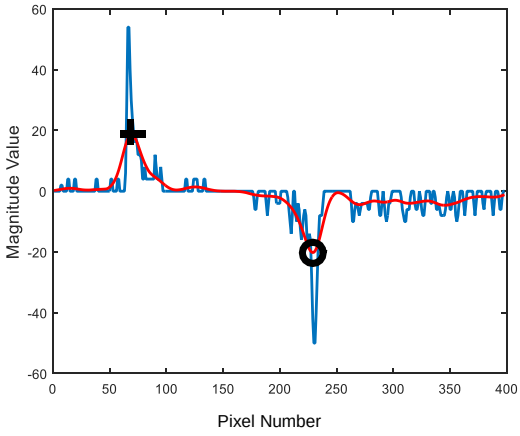

Graph 5: Magnitude at line 330

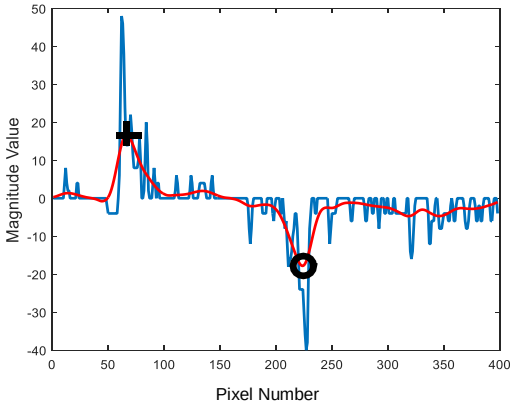

Graph 6: Magnitude at line 350

Figure 6. 8: Gradient magnitudes of figure 6.7(a)

As shown from graph 1 and 2, that there are two local maxima and two local minima that affirm the edges of the bone and the edges of the prosthetic as described for a normal case of THR image. Conversely, there is only one local maxima and one local minima which correspond edges of the bone as exemplified earlier about bottom of a THR image that is can be seen at sample line at **310 - 350** of figure 6.6 from **graphs 4 – 6**. Considering the fact of alternation between local maxima and local minima within the region of prosthetic edges is clearly visible in figure 6.9 that conform infected THR image in figure 6. 7 (b).

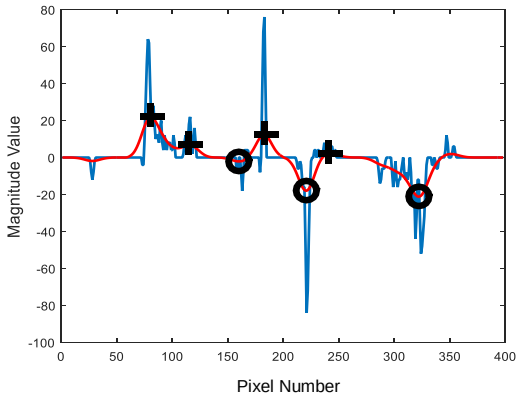

Graph 1: Magnitude at line 250

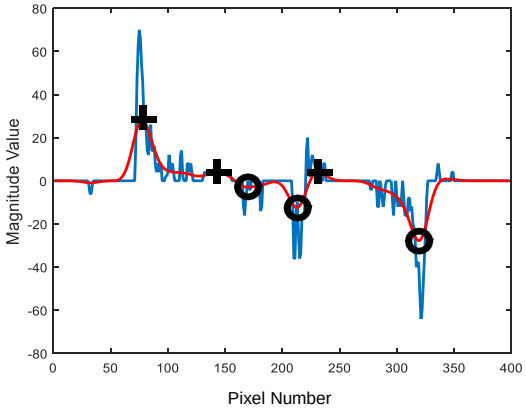

Graph 2: Magnitude at line 270

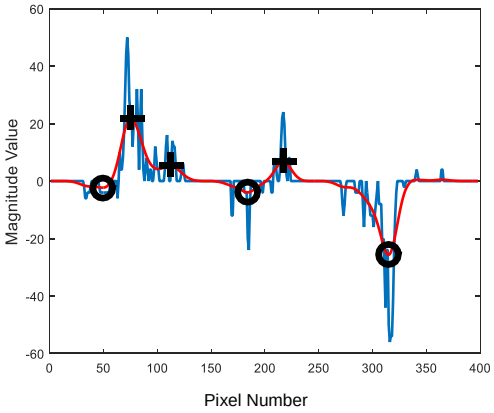

Graph 3: Magnitude at line 290

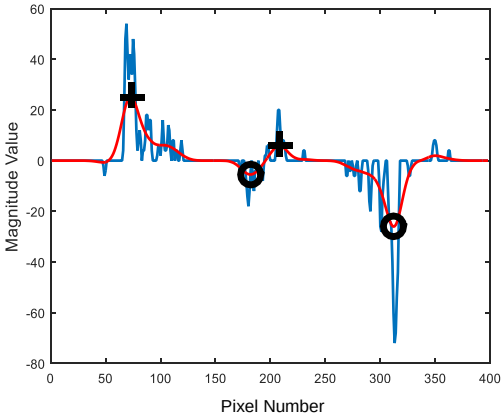

Graph 4: Magnitude at line 310

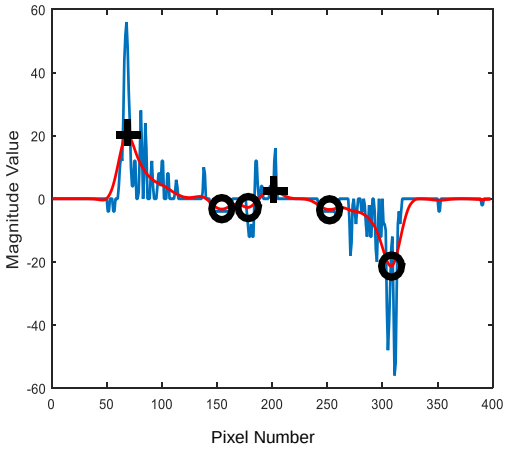

Graph 5: Magnitude at line 330

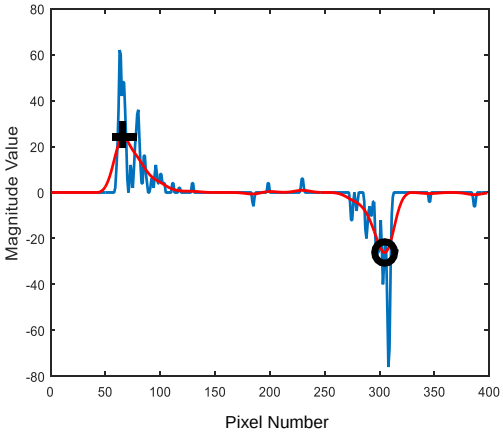

Graph 6: Magnitude at line 350

Figure 6. 9: Gradient magnitudes of figure 6.7 (b)

To provide an evident clarification of gradient magnitude behavior across sample intervals; this approach was tested on another normal and abnormal THR image. Similarly, the sampled gradient magnitudes were evaluated across the target region from line **250 - 350** as in figure 6.11, that conform to a normal THR image in figure 6.10 (e).

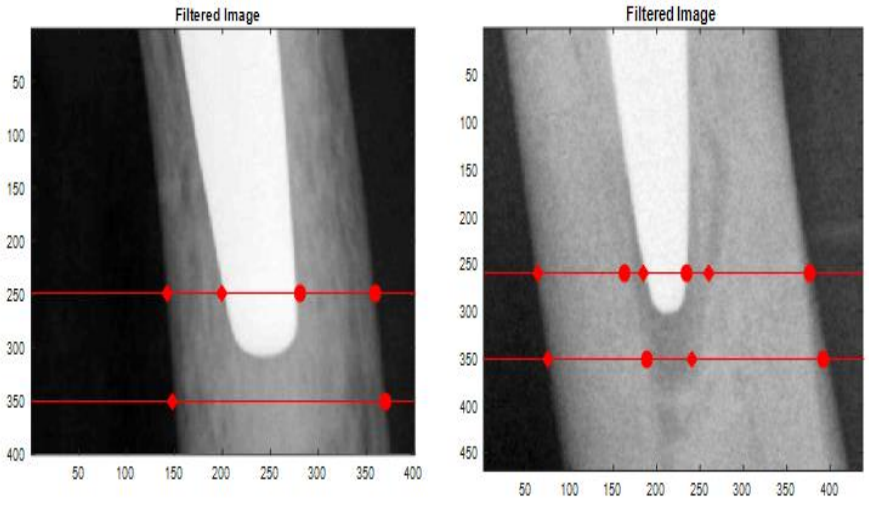

Figure 6. 10: Detecting local maxima and minima in (a) normal THR x-ray image (b) infected THR x-ray image

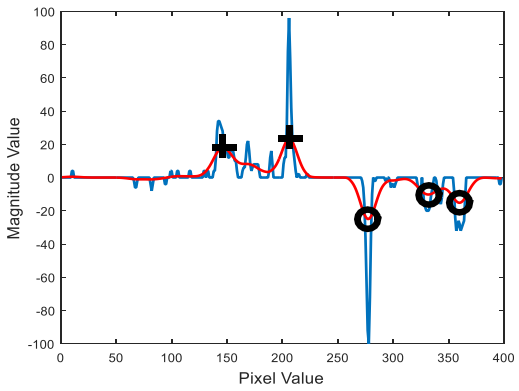

Graph 1: Magnitude at line 250

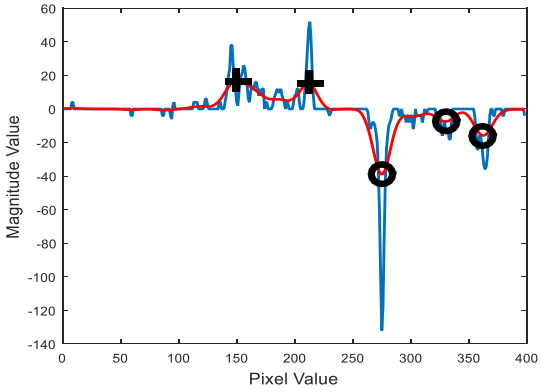

Graph 2: Magnitude at line 270

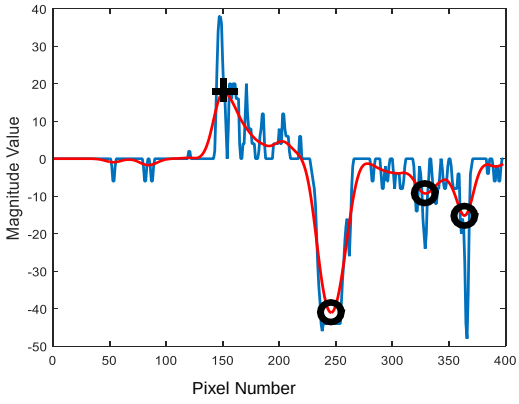

Graph 3: Magnitude at line 290

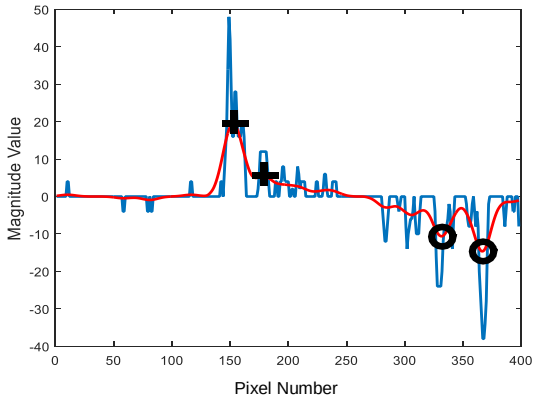

Graph 4: Magnitude at line 310

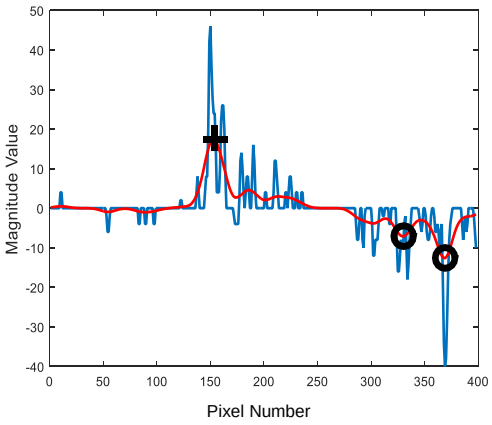

Graph 5: Magnitude at line 330

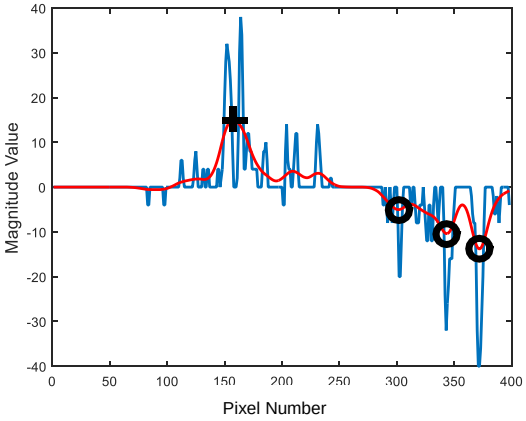

Graph 6: Magnitude at line 350

Figure 6. 11: Gradient magnitudes of figure 6.10 (a)

By looking at gradient magnitude of graph 1, that correspond line **250** in figure 6.10 (a); there are two local maxima that manifest the bone and the prosthetic edge for a normal THR image whereas three local minima however, the third local minima is out of the specified rang of defining the infected region in THR images. The **graph 4-6**, shows gradient magnitude of the bottom of THR image where it has to be one local maxima and one local minima that represents bone edge. As far for these graphs the number both local maxima and local minima varies

due the THR image illumination whereby this variation concur close to the bone edge that is again as stated earlier as a point out of the target region zone. On the other hand, looking at figure 6.11 that correspond infected THR image in figure 6.10 (b), both number local maxima and local minima exceed within target region. Merely, this clearly oppose the typical number of local maxima and local minima in a normal THR image. Yet, the only difference is in **graph 4** whereby, there is an local minima spotted before the start point of the bone edge as this is indicated as well out of the target region.

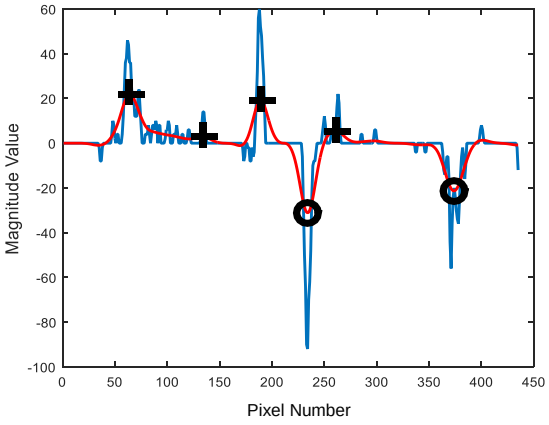

Graph 1: Magnitude at line 250

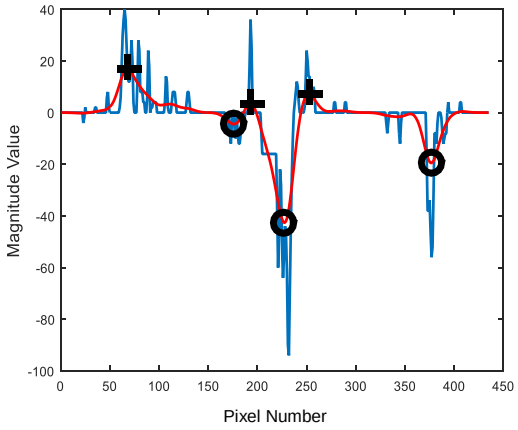

Graph 2: Magnitude at line 270

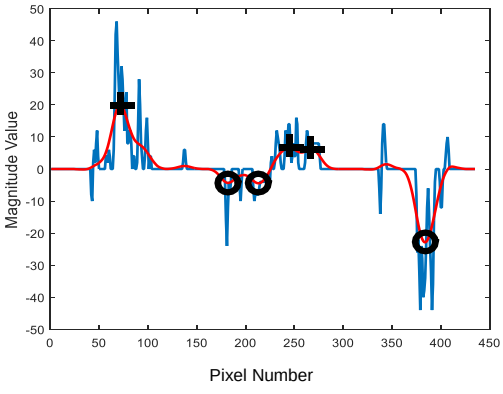

Graph 3: Magnitude at line 290

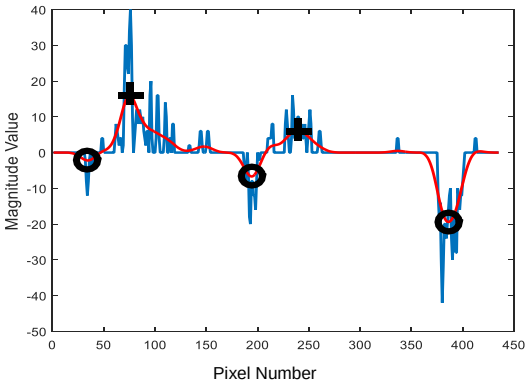

Graph 4: Magnitude at line 310

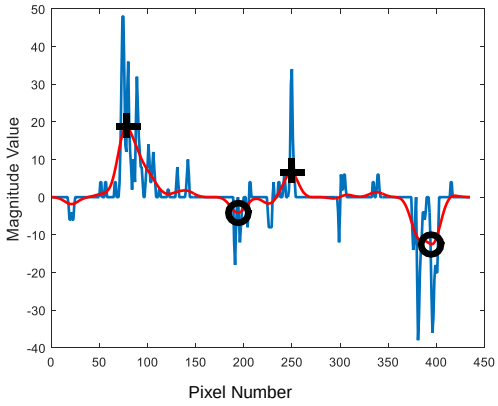

Graph 5: Magnitude at line 330

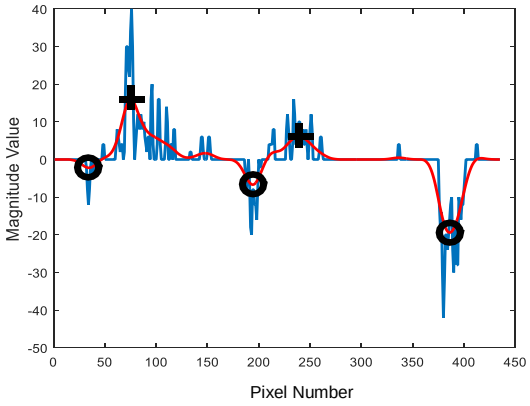

Graph 6: Magnitude at line 350

Figure 6. 12: Gradient magnitudes of figure 6.10 (b)

Despite the variation in gradient magnitude as noted in some of the graphs which is because of the x-ray image illumination; the commonalities of gradient magnitude values near the edge of the prosthesis ”target region” is clearly visible for both cases normal and infected THR x-rays. The rapid fluctuation of values near this region is a clear indication of an anomaly, most commonly an infection. Additionally, towards the bottom of the image as shown in figure 6.6, figure 6.9, figure 6.12 and more results are presented in appendix B, there are more than four peaks in an infected THR image, in contrast to the two found in a normal THR image. Thereby, all of these observations combined together serve as a powerful indicator for diagnosing the existence of infection within a THR x-ray image. This gives an obvious insight that gradient magnitude information, may use as an indicator to identify the fluctuations in intensity values close to the edge of the prosthesis, can in turn be used to identify the presence of infections within THR x-ray images. In addition, for calarification purpose sampling the entire cropped THR image automatically results in too many figures that have similar readings of gradient magnitudes. Since the number of the tested images is limited to 22, it was

adequate to illustrate the gradient magnitude along the target region as specified above in this section.

6. 6 Conclusion

This chapter proposed an automated technique to identify infection in THR x-ray images. Per-processing steps were carried on the THR x-ray images to enhance the appearance of the images and make certain details of closely adjacent regions in the image more evident. Gradient magnitude values of the target region were obtained and sampled at equal interval across this region. Number of existing local maxima and local minima were used as a feature for an indication if there is an anomaly in the tested THR x-ray image. A rapid alteration in number of local maxima and local minima within the target region in THR x-ray image is assumed a clear sign of infection. However, the proposed approach needs to be evaluated and that would be performed as a future work to support the accuracy and robustness of the technique on large set of THR data including any odd cases.

Chapter 7.

Conclusion and Future Work

The aim of the work carried out within the research context of this thesis was to design, implement and test computer vision based algorithms for the automatic detection of complications that can arise after THR surgical procedures. In achieving this aim an Active Contour Method (ACM) based approach was presented for the automatic extraction of the prosthesis. Subsequently a curvature measurement based approach was presented for the extraction of key-points on the boundary of the prosthesis contour, that are often used by medical experts as reference points in analysing THR images for the presence of complications. Subsequently pixel value gradient variation analysis based approaches were presented for the automatic detection of three main complications of THR surgical operations, namely, the presence of loosency, subsidence and infections. In addition to the above to help automate existing approaches for the detection of prosthesis misalignment, an ACM based approach was also presented for the automatic detection and segmentation of the Obturator Foramen, often used to provide reference points in quantifying misalignment.

Following sections provide the thesis conclusions and possible future work.

7. 1 Conclusion

A novel approach to extracting the prosthesis automatically was presented in chapter 3. In fact, two different approaches were implemented for the purpose of extracting prosthesis automatically. This chapter starts presenting the first approach which used histogram thresholding to extract prosthesis. Histogram thresholding generates a binary image wherein the foreground is separated from the background. It was shown that histogram thresholding has a drawback; it's accuracy significantly varied between different test THR images due to image quality, pixel value saturation and prosthesis location differences that are often present. It only produced accurate extractions on good quality images with very clear prosthesis boundaries. The second approach proposed was using active contour methods. The novelty of this approach is we automatically allocate the start points of this algorithm and based on these points it continues to deform the prosthesis contour until the contour reaches the prosthesis boundary. As we showed in chapter 3, as the prosthesis cup is circular in shape, we applied a circle detection algorithm to detect the prosthesis cup and locate its centre point automatically. By having this information, we determined the most right prosthesis cup edge pixels points. These parameters were passed to active contour method where it starts converging the prosthesis contour. We have demonstrated the ability of proposed approach in extracting the prosthesis of various different test THR x-ray images. Additionally, we extended the use of active contour method to segment obturator foramen. By segmenting obturator foramen; we can determine misalignment or leg discrepancy after total hip replacement. This this work was concluded to be useful in contributing towards the semi-automated approaches presented in literature for the detection of misalignment.

A novel algorithm was designed and implemented in chapter 4 to detect THR prosthesis loosening. With this approach, any dark region within radiolucent zone

or line at the prosthesis is detected via evaluating the gradient values at the prosthesis contour level. To allocate the radiolucent zones we defined straight and curved edge of the prosthesis contour by computing the curvature rate. Then the associated gradient values computed. We showed how the straight regions of radiolucent zone discriminate from the curved regions along with a demonstration of gradient pixels values of those regions. We showed the efficiency of this algorithm by comparing THR x-ray images with and without loosening as shown in the result and appendix-A. Another novel algorithm is presented in chapter 5 which automatically detect subsidence in THR x-ray images. After extracting the prosthesis edge, a key point is automatically detected on the convex of the prosthesis using corner detection that depends on computing curvature scale space. We showed how this approach is different from detecting loosening. As such the surrounded region of the key point is segmented to evaluate the consistency of grey scale pixels which is performed again by computing gradient pixel value. We showed that there is a clear pattern in the results with THR x-ray images with subsidence which is used to discriminate from THR x-ray images with no subsidence. Last but not least, a novel algorithm is presented in chapter 6 to detect THR infection. To detect the infection suspicious region within THR x-ray images is segmented; we showed that these region are surrounded the prosthesis particularly at the bottom edge. The segmented images are enhanced and the absolute gradient magnitude is computed at equal intervals across the images. We find local maxima and local minima of each interval. We showed that number of existing local maxima and local minima in normal THR image is limited to local edges within the image and we also showed in infected THR images that there is a variation in number of local maxima and local minima within the same THR image region; this an indication of an anomaly which is probably a sign of infection.

7. 2 Future Work

The ACM based approaches presented for the automatic segmentation of the prosthesis and the obturator foramen were proven to be very effective and help automate the subsequent THR complication detection algorithms presented both within this thesis and the methods proposed by other researchers. In order to ensure their universal effectiveness in extracting the relevant object areas, some fine tuning of the algorithms will have to be done depending on the shapes of the objects to be detected, noise levels of the images etc.

Further the algorithm proposed for the use in the detection of the circular area of the prosthesis can also be used to determine the circular plastic/steal cup that is often fixed to the thigh bone to hold the circular part of the prosthesis within. By detecting the centres of the two circles one will also be able to determine the presence of dislocations and even to quantify dislocation.

The algorithms presented to detect the presence of loosensy, subsidence and infections can be extended to quantify the relevant complication. For example once subsidence is detected in the THR images illustrated in figure 7.1 if the dark area around the subsidence region can be quantified via counting the dark pixels, this will provide a means for the quantification. Such additional knowledge of the measure of the complication can help medical specialists who may want to closely monitor escalation of the complication to determine when corrective surgery will have to be performed or to advise patients. Similarly approaches to quantifying loosency and infections can also be derived based on counting the dark pixels of the ROIs on normalised images.

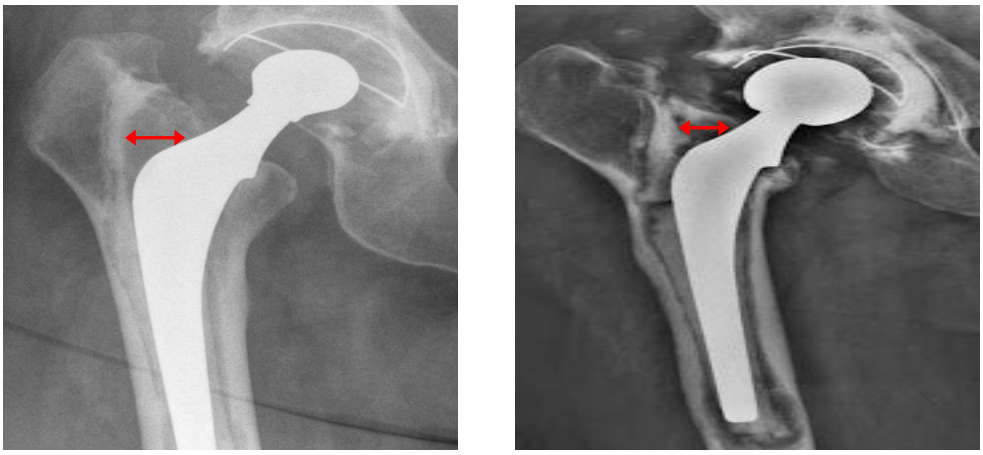

Figure7. 1: The distance between prosthesis and bone marked with red arrow

In the tested THR x-ray images within this thesis the infection is viewed at the bottom edge of prosthesis. However, the prosthesis is a bizarre object in the body; thus, infection can occur anywhere around the prosthesis, this work also can be extended to include the prosthesis cup region.

Another evident for measuring two common THR anomalies loosening and infection is measuring the bone density. With x-ray manifestation of bone; this two destructive lesions are surrounded by bright rim of density that represent prosthesis edge 'steel'. In term of measuring the density loosening seems as an extensive reaming that are deeper than the prosthesis edge creating a loosening rim around the prosthesis. Depending on the density of the bone the infection appears as punched holes surrounded the prosthesis that are darker then the bone and the prosthesis.

Loosening often results in the prosthesis having the freedom to move within the bone and with prolonged period of loosening due to the prosthesis 'hitting' the

wall of the bone at frequent intervals there could be evidence of 'bone thining' and 'bittleness'. Such severe cases of loosening can be identified by processing the bone and the pixel value variations within the bone close to the prosthesis.

It was mentioned that infections often is indicated by irregular edges. The proposed approach for the detection of infections can be extended to check whether the boundary is irregular. However for this purpose the image should be cross-sectioned at very close intervals that will need more processing power.

Further it is important for any research conducted within medical imaging field to present the false positive and false negatives of the approaches proposed for computer based image analysis. Due to the acute shortage of test images that were mainly due to patient confidentiality related issues, we were only able to test the algorithms on a relatively modest set of data. However as these datasets were selected by medical experts who were involved in the annotation of the complications and validation of our methods based on the small dataset, we are confident that the proposed approaches are a good proof of concept level idea. In the future with more data being available, the experiments could be extended. Such larger datasets will also allow validation and further analysis leading to possible further enhancement of the algorithms.

References

1. Hip replacement Definition , [Internet] available from
< http://orthocarefl.com/?page_id=744>, [Accessed on 26th of June 2017].
2. S. C. Mitchell, J. G. Bosch, B. P. F. Lelieveldt, R. J. van der Geest, J. H. C.Reiber, and M. Sonka. 3-D active appearance models: Segmentation of cardiac MR and ultrasound images. IEEE Trans. Med. Imag., 21(9):1167–1178, 2002.
3. Primary Total Hip Replacement: A Guide to Good Practice. British Orthopaedic Association Blue Book, First Published 1999, Revised August 2006, Nov 2012.
4. National Joint Registry, National Joint Registry for England and Wales: 8th Annual Report, Hemel Hempstead: NJR Centre, 2011, page 59.
5. National Joint Registry. Public and Patient Guide to the NJR'S 10th Annual Report 2013. England, Wales and North Ireland.
6. T. A. Gruen , G. M. McNeice , H. C. Amstutz , Modes of failure" of cemented stem-type femoral components: a radiographic analysis of loosening, Clin Orthop Relat Res. 1979 Jun;(141):17-27.
7. Possible Hip Replacement Surgery Complications, [Internet] available from
<http://evertsmith.com/treatment/hip-complications/>,
[Accessed on 28th of July 2015].
8. W. Zimmerli: Prosthetic device infections,In: Root RK, Waldvogel FA, Corey L, Stamm WE (eds.), Clinical infectious diseases: a practical approach, Oxford University Press 1999, pp 801–808.
9. W. Zimmerli, P.E. Ochsner, Management of infection associated with prosthetic joints, Infection, 2003 Mar, 31(2):99-108.
10. W. Zimmerli, Prosthetic device infections. In: Root RK, Waldvogel FA, Corey L, Stamm WE (eds.), Clinical infectious diseases: a practical approach, Oxford University Press 1999, pp 801–808.
11. D. A. Dennis, Dislocation Following Total Hip Arthroplasty, Revision Total Hip Arthroplasty pp 32-39.
12. Dislocation of a total hip arthroplasty: etiology and management, [Internet] available from<http://www.revmed.ch/rms/2009/RMS-230/Luxation-d-une-arthroplastie-totale- de-la-hanche-etiologie-et-prise-en-charge>, [Accessed on 28th of July 2015].

13. N. Otoum,E. A.Edirisindhe,Medical Image Processing: Applications in Ophthalmology and Total Hip Replacmcnet, Loughborough University, 2012.
14. M. Komeno, M.Hasegawa, A.Sudo, A. Uchida, Computed Tomographic Evaluation of Component Position on Dislocation After Total Hip Arthroplasty, Healio Orthopedics, Vol.29, No.12, Dec. 2006.
15. A.Oprea, C.Vertan: A Quantitative Evaluation of the Hip Prosthesis Segmentation Quality in X-ray Image, International Symposium in Signals, Circuits and Systems, ISSCS, vol.1,pp.1-4, Jul. 2007.
16. L. Florea and C. Vertan, Automatic Hip Prosthesis Fit Estimation by Cooperative X-ray Image Segmentation, U.P.B. Sci. Bull., Series C, Vol.71, No.4, 2009.
17. R. Smith and K. Najarian, Automated Segmentation of Pelvic Bone Structure in X-ray Radiographs Using Active Shape Models and Directed Hough Transform, Bioinformatics and Biomeidcine Workshops, IEEE International Conference, pp.56-63 , Nov. 2008.
18. T.M.Barker, W.J.Donnelly, Automated image analysis technique for measurement of femoral component subsidence in total hip joint replacement, Medical Engineering & Physics,Vol.25, No.2,pp.91–97, Mar 2003.
19. M. Downing, P. Undrill, P. Ashcroft, D. Hukins, and J. Hutchison, Automated femoral measurement in total hip replacement radiographs, International Conference on Image Processing and Its Applications, IEEE, July 1997.
20. K. Hardinge, M.L. Porter, P.R. Jones, D.W. Hukins, C.J. Taylor, Measurement of hip prosthesis using image analysis. The maxima hip technique, Wrightington Hospital and the University of Manchester, 1991.
21. S.Sahin , E.Akata, Image Analysis for Obturator Foramen Based on Marker-Controlled Watershed Segmentation and Zernike Moments, International Journal of Computer, Electrical, Automation, Control and Information Engineering Vol:9, No:10, 2015.
22. S.Kerrigan,S.McKenna,I.W.Ricketts,C.Wigderowitz, Analysis of Total Hip Replacements Using Active Ellipses, Division of Applied Computing, University of Dundee, Dundee, Scotland.
23. S. Kerrigan, S. McKenna, I.W. Ricketts, C. Wigderowitz, Eccentricity Error Correction for Automated Estimation of Polyethylene Wear after Total Hip Arthroplasty, University of Dundee, Dundee, Scotland.
24. S. Kerrigan, S. McKenna, I.W. Ricketts, C. Wigderowitz, Eccentric Elliptical Contours in Total Hip Replacements, University of Dundee, Dundee, Scotland.

25. A. Kaneuji, T. Sugimori, T. Ichiseki, K. Fukui, K. Yamada, T. Matsumoto, The relationship between stem subsidence and improvement in the radiolucency in polished tapered stem, Int. Orthop. 2006 Oct;30(5):387-90. Epub 2006 Apr 14.
26. J. R. Loudon, J. Charnley, Subsidence of the femoral prosthesis in total hip replacement in relation to the design of the stem, Victoria Infirmary, Glasgow and The Hip Centre, Wrightington Hospital, Wigan
27. T. O. Smith, T.H.D. Williams, A. Samuel, L. Ogonda, J.A. Wimhurst, Reliability of the radiological assessments of radiolucency and loosening in total hip arthroplasty using PACS, Hip Int., 2011; 21(5): 577 – 582.
28. S. N. Massoud, J. B. Hunter, B. J. Holdsworth, W. A. Wallace, R. Juliusson, Early femoral loosening in one design of cemented hip replacement, Harlow Wood Orthopaedic Hospital, Nottingham, England,1997.
29. P. S. Kinov, T. Z. Petrov , D. Vasileva , P.N. Tivchev, Comparison of Different Diagnostic Modalities in Evaluation of Infection of Total Hip Arthroplasty, Clinic of Orthopedics and Traumatology, Queen Giovanna University Hospital- ISUL, Medical University-Sofia, Bulgaria,2009.
30. H.Mulcahy , F.Chew , Current concepts of hip arthroplasty for radiologists: part 1, features and radiographic assessment, AJR Am J Roentgenol. 2012 Sep;199(3):559-69. doi: 10.2214/AJR.12.8843.
31. J.Vanrusselt, M.Vansevenant, G.Vanderschueren, F.Vanhoenacker, Postoperative radiograph of the hip arthroplasty: what the radiologist should know, Insights Imaging. 2015 Dec; 6(6): 591–600.
32. C. Ruther, U. Timm, H. Ewald, W. Mittelmeier, R. Bader, R. Schmelter, A. Lohrengel,D. Kluess, Current Possibilities for Detection of Loosening of Total Hip Replacements and How Intelligent Implants Could Improve Diagnostic Accuracy, Department of Orthopaedics, University of Rostock Germany.
33. E. R. Valstar, R.G.H.H.Nelissen ,J. H.C. Reiber, P. M. Rozing , The use of Roentgen stereophotogrammetry to study micromotion of orthopaedic implants Department of Orthopaedics, Leiden University Medical Center, P.O. Box 9600, 2300.
34. A.P Gergiou, J.L Cunningham, Accurate diagnosis of hip prosthesis loosening using a vibrational technique. e. Clinical Biomechanics, 16 (4), pp. 315-323.2001.
35. W.Kristanto, P. M. A. van Ooijen, B. The, H. Duifhuis, T. R. Mengko, M. Oudkerk, Design and Implementation of Gradient Vector Flow Snake to Detect a Reference Object in Pelvic X-rays for Preoperative Total Hip Arthroplasty Planning Application, J Digit Imaging. 2007 Dec; 20(4): 373–380.
36. S. Habib, O. Adnan, Nafees-ur-Rahman, Automated Detection of Infected Area in Lungs, International Conference on Emerging Technologies, 2009.

37. M.I.Sezan, A peak detection algorithm and its application to histogram-based image data reduction, Graphics Models and Image processing, 29,47~59,1985
38. Thresholding Tool, [Internet] available from
<http://uk.mathworks.com/MATLABcentral/fileexchange/6770-thresholding-tool>, [Accessed on 17th of July 2015].
39. 2-D adaptive noise-removal filtering, [Internet] available from
< http://www.mathworks.co.uk >,[Accessed on 12th August 2015].
40. F. Jin, P. Fieguth, L. Winger and E. Jernigan, Adaptive Wiener filtering of noisy images and image sequences, Department of Systems Design Engineering, University of Waterloo,2003.
41. Z. Wei, Y. Hua, S. Hui-sheng, F. Hong-qi, X-ray Image Enhancement Based on Multiscale Morphology,IEEE,1-4244-1120-3/07,2007.
42. Sobel operator, [Internet] available from
<http://en.wikipedia.org/wiki/Sobel_operator>, [Accessed on 14 of June 2015]
43. Q. Lin, Y. Han, H. Hahn, Real-time Lane Detection Based on Extended Edge-linking Algorithm, IEEE Computer Society,978-0-7695-4043-6/10 , 2010 , doi:10.1109/ICCRD.2010.166.
44. M. Kass, A. Witkin, D. Terzopoulos, Snakes: Active contour models, Internet J. Comput. Vision, 1 (4) (1987), pp. 321‑331.
45. W. Kristanto, P. M. A. van Ooijen, B. The, H. Duifhuis, T. R. Mengko, M. Oudkerk, Design and Implementation of Gradient Vector Flow Snake to Detect a Reference Object in Pelvic X-rays for Preoperative Total Hip Arthroplasty Planning Application, J Digit Imaging. 2007 Dec; 20(4): 373–380.
46. F.P. Ferrie, J. Lagarde, P. Whaite, Darboux frames, snakes, and super-quadrics: Geometry from the bottom up, IEEE Trans. Pattern Anal. Machine Intell. 15 (August 1993) 771‑784.
47. T. McInerney, D. Terzopoulos A dynamic finite element surface model for segmentation and tracking in multidimensional medical images with application to cardiac 4D image analysis Comput. Med. Imaging Graph, 19 (1) (1995), pp. 69‑83.
48. C. D. Terzopoulos, K.M. Harris, Computer-assisted registration, segmentation, and 3D reconstruction from images of neuronal tissue sections, IEEE Trans. Med. Imaging 13 (June 1994) 351‑362.
49. R. Durikovic, K. Kaneda, H. Yamashita, Dynamic contour: a texture approach and contour Operations Visual Comput., 11 (1995), pp. 277‑289.

50. F. Leymarie, M.D. Levine, Tracking deformable objects in the plane using an Active contour Model, IEEE Trans. Pattern Anal. Machine Intell., 15 (6) (1993), pp. 617‑634.
51. D.Terzopoulos, R.Szeliski, Tracking with Kalman snakes, A. Blake, A. Yuille (Eds.), Artificial Intelligence, MIT Press, Cambridge, MA (1992), pp. 3 – 20.
52. A.J. Abrantes, J.S. Marques, A class of constrained clustering algorithms for object boundary extraction, IEEE Trans. Image Process 5 (November 1996) 1507 – 1521.
53. C. Davatzikos, J.L. Prince, An active contour model for mapping the cortex, IEEE Trans. Med. Imaging 14 (March 1995) 65 – 80.
54. C.Xu, J.L. Prince, Gradient vector flow: A new external force for snakes, IEEE Proc. Conf. on Comput. Vis. Patt. Recog. (CVPR) 1997, pp. 66 – 71.
55. C.Xu, J. L. Prince, Snakes, shapes, and gradient vector flow, IEEE Trans. on Image Process. (March 1998) 359 – 369.
56. N.Mark, A. Alberto, Feature Extraction & Image Processing for Computer Vision, 2nd Edition, Academic Press 2008, ISBN: 0 7506 5078 8.
57. M.Awrangjeb, G.Lu, M.Murshed, An affine resilient curvature scale-space corner detector,1. I-1233 . 10.1109/ICASSP.2007.366137
58. L.Zou, J.Chen, J.Zhang & L.Dou, The Comparison of Two Typical Corner Detection Algorithms, Second International Symposium on Intelligent Information Technology Application, 2008.
59. Flood fill operation, [Internet] available from
<http://www.mathworks.com, [Accessed on 18th of July 2015].
60. Template Matching, [Internet] available from
<https://en.wikipedia.org/wiki/Template_matching>,[Accessed on 29 of September 2016]
61. L.Jia, C.Pen, H.Liu, Z.Wang, A Fast Randomized Circle Detection Algorithm, Proceedings-4th International Congress on Image and Signal Processing,2011.
62. O.R.Vincent, O.Folorunso, A Descriptive Algorithm for Sobel Image Edge Detection, Proceedings of Informing Science & IT Education Conference, pp. 97-107, 2009.
63. Y.Jiang , J.Meng , P.Babyn, X-ray image segmentation using active contour model with global constraints, Proceedings of CIISP 2007; 2007 June 4; Honolulu. Honolulu (HI): IEEE; 2007. p. 240-45.
64. M.E.Leventon, W.E.L.Grimson, O.Faugeras, Statistical shape influence in geodesic active contours, Proceedings from IEEE Conference on Computer Vision and Pattern Recognition, (2000) 316-323.

65. S. Lankton and A. Tannenbaum. Localizing Region-Based Active Contours. IEEE Transactions on Image Processing, 17(11):1, 2008
66. S.Chopra,K. Marfurt,Volumetric curvature attributes for fault/fracture characterization, First Break. 25. 10.3997/1365-2397.2007019.
67. Solomon, C.; Breckon, T. Fundamentals of Digital Image Processing,1st Edition Wiley-Blackwell: Hoboken, NJ, USA, 2011.
68. Image Gradient, [Internet] available from
<https://en.wikipedia.org/wiki/Image_gradient>,[Accessed on 25th of October 2016].
69. A. C. Bovik, The Essential Guide To Image Processing, 2nd Edition,Academic Press, Boston, Mass, USA, 2009,ISBN:0123744571 9780123744579.
70. Histogram Equalization, [Internet] available from
<https://en.wikipedia.org/wiki/Histogram_equalization>, [Accessed on 17th of October 2016].
71. J .Karrholm, W. Frech,B. Nivbrant, H.Malchau,F. Snorrason, P. Herberts (1998) Fixation and metal release from the Tifit femoral stem prosthesis. 5-year follow-up of 64 cases. Acta Orthop Scand 69(4):369–378.
72. J. K¨arrholm, B. Borss´en, G. L¨owenhielm, F. Snorrason, Does early micromotions of femoral stem prostheses matter? 4-7-year stereoradiographic follow-up of 84 cemented hip prostheses, J Bone Joint Surg [Br] 1994;76-B:912-7.
73. Kroell A, Beaule P, Krismer M, Behensky H, Stoeckl B, Biedermann R (2008) Aseptic stem loosening in primary THA: migration analysis of cemented and cementless fixation. Int Orthop. doi:10.1007/s00264-008-0701-1.
74. S.Breusch, H. Malchau, The Well-Cemented Total Hip Arthroplasty: Theory and Practice,Springer Science & Business Media, 8 Feb 2006.
75. L. V. Gool, T. Moons and D. Ungureanu, Affine/photometric invariants for planar intensity patterns, in Proc. European Conference on Computer Vision, vol.LNCS 1064, no. 1, pp. 642–651, Cambridge, UK, April 1996.
76. L.Kitchen,A.Rosenfeld,Grey-level corner detection, Pattern RecognitionLetters, vol. 1, pp. 95–102, December 1982.
77. A.Rosenfeld,E. Johnston, Angle detection on digital planar curves, IEEETrans. on Computers, vol. C-22, pp. 875–878, September 1973.
78. A.Rosenfeld and J.Weszka, An Improved Method of Angle Detection on Digital Curves, IEEE Trans. on Computers, vol. C-24, pp. 940–941, September 1975.
79. F.Mokhtarian,R. Suomela, Robust image corner detection through curvaturescale space, IEEE Trans. on Pattern Analysis and Machine Intelligence, vol. 20,no. 12, pp. 1376–1381, December 1998.

80. M. Awrangjeb, Guojun Lu, and M. Murshed, An Affine Resilient Curvature Scale-Space Corner Detector, in Proc. International Conference on Acoustics, Speech,and Signal Processing (ICASSP 2007), vol. 1, pp. 1233–1236, Hawaii, USA, 15-20 Apr. 2007.
81. Morrey B, Difficult complications after hip joint replacement,Clin Orthop Relat Res. 344: 179–187, 1997.

Appendix A.

A sample THR x-ray image with loosening

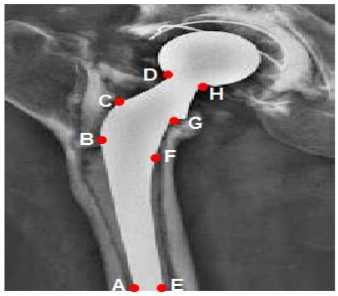

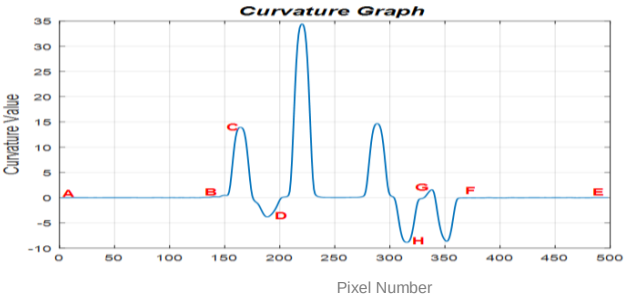

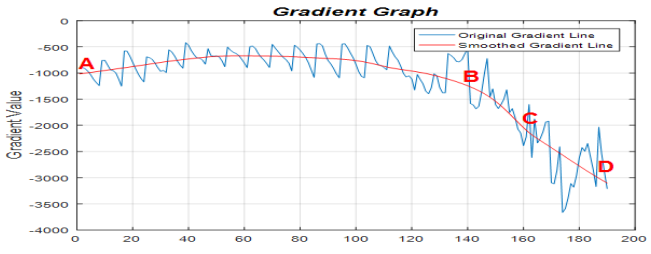

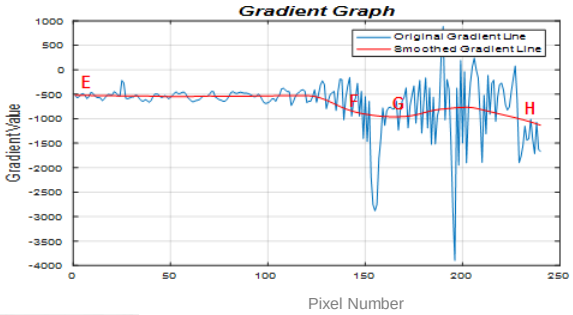

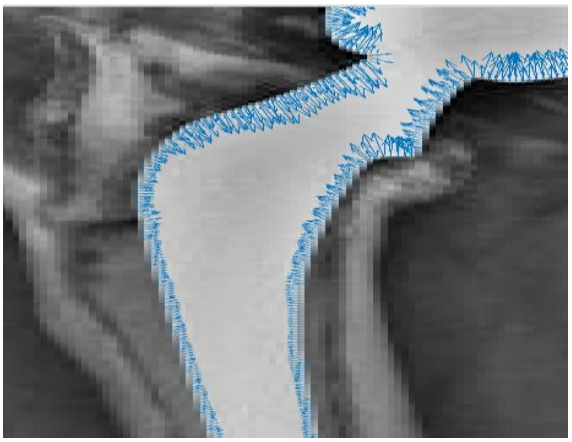

A sample THR x-ray image without loosening-1

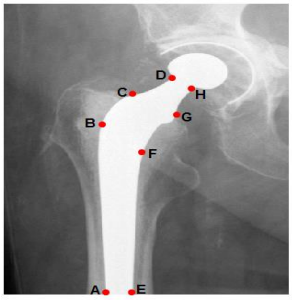

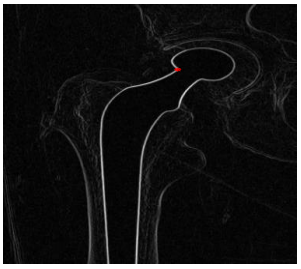

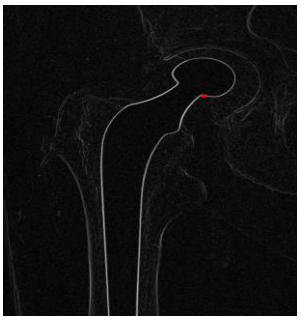

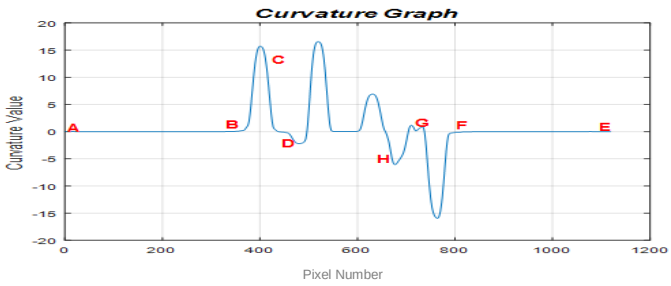

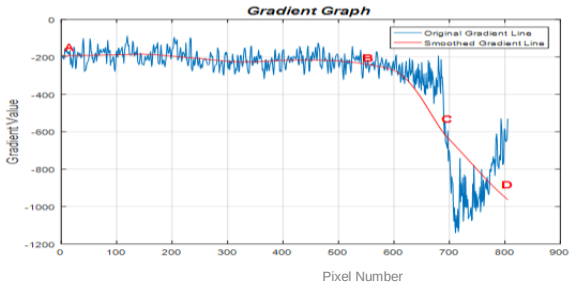

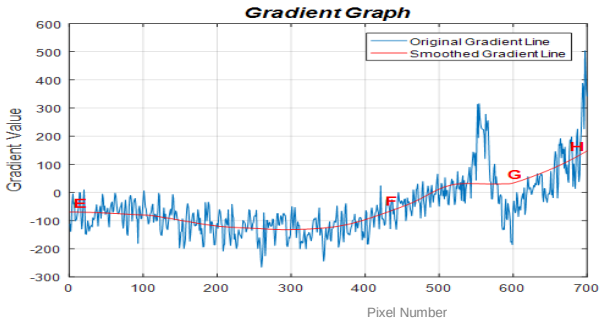

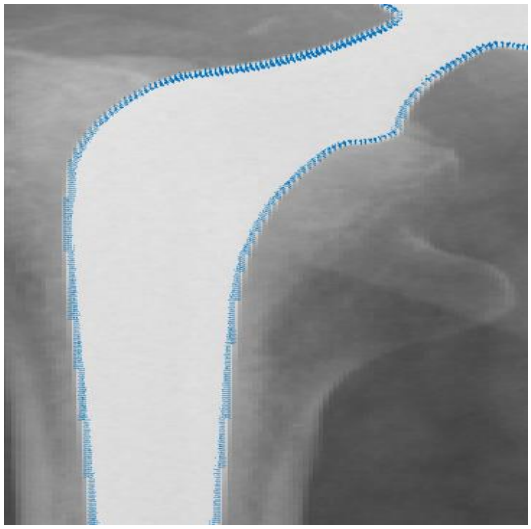

A sample THR x-ray image without loosening-2

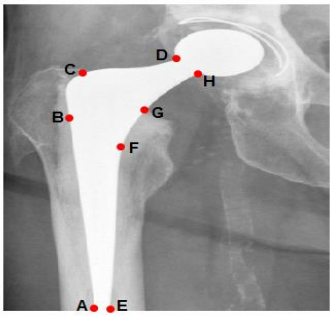

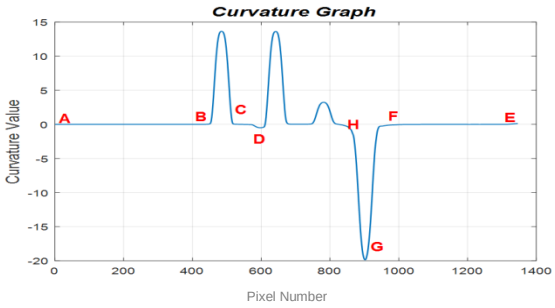

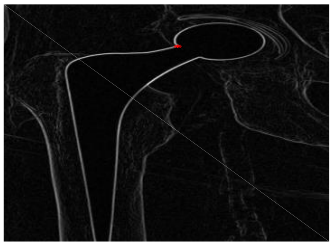

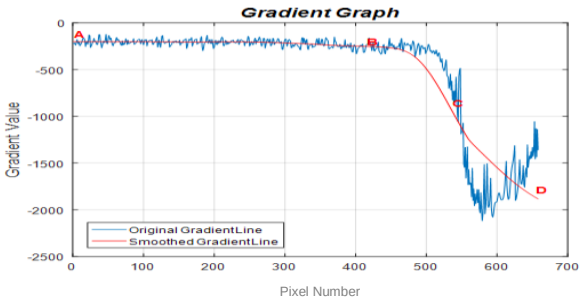

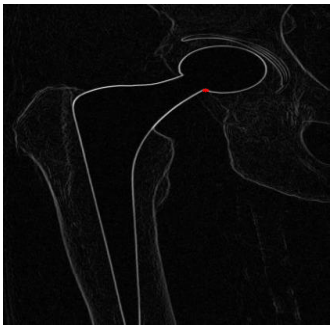

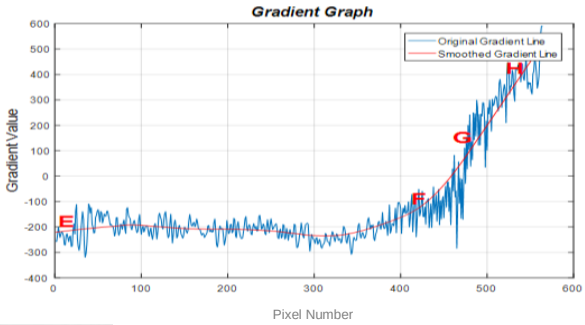

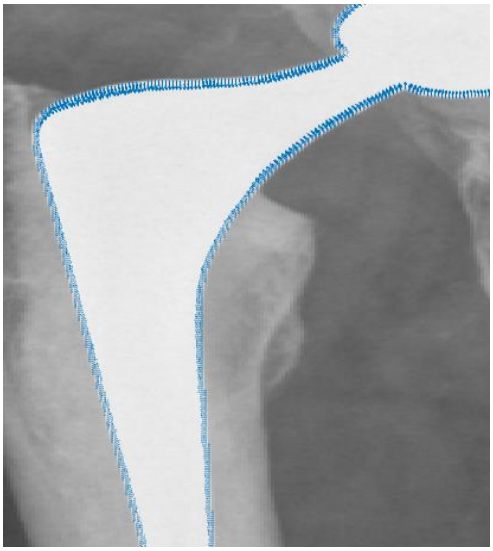

A sample THR x-ray image without loosening-3

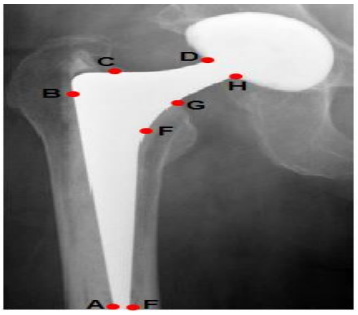

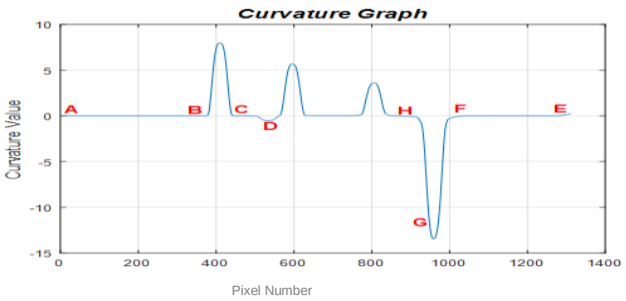

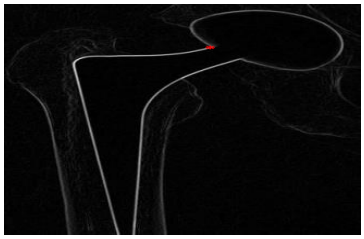

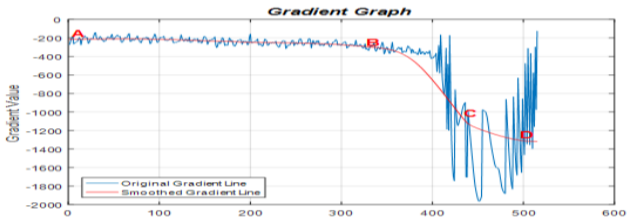

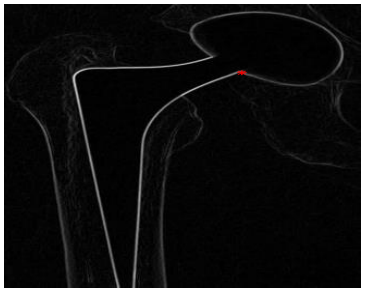

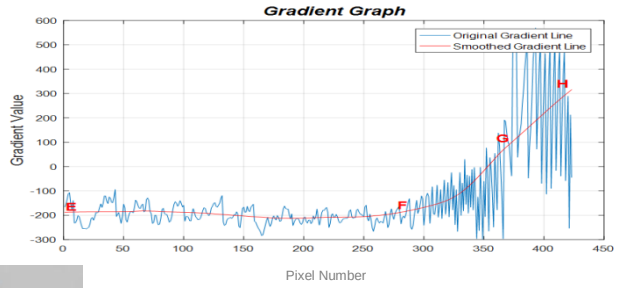

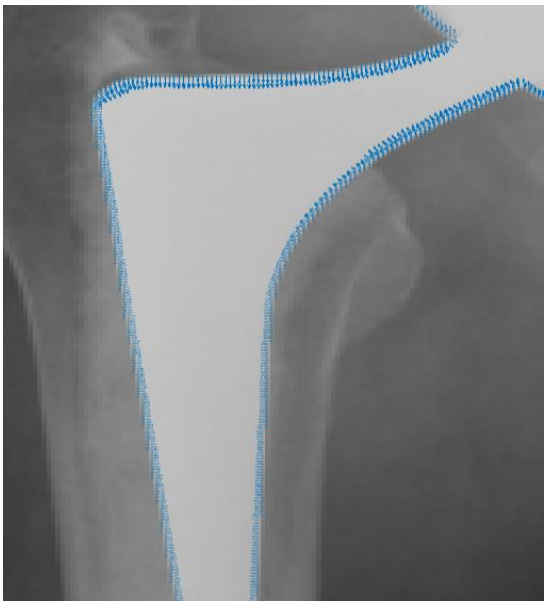

Appendix B.

A sample THR x-ray image without Subsidence (note that the size of the segmented region is 120 pixel) – Image 1

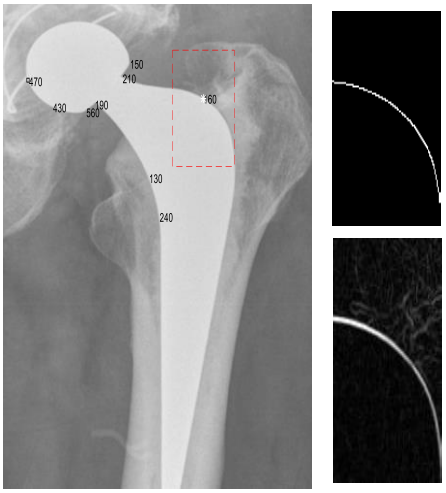

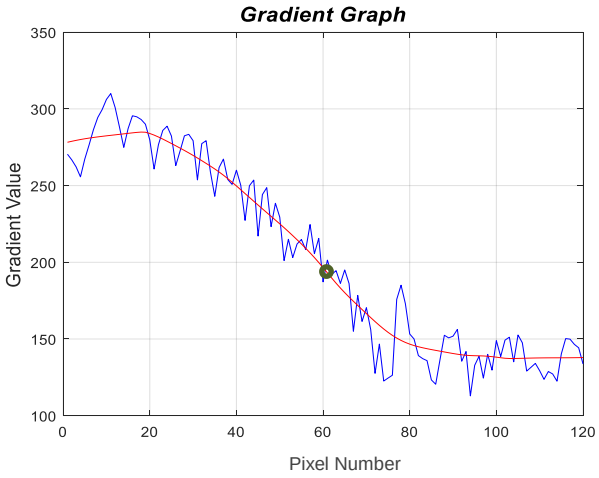

A sample THR x-ray image without Subsidenc- Image 2

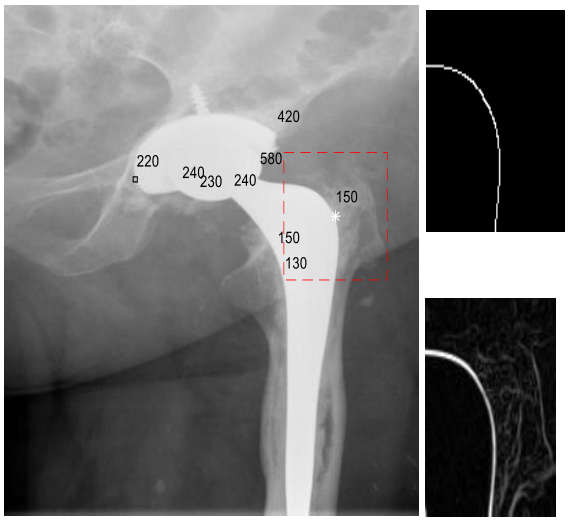

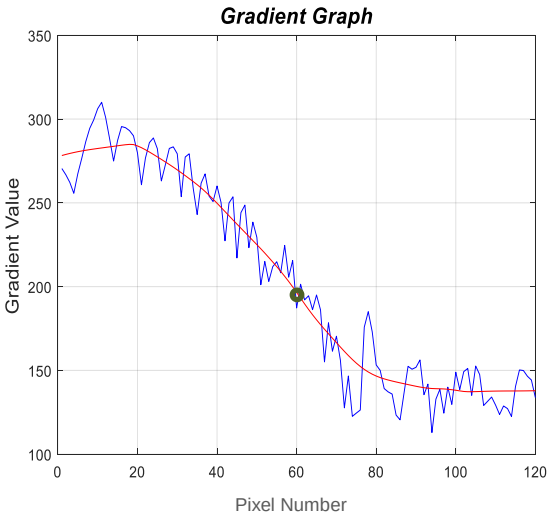

A sample THR x-ray image without Subsidenc- Image 3

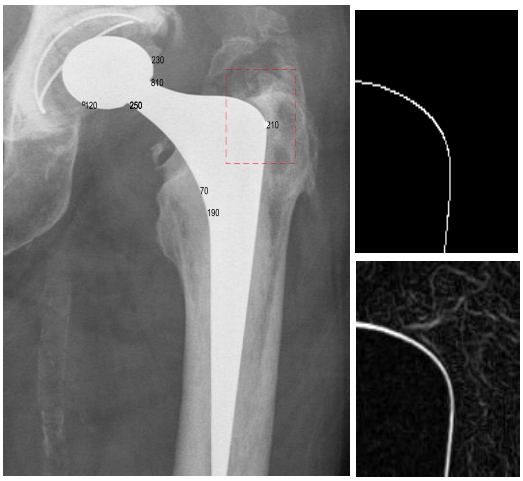

A sample THR x-ray image without Subsidenc- Image 4

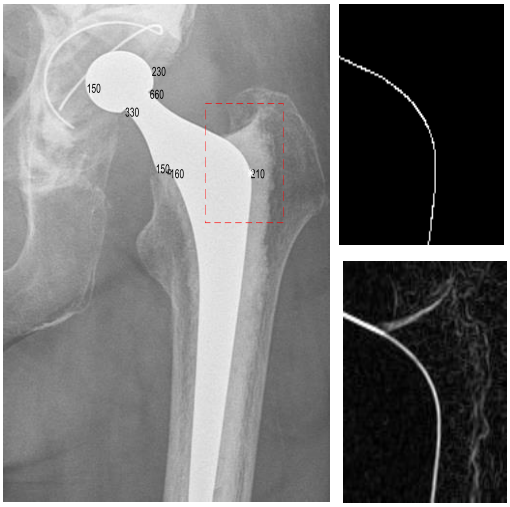

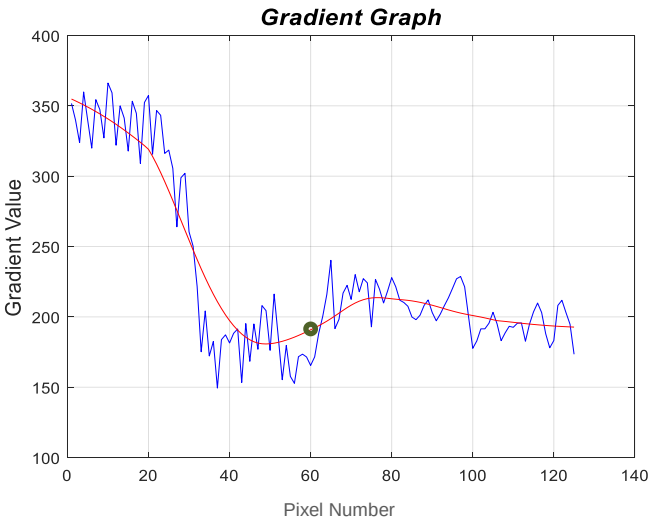

Appendix C. Sample of Infected THR x-ray Images

No.	Infected THR Image	Gradient Magnitude Graphs
a)	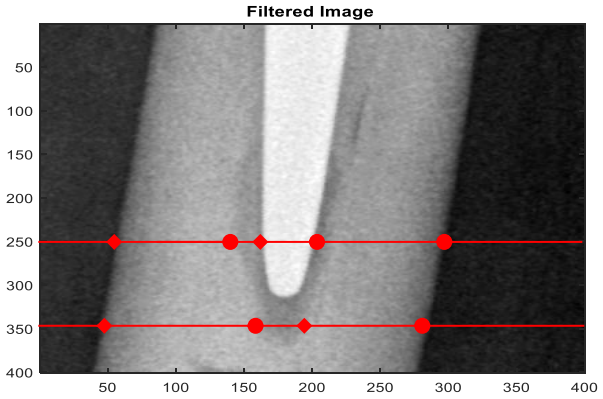	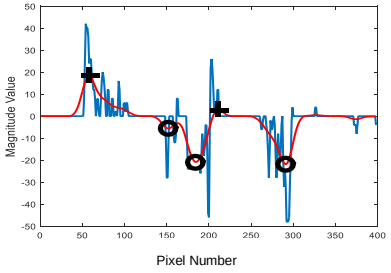 **Graph 1: Magnitude at line 250** 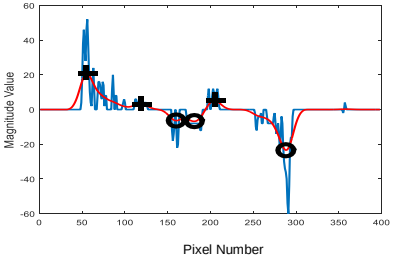 **Graph 2: Magnitude at line 270** 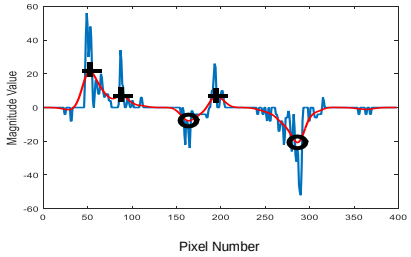 **Graph 3: Magnitude at line 290** 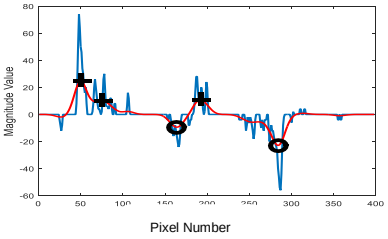 **Graph 4: Magnitude at line 310** 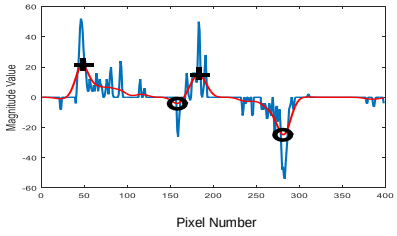 **Graph 5: Magnitude at line 330** 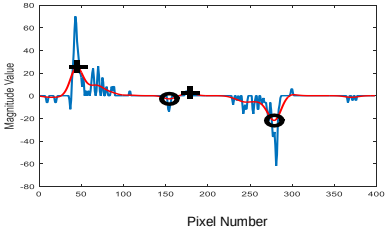 **Graph 6: Magnitude at line 350**

b)

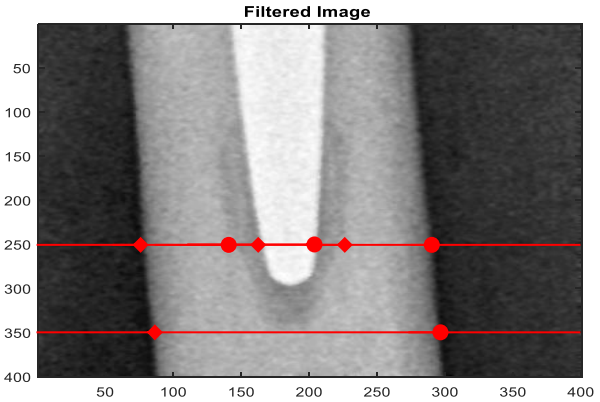

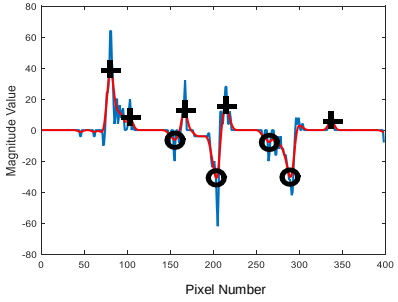

Graph 1: Magnitude at line 250

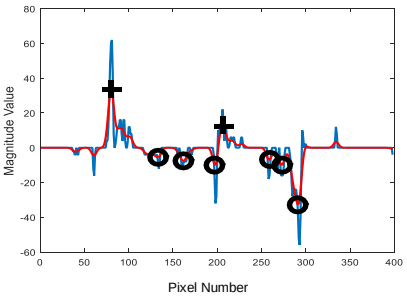

Graph 2: Magnitude at line 270

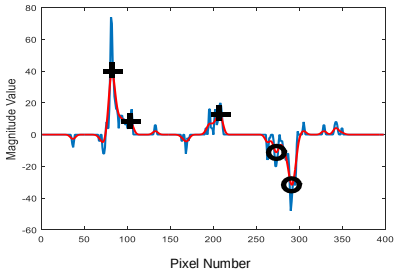

Graph 3: Magnitude at line 290

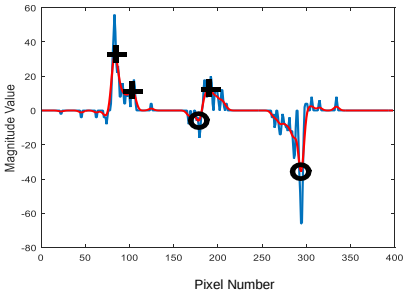

Graph 4: Magnitude at line 310

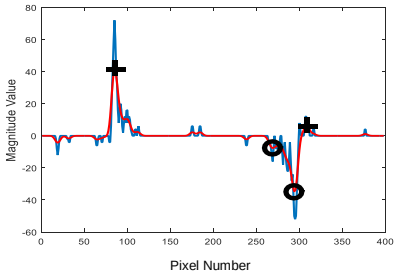

Graph 5: Magnitude at line 330

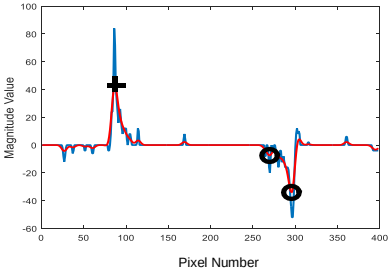

Graph 6: Magnitude at line 350

c)

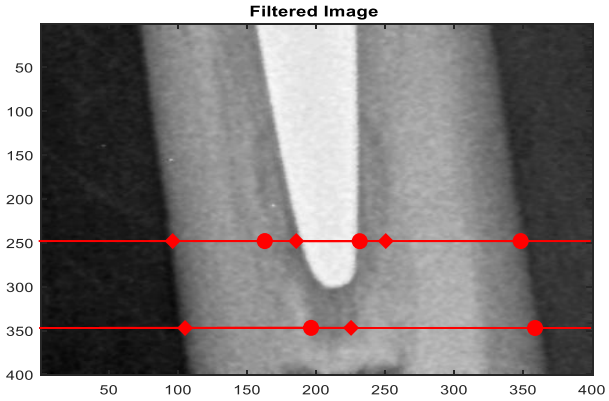

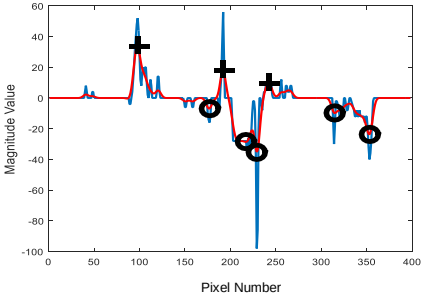

Graph 1: Magnitude at line 250

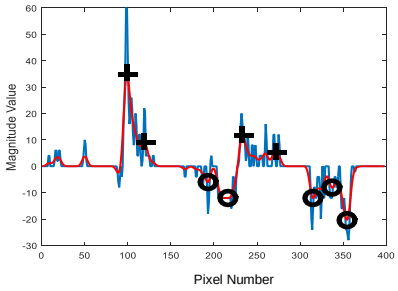

Graph 2: Magnitude at line 270

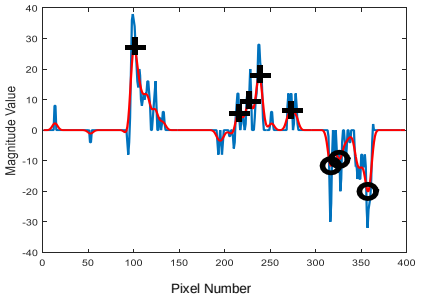

Graph 3: Magnitude at line 290

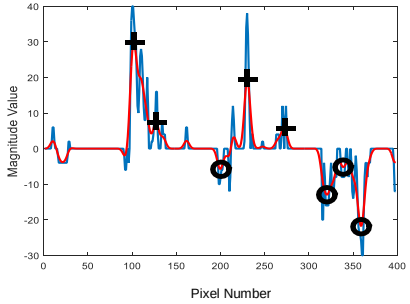

Graph 4: Magnitude at line 310

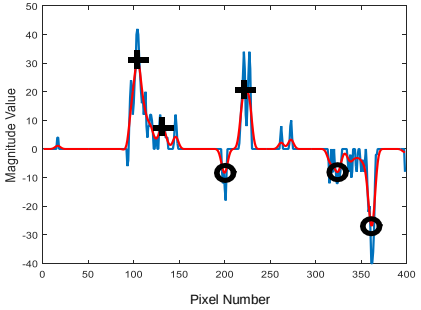

Graph 5: Magnitude at line 330

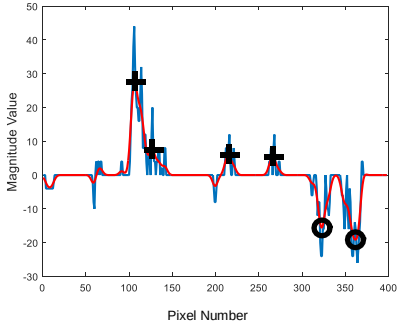

Graph 6: Magnitude at line 350

d)

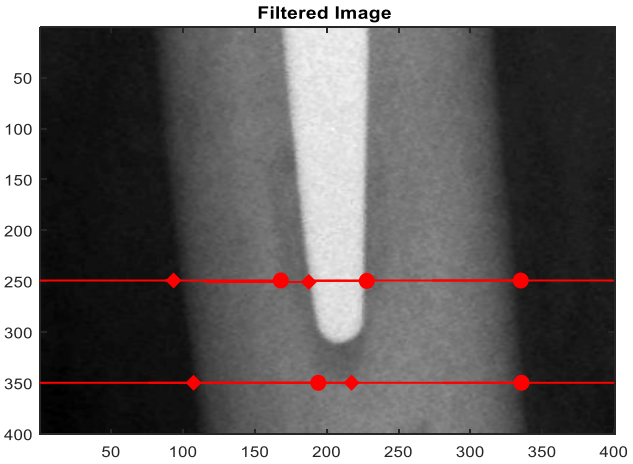

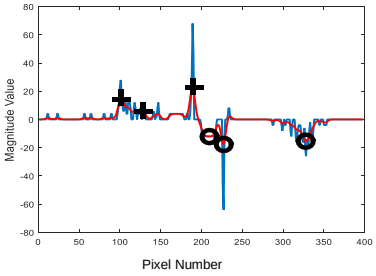

Graph 1: Magnitude at line 250

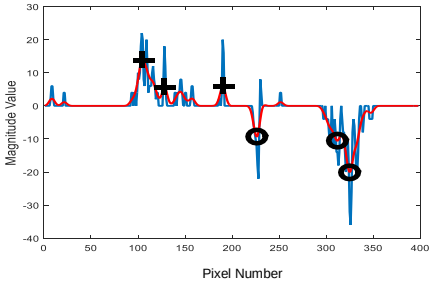

Graph 2: Magnitude at line 270

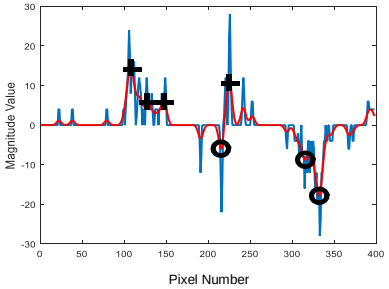

Graph 3: Magnitude at line 290

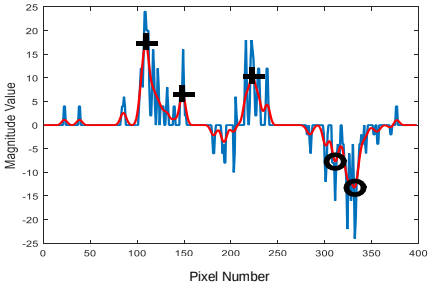

Graph 4: Magnitude at line 310

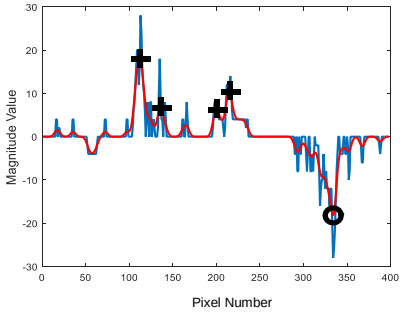

Graph 5: Magnitude at line 330

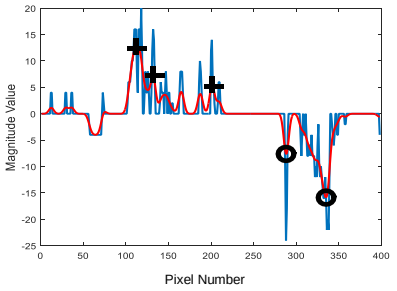

Graph 6: Magnitude at line 350